Università degli Studi di Milano Bicocca
Dipartimento di Fisica “Giuseppe Occhialini"

PhD in Physics and Astronomy
Cycle XXXVII

Design, characterization, and testing of modular readout electronics for Kinetic Inductance Detectors for the COSMO Experiment

By

Giulia Conenna

Supervisor:
Prof. Mario Zannoni

Tutor:
Prof. Massimo Gervasi

Academic years: 2021/2024

ἓν οἶδα ὅτι οὐδὲν οἶδα

Contents

Abstract

This thesis focuses on the design, testing, and characterization of readout electronics for a Kinetic Inductance Detector (KID)-based experiment, COSMO (COSmological Monopole Observer), using commercial components for reliability and rapid prototyping.
COSMO is an experiment aimed at searching for y-type spectral distortions in the Cosmic Microwave Background (CMB) between 120 and 300 GHz. It will be operated from Concordia Station on the Antarctic plateau. The experiment is based on a cryogenic Martin-Puplett interferometer with KIDs as its superconductive detectors. The COSMO focal plane will feature 18 multimode aluminum KIDs, with an expected baseband between 80 and 120 MHz. The interferometer will produce interferograms proportional to the difference between the sky and an internal reference black body. To compensate for atmospheric fluctuations, the sky signal is modulated at a high rate. This modulation imposes a critical requirement on the readout electronics: it must be capable of ultra-fast rates to track the signal modulation and perform detector diagnostics. This readout architecture is based on an IQ transceiver generating a comb of test tones, each tuned to a detector frequency. This prototype of readout electronics can achieve and maintain a readout rate higher than 60 kHz for 18 detectors.
After an overview of modern cosmology and state-of-the-art experiments with a focus on spectral distortions, the COSMO experiment will be introduced, highlighting the scanning strategy, detector selection, and the readout electronics developed and tested in this thesis. This is followed by an introduction to KIDs and their properties. The subsequent chapters detail the COSMO electronics readout firmware and software, alongside the strategy for detecting KID amplitude and phase variations using Digital Down Conversion (DDC). A full description and characterization of the COSMO readout electronics components will precede the presentation of test results in both warm and cryogenic environments. Since COSMO KIDs weren't ready at the time of this thesis, thanks to the large band of the readout electronics, the majority of the tests was conducted in a 4 K cryostat at the University of Milano-Bicocca on an array of Niobium KIDs working at approximately 2 GHz, with further tests at the University of Rome Sapienza on Aluminum KIDs in a dilution cryostat, at 300 MHz. Additionally, a graphical user interface was developed to provide a user-friendly interface.

Introduction

Since its revolutionary first detection by A. Penzias and R. Wilson at Bell Labs[1], it has been clear that the Cosmic Microwave Background (CMB) had the potential to transform our understanding of the Universe by providing crucial information about its origin, evolution, and composition. This faint relic radiation, dating back to when the Universe was just 380.000 years old, encodes invaluable data about the physical conditions of the early cosmos.
After many decades of increasingly precise measurements, a consensus cosmological model, known as the ΛCDM model, has emerged. Built on CMB observations and supported by a range of other experimental evidence, this model describes a Universe dominated by cold dark matter (CDM) and a cosmological constant (Λ), which drives accelerated cosmic expansion. The ΛCDM model has successfully explained a wide array of phenomena, from the large-scale structures of the Universe to the anisotropies in the CMB, allowing us to trace the history of the Universe with remarkable accuracy.
However, despite its successes, the ΛCDM model leaves several important questions unanswered. For instance, the nature of dark matter and dark energy remains elusive, and the model does not account for the physics of the very early Universe, particularly the period of Inflation, when the Universe underwent rapid exponential expansion. In connection with this, precise measurements of the CMB's polarization patterns, particularly the elusive B-modes, would offer insights into primordial gravitational waves generated during Inflation. While the detection of B-modes is a primary target for many current CMB experiments, an alternative path is represented by spectral distortions, small deviations from the CMB's perfect blackbody spectrum, that offer complementary information on the thermal history of the Universe, potentially opening a new observational window into the physics of the early Universe. Spectral distortions are generated by processes that drive matter and radiation out of thermal equilibrium after thermalization becomes inefficient. There are μ- and y-type of distortions. Compton scattering is inefficient at redshift $z < 5 \cdot 10^4$ yielding to y-type distortion, which probes the thermal history during recombination and reionization. In contrast, a μ-type distortions forms at $z > 5 \cdot 10^4$, when Compton scattering is very efficient, probing events in the pre-recombination era.
This thesis focuses on the development, testing and characterizing the readout electronics for a Kinetic Inductance Detector (KID)-based experiment, COSMO (COSmological Monopole Observer) designed to search for the y-type spectral distortions in the CMB.

KIDs are highly sensitive cryogenic superconducting detectors operating on the principle of kinetic inductance. When photons strike the superconducting material, they break apart Cooper pairs (the paired electrons responsible for superconductivity) and create quasiparticles. This process changes the kinetic inductance of the material, which in turn affects its resonance frequency and its phase. By measuring these shifts, KIDs can detect incoming photons with high sensitivity.

Chapter 1 provides an overview of modern cosmology and state-of-the-art experiments, with a focus on spectral distortions. Chapter 2 introduces the COSMO experiment, emphasizing the scanning strategy, the detectors chosen, and an introduction to the readout electronics tested and developed in this thesis. Chapter 3 gives an introduction to KIDs and their properties. Chapter 4 details the COSMO electronics readout firmware and software, along with the strategy for detecting KIDs' amplitude and phase variations using Digital Down Conversion (DDC). Chapter 6 presents test results of the COSMO readout electronics in both warm and cryogenic environments. Chapter 5 is dedicated to describing and characterizing the components of the COSMO readout electronics. Chapter 6 presents the test results of the COSMO readout electronics in both warm and cryogenic environments. Since COSMO KIDs were not available at the time of this thesis, tests were conducted in a 4 K cryostat at the University of Milano-Bicocca, where an array of Niobium KIDs was cooled, and further testing took place at the University of Rome Sapienza with Aluminum KIDs in a dilution cryostat. Finally, Chapter 7 briefly reviews other CMB experiments utilizing KIDs, for comparison purposes.

Chapter 1

Science behind spectral distortions

In this chapter, I present an overview of modern cosmology, with a particular emphasis on the Cosmic Microwave Background (CMB). I delve into its historical significance, key experiments, and the future directions of research in this field.
I then move into a detailed review of CMB spectral distortions. This focus stems from my involvement in the COSMO (COSmological Monopole Observer) experiment, which aims to measure the CMB isotropic component of the y-distortions, as elaborated in chapter 2.

1.1 Overview to Modern Cosmology

During the first decades of the 20th century, the search for a theory that could explain the origin and evolution of the Universe gave birth to Modern Cosmology. The path to explain on a physics base the origin and the evolution of the Universe was theoretically opened by the overcoming of the classic Newtonian theory of gravity, the Einsten's theory of General Relativity, which provided a unified description of gravity as a geometric property of four dimensional spacetime. Soon afterwards, principles that the Universe (at its origin, and at large scales) is homogeneous and isotropic (assumptions known as the Cosmological Principle) were added to the theory. Observational evidences of an expanding Universe, i.e. mostly the Hubble's law, also led to the idea that the theory should include an evolution history of the cosmos, or in other words that the metric must include a time-dependent factor in the spatial terms.
The most general spacetime metric through which the expanding Universe can be described and in which the Cosmological Principle applies is the so called *Friedmann - Lemaitre - Robertson - Walker* (FLRW) *metric* [2, 3, 4, 5]:

$$ds^2 = c^2 dt^2 - a(t)^2 \left[\frac{dr^2}{1 - Kr^2} + r^2 \left(d\theta^2 + \sin^2\theta \, d\phi^2 \right) \right] \tag{1.1}$$

where r, θ, ϕ are the comoving spherical polar coordinates; $a(t)$, the *cosmic scale factor*, describes how distances in a homogeneous, isotropic Universe expand or

contract with time; t, the cosmological proper time, is the time measured by an observer who sees the Universe expanding isotropically around him; K is the *curvature parameter* that can assume the values from -1 to 1, depending on the curvature of the space.
In a Universe described by the FLRW metric, one can assume the existence of 3 components: non relativistic matter (m), radiation - relativistic matter (r), and dark energy associated with the cosmological constant Λ. A solution of the Einstein equations is given by the following two equations called *Friedmann equations*:

$$H^2 = \left(\frac{\dot{a}}{a}\right)^2 = \frac{8\pi G}{3}\sum \rho_{\mathrm{i}} + \frac{\Lambda}{3} - \frac{K}{a^2} = H_0^2\left[\frac{\Omega_{0,\mathrm{r}}}{a(t)^4} + \frac{\Omega_{0,\mathrm{m}}}{a(t)^3} + \Omega_{0,\Lambda} + \frac{1-\Omega_0}{a(t)^2}\right] \tag{1.2}$$

$$\frac{\ddot{a}}{a} = -\frac{4\pi G}{3}\sum \rho_{\mathrm{i}}(1+3w_{\mathrm{i}}) + \frac{\Lambda}{3}c^2 \tag{1.3}$$

For convention the subscript "0" indicates the value of a time varying quantity evaluated at the present.
$\Omega_{0,\mathrm{r}} = \rho_{0,\mathrm{r}}/\rho_{0,\mathrm{c}}$, $\Omega_{0,\mathrm{m}} = \rho_{0,\mathrm{m}}/\rho_{0,\mathrm{c}}$, $\Omega_{0,\Lambda} = \rho_{0,\Lambda}/\rho_{0,\mathrm{c}}$ are the *density parameters*, with $\rho_{0,\mathrm{c}}$ the critical density defined as $\rho_{0,\mathrm{c}} = \dfrac{3H_0^2}{8\pi G}$ and $\rho_{0,\mathrm{m}}$, $\rho_{0,\mathrm{r}}$ and $\rho_{0,\Lambda}$ are, respectively, the matter, radiation and cosmological parameter associated density evaluated at present. Finally, $\Omega_0 = \Omega_{0,\mathrm{r}} + \Omega_{\mathrm{m},0} + \Omega_{\Lambda,0}$.
$H \equiv \dot{a}/a$ is the Hubble parameter and when evaluated at present time it is the so called *Hubble constant* H_0.
The density of the components is also related to the scale factor as: $\rho_{\mathrm{i}}(a) = \rho_0 a^{-3(1+w_{\mathrm{i}})}$, where w_i is a constant parameter which is equal to 0, 1/3 and -1, for non relativistic matter, relativistic component and cosmological constant respectively.

The discovery of Cosmic Microwave Background (CMB) allowed to exclude hypothesis of a Steady-State Universe [6, 7], showing the existence of a relic radiation permeating the whole Universe, whose tiny anisotropies carry precious information on the early conditions of the cosmos, supporting the idea of the hot Big Bang model. After decades of experimental missions to measure the intensity and the polarization anisotropies of the CMB, we now know not only that our Universe is expanding and flat, but we also have precise estimations of the theory parameters. The latest values for the parameters described above, obtained by Planck [8], are summarized in table 1.1.

1.2 What is CMB and some history of its measurements

One of the major advances in twentieth-century astronomy was the discovery of the origin of heavy elements. We know today that essentially all the heavy

Hubble constant H_0	67.36 ± 0.54 km s^{-1} Mpc^{-1}
Matter density Ω_m	0.3153 ± 0.0073
Dark energy density Ω_Λ	0.6847 ± 0.0073

Table 1.1: Cosmological parameter values from the Planck Collaboration [8] for the ΛCDM model. Data are from Planck CMB temperature power spectra, in combination with high multipole, polarization spectra and CMB lensing reconstruction. Cosmological parameters have 68% confidence limits.

elements are created by thermonuclear reactions at the centers of stars and in supernovae. The starting point of all these reactions is the fusion of hydrogen into helium. However, as astronomers began to understand the details of thermonuclear synthesis in the 1960s, they were faced with a dilemma: there is far more helium in the Universe than could have been created by hydrogen fusion in stars. The presence of so much helium posed a major dilemma and many theories were proposed.

1.2.1 History

In 1946 G. Gamow [9] and his colleagues introduced the *Hot* Big Bang model, with the thought that temperature of the order of $10^9 - 10^{10}$ K would be required to build up nuclei heavier than hydrogen. They also recognized that this scenario would have left the present Universe at a non-zero temperature. Afterwards, R. Alpher and R. Herman [10] made specific predictions on the present "background temperature", estimating $T_0 \simeq 5$ K.
By the early 1960s, receivers operating at centimeter wavelengths had been improved. Radio astronomers workers at Bell Labs (including Arno Penzias and Robert Wilson) detected an excess of *noise* [1, 11] entering the antennas at any point of the sky. After correcting for all the possible sources of systematic errors, the "excess noise" from the sky was measured at a wavelength $\lambda = 7.35$ cm and showing an intensity equivalent to 3.5 K.
Unaware of all the theoretical and observational works of those years, Robert H. Dicke and his Princeton colleagues, in 1964 were busy in reinventing the Hot Big Bang [12], and in designing a sensitive receiver to detect the thermal background left by it.
The one who put in touch Bell Labs workers with Dicke and colleagues was Bernie Burke, one of the founding fathers of radio astronomy, after having attended a talk by Jim Peebles about the Hot Big Bang, the importance of radiation in the early Universe and its detection.
Dicke and collaborators explained this "excess noise" as the thermal cosmic background, a relic of a Hot Big Bang. However, several other, non-Big-Bang, explanations were proposed but there were two crucial tests of the Big Bang hypothesis. First, relic radiation from a Hot Big Bang would have a thermal (Planck) spectrum. Second, relic radiation would be isotropic.

Both these tests were passed from 1967 on-wards.

Since then, CMB has been and still is a subject of study, leading to numerous experiments and observations that have significantly advanced our understanding of the early Universe, helping to shape our current cosmological models and theories.
Here are some past experiments and missions related to the CMB:

- After the discovery of CMB the experiments were aimed at determining with a larger accuracy the CMB temperature and to identify any distortions from the blackbody spectrum. A notable boost in such direction was achieved by the White Mountain collaboration. Some Italian and American groups decided to carry out measurements together using five radio receivers at different frequencies, from 2.5 GHz to 90 GHz, calibrating them with the same reference source. The results [13] are consistent with a Planck spectrum at a temperature $T_0 = 2.73 \pm 0.05$ K. The measurements were subsequently improved and extended, especially at low frequencies.

- In 1976 George Smoot and collaborators [14] detected anisotropy in the CMB with a 33 GHz twin-antenna Dicke radiometer flown to an altitude of 20 km aboard a U-2 aircraft. Later, in 1978 dipole anisotropy in the CMB in the 500-3000μm wavelength region had been measured in a balloon-borne experiment by Francesco Melchiorri and collaborators [15].

- COBE (Cosmic Background Explorer) [16, 17, 18, 19, 20, 21, 22]: launched in 1989, COBE was a NASA satellite that provided the first high-precision map of the cosmic microwave background radiation. Its observations confirmed the Plank spectrum and detected for the first time tiny anisotropies providing important data about its characteristics. Two of COBE's principal investigators, George F. Smoot and John C. Mather, received the Nobel Prize in Physics in 2006 for their work on the project. According to the Nobel Prize committee, "the COBE project can also be regarded as the starting point for cosmology as a precision science".

- BOOMERanG (Balloon Observations of Millimetric Extragalactic Radiation and Geophysics) [23]: BOOMERanG was a series of balloon-borne experiments aimed at measuring the anisotropies of the CMB. The first BOOMERanG flight took place in 1997 from Antarctica, followed by a second flight in 1998. These experiments provided some of the earliest high-resolution maps of the CMB temperature fluctuations, helping to constrain cosmological parameters. The most important result was the precise measurement of the space curvature, confirming that the Universe is flat.

- MAXIMA (Millimeter Anisotropy eXperiment Imaging Array) [24]: MAXIMA was a balloon-borne experiment launched in 1998 and again in 1999 from New Mexico. It aimed at measuring the small-scale fluctuations in

the cosmic microwave background radiation. MAXIMA provided high-resolution maps of the CMB anisotropies, contributing to our understanding of the early Universe's structure and evolution.

- DASI (Degree Angular Scale Interferometer) [25]: operating between 1999 and 2007 from the South Pole, DASI was a microwave telescope designed to measure the small-scale anisotropies in the cosmic microwave background radiation. It made high-resolution maps of the CMB polarization and temperature fluctuations. DASI made a significant breakthrough in cosmology by providing the first detection of the E-mode polarization.

- WMAP (Wilkinson Microwave Anisotropy Probe) [26]: launched in 2001, WMAP was a NASA satellite designed to measure the temperature fluctuations in the cosmic microwave background radiation with unprecedented precision. WMAP provided a detailed fully-sky map of the CMB anisotropies.

- Planck Satellite [27]: Launched by the European Space Agency (ESA) in 2009, the Planck satellite was specifically designed to study the cosmic microwave background with even higher precision than previous missions. Planck's observations provided highly detailed maps of the CMB temperature and polarization anisotropies, offering insights into the early Universe's properties and evolution.

- BICEP/Keck Array [28]: working from the South Pole since 2006, BICEP is a series of experiments aimed at measuring the polarization of the CMB. The primary goal of BICEP is to detect the "B-mode" polarization pattern in the CMB, which would be a direct signature of primordial gravitational waves generated during cosmic inflation. The joint analysis with Planck data represents the most precise upper limit to the cosmological B-modes polarization of CMB [29].

- SPTpol (South Pole Telescope Polarimeter) [30] is an instrument installed on the South Pole Telescope starting from 2012, specifically designed to measure the polarization of the CMB with high sensitivity. In 2013, SPTpol achieved a significant milestone by detecting B-mode polarization resulting from gravitational lensing.

- POLARBEAR [31]: starting from 2012 in Atacama Desert, Chile, POLARBEAR is a cosmic microwave background polarization experiment that aims at measuring the polarization signals of the CMB with high sensitivity and resolution. It focuses on detecting the signature of primordial gravitational waves, which would provide direct evidence for cosmic inflation. The POLARBEAR team was able to report that the measured B-mode polarization from lensing was of cosmic origin at a 97.2% confidence level by focusing their observing time on this small patch where they are highly sensitive to arcminute anisotropies.

- SPIDER (Suborbital Polarimeter for Inflation, Dust, and the Epoch of Reionization) [32]: Spider is a balloon-borne experiment designed to measure the polarization of the cosmic microwave background radiation. Launched in multiple campaigns from Antarctica, the first in 2015, SPIDER aims at detecting the signature of primordial gravitational waves in the polarization of the CMB. By studying these polarization patterns, SPIDER helps to test inflationary models of the early Universe and constrain cosmological parameters.

The main result of the observations are summarized here:

- Confirmation of the Big Bang Theory: CMB observations provide strong evidence supporting the Big Bang theory, which posits that the Universe originated from an extremely hot and dense state approximately 14.8[†] billion years ago. The uniformity and isotropy of the CMB across the sky corroborate the idea of a homogeneous and isotropic early Universe.
- CMB spectrum is very close to a perfect blackbody, at any angular position in the sky. Thus it is also isotropic.
- The CMB has the dipole distortion in temperature, which is a Doppler shift caused by the net motion of the Earth relative to a reference frame in which the CMB is isotropic. From this it is possible to infer that the Local Group is moving toward Hydra at 0.2% the speed of light.
- The CMB mean temperature is $\langle T \rangle = 2.7255 \pm 0.0006$ K; there are temperature fluctuation (after removing the dipole) of the order of 10^{-5}. Temperature fluctuations provide crucial insights into the seeds of cosmic structure formation, with slightly denser regions eventually evolving into galaxies and galaxy clusters while underdense regions become voids.

In the field of CMB research, there are two main goals still missing: the detection of primordial B-mode polarization and the measurement of spectral distortions. B-mode polarization refers to a specific pattern of polarization in the CMB. Unlike the E-mode polarization, which arises from density fluctuations in the early Universe, B-mode polarization can be generated by gravitational waves produced during the period of cosmic inflation. The detection of primordial B-mode polarization would provide direct evidence for the inflationary model of the early Universe.
Spectral distortions in the CMB refer to deviations (see figure 1.1) from the characteristic blackbody spectrum expected from the CMB. Spectral distortions carry valuable information about the thermal and ionization history of the Universe, as well as the properties of exotic phenomena like decaying dark matter or primordial black holes. By measuring these distortions, it will be possible to probe the conditions of the early Universe and test cosmological models.
Spectral distortions are extensively treated in 1.6.

[†]Assuming $H_0 \simeq 67.4$ km/s/Mpc [33]

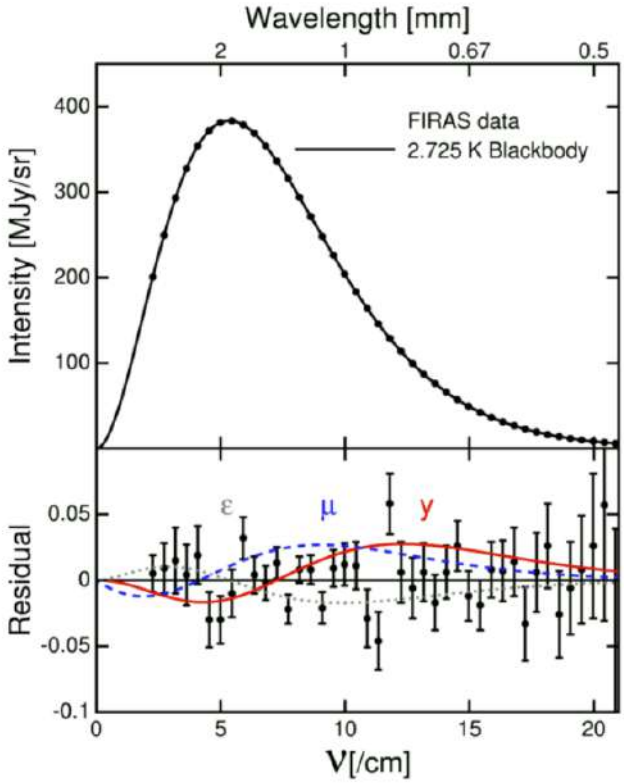

Figure 1.1: FIRAS measurement: the difference between the CMB and the best fitting blackbody. The plot at top shows this residual added to the theoretical blackbody spectrum. The three curves in the bottom correspond to three fairly likely non-blackbody spectra: the grey curve shows a body with a reflectivity of 100 parts per million instead of zero, and the red and blue curves show the effect of hot electrons adding an excess 60 parts per million of energy to the CMB either before (blue) or after (red) 1000 years after the Big Bang. [18]

1.3 Thermal history of the Universe: origin of the CMB

In order to explain the origin of the CMB, it is necessary to distinguish two closely and related moments in the history of the Universe [34]:

- epoch of *recombination*: is the time at which the baryonic component of the Universe goes from being ionized to being neutral. $T_{\rm rec}$ =3760 K, $z_{\rm rec} = 1380$
- epoch of *photon decoupling*: is the time at which the photon path-length is larger than the Hubble radius. Indeed, when photons decouple, they cease to interact with the electrons, and the Universe becomes transparent. $T_{\rm dec}$ =2970 K, $z_{\rm dec} = 1090$.
  At the same epoch the *last scattering* between CMB photons and free electrons also occurs: $T_{\rm lss} \simeq T_{\rm dec} \simeq 2970$ K, $z_{\rm lss} \simeq z_{\rm dec} \simeq 1090$.

Indeed, CMB is the relic of the radiation coming from the last scattering surface.

1.4 Inflation

Inflation is a critical concept in modern cosmology, referring to a rapid exponential expansion of the Universe that occurred in the first fractions of a second after the Big Bang, roughly from 10^{-36} seconds to10^{-32} seconds. This period of accelerated growth is thought to have stretched space-time to vast scales, smoothing out irregularities and setting the initial conditions for the Universe's large-scale structure. The theory of inflation helps explain several key features of the cosmos, such as the uniformity of the CMB and the distribution of galaxies. By studying the imprints of inflation on the CMB and other cosmic phenomena, researchers aim to uncover the physical processes that shaped the Universe's early evolution.
However, while inflation is an important topic in cosmology (a very good review of the problem is [35]), it is not the primary focus of this thesis. Instead, this work investigates spectral distortions in the CMB, which offer valuable insights into the Universe's history but are distinct from the study of inflation itself.

1.5 CMB Intensity Anisotropies

Inflationary models predict that the density fluctuations are generated by quantum fluctuation during the inflationary phase. Thus, Gaussian fields are strongly motivated by inflation.
CMB radiation has temperature anisotropies that are described as a fraction of T_0, the mean temperature, and a function of angular position on the sky

$$\frac{\Delta T}{T} = \frac{T(\theta,\phi) - T_0}{T_0} \tag{1.4}$$

Fluctuations in the temperature T can be treated in term of the spherical harmonics as follows:

$$\frac{\Delta T}{T} = \sum_{l=0}^{\infty} \sum_{m=-l}^{m=+l} a_{lm} Y_{lm}(\theta,\phi) \tag{1.5}$$

where θ and ϕ are the spherical angles; the Y_{lm} are the spherical harmonics, a complete orthonormal set of functions on the surface of a sphere; the a_{lm} are complex coefficients that have to satisfy the condition:

$$\left\langle a^*_{l'm'} a_{lm} \right\rangle = C_l \delta_{ll'} \delta_{mm'} \tag{1.6}$$

where δ_{ij} is the Kronecker symbol and C_l is the angular power spectrum:

$$C_l \equiv \left\langle |a_{lm}|^2 \right\rangle \tag{1.7}$$

The autocovariance function for the temperature fluctuations is defined as:

$$C(\theta) = \left\langle \frac{\Delta T}{T}(\hat{\mathbf{n}}_1) \frac{\Delta T}{T}(\hat{\mathbf{n}}_2) \right\rangle \tag{1.8}$$

where $\cos\theta = \hat{\mathbf{n}}_1 \cdot \hat{\mathbf{n}}_2$, with $\hat{\mathbf{n}}_i$ unit vectors pointing to arbitrary directions on the sky.
It is possible to estimate $C(\theta)$ and C_l from an individual sky using an *ergodic hypothesis* , for which making an average over the probability ensemble is the same as an average over all the spatial positions. This hypothesis is solid only for small angular scales when it is possible to average over many different pairs of directions with the same θ, or many different modes with the same l.However, the small quantity or pairs at large angular scales leads to a bigger error which is usually referred as *cosmic variance*.
Using the Legendre polynomial $P_l(x)$, it is possible to establish a relationship between $C(\theta)$ and C_l :

$$C(\theta) = \frac{1}{4\pi} \sum_{l=2}^{\infty} (2l+1)\, C_l P_l(\cos\theta) \tag{1.9}$$

$$C_l = \frac{1}{4\pi} \int d^2\hat{\mathbf{n}}_1 d^2\hat{\mathbf{n}}_2 P_l(\hat{\mathbf{n}}_1 \cdot \hat{\mathbf{n}}_2)\, C(\theta) \tag{1.10}$$

Going back to eq. 1.5, the $l = 0$ term can be ignored since it is the monopole correction, which just alters the mean temperature ($Y_{00} = \text{const}$). The $l = 1$ is the dipole term, that is attributed to the motion of the observer through space and it is treated separately since it is not relevant for CMB anisotropies studies.
The remaining modes, from $l = 2$, the quadrupole term, are attributed to intrinsic anisotropies.
Moreover, eq. 1.6 is a fundamental result: in the harmonic space it is possible to show that each l is non correlated to the others and thus it can be studied individually.

The most updated map of the temperature anisotropies is showed in figure 1.2. This map is derived from the joint baseline analysis of Planck, WMAP, and 408 MHz observations [36].

1.5.1 CMB dipole

Dipole anisotropy of CMB is due to the motion of our Galaxy with respect to a cosmologically comoving frame where the CMB is isotropic. In term of the spherical coordinates, the dipole anisotropy is the variation with the angle between the observation and the direction of motion of the observer, θ, proportional to $\cos\theta$. This motion is of the order $\beta = v/c \simeq 10^{-3}$ and the net Doppler effect on the temperature is zero. Given the relatively high value of β, we need to consider a relativistic Doppler effect that has two components. The first is related to the fact that in the direction θ the observer collects $\left(1+\beta\cos\theta\right)$ more photons than an observer at rest, which makes the temperature increase by the same factor. The second effects is aberration, which makes the solid angle for a moving observer smaller by a factor $\left(1+\beta\cos\theta\right)^{-2}$.

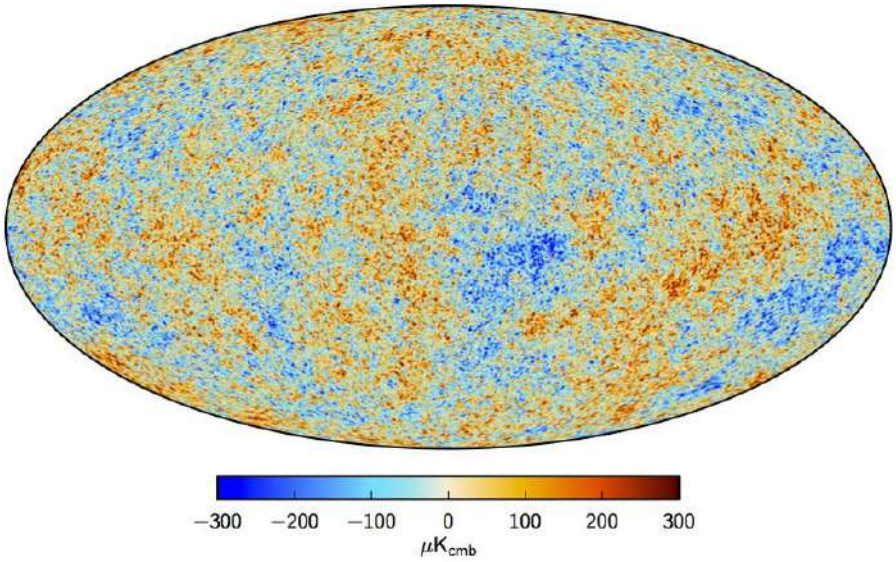

Figure 1.2: Temperature CMB anisotropy map from Planck Satellite, combined with the WMAP data and 408 MHz observations [36].

The final result of the temperature is:

$$T(\theta) = T_0\left(1-\beta^2\right)^{1/2}\left(1+\beta\cos\theta\right) \tag{1.11}$$

The contribute to the temperature of the dipole is bigger then the one of the high order multiples: this is the reason why dipole anisotropy is actually treated separately.

1.5.2 Intrinsic CMB temperature anisotropy

The moments with $l \geq 2$ are cosmologically more interesting since they are due to intrinsic anisotropies of the CMB.
Anisotropies can be distinguished between primary and secondary. The former arise due to effects at the time of recombination; the latter are generated after the last scattering surface during the travel of the photons.

1.5.2.1 Primary anisotropies

There are three main primary effects, which create anisotropies on the last scattering surface.

- *Sachs-Wolfe effect*, dominant on large scales, is caused by the potential perturbations at last scattering, and has two different components .
  The first is the shift in frequency of the photons traveling from the last scattering surface to the observer: an overdense region cools the background as the photon lose energy climbing out; an underdense region heats it as

the photons gain energy. The contribution to the variation of temperature is:

$$\frac{\delta T}{T} = \frac{\delta \Phi}{c^2} \tag{1.12}$$

Potential perturbations cause also the time dilation at the last scattering surface, so that the observer seems be looking at a younger and hotter Universe where there is an overdesity. The contribution is:

$$\frac{\delta T}{T} = -\frac{2}{3}\frac{\delta \Phi}{c^2} \tag{1.13}$$

which is given by the dependence between scale factor and time and temperature[†].
The net contribution of *Sachs-Wolfe effect* is:

$$\frac{\Delta T}{T} = \frac{1}{3}\frac{\delta \Phi}{c^2} \tag{1.14}$$

- *Adiabatic perturbations*: If, as predicted by inflation theory, the fluctuation in the plasma are adiabatic, the temperature variation due to this is:

$$\frac{\Delta T}{T} = \frac{1}{3}\frac{\delta \rho_m}{\rho_m} \tag{1.15}$$

- *Velocity Doppler perturbations*: the plasma has a non-zero velocity at recombination, which leads to Doppler shifts in frequency and hence brightness temperature. The temperature variation due to the Doppler effect from the scattering of photons by moving plasma is:

$$\frac{\Delta T}{T} = \frac{\delta \mathbf{v} \cdot \hat{\mathbf{r}}}{c} \tag{1.16}$$

In addition, there are physical processes that act on the radiation perturbations, reducing the predicted anisotropies. In order to treat them, it is necessary to take into account the thickness of the last scattering shell, which has to be of the same order of magnitude of the photon mean free path at that time. For scale smaller than the photon mean free path, the radiation fluctuations are damped by diffusion of the photon in the baryonic fluid. This process is called *Silk damping*. Another process that can suppress the fluctuations is caused by dark matter. Indeed, dark matter perturbations can grow while the baryon fluid is still held back by radiation pressure, which causes adiabatic radiation fluctuations that are less than the one predicted by a dark matter spectrum alone.
There is also an oscillation signal in the CMB, which depends on the phase of the waves at the time of last scattering . Therefore, acoustic peaks in the small scale power spectrum of the CMB fluctuations are formed due to oscillations in the fluid of baryons plus radiation.

[†]Time dilation is $\frac{\delta t}{t} = \frac{\delta \Phi}{c^2}$, the scale factor $a \propto t^{2/3}$ and $T \propto a^{-1}$

1.5.2.2 Secondary anisotropies

As said above, there are other sources for anistropies, the so called secondary anistropies.
The most important are summarized here:

- *integrated Sachs-Wolfe effect*: similarly to the primary Sachs Wolfe effect, photons shift their frequency in traversing a linear gravitational potential from the last scattering surface to the observer.
- *Rees-Sciama effect*: if the gravitational potential is nonlinear, the integrated Sachs-Wolfe effects is called Rees-Sciama effect.
- *Sunyaev Zeldovich effect*: CMB photons undergo inverse Compton scattering with free electrons in the hot intracluster medium, gaining energy. In addition, the characteristic frequency dependence of this effect allows it to be distinguished from intrinsic anisotropies, since intracluster medium has temperature fluctuations at 10^{-5} level.
- *Reionization*: after first generation of star formation, UV photons are emitted into the intergalaxy medium and so hydrogen and helium are reionized
  ($6 < z < 12$). As consequence, CMB photons undergo inverse Compton scattering with the free electrons, changing and in particular gaining energy.
- *Gravitational lensing*: Large scale structure between the last scattering surface and the observer gravitationally lenses the temperature and polarization anisotropy of the CMB. Therefore, CMB lensing distorts the hot and cold spots of the temperature field around foreground masses.

1.5.3 CMB angular power spectrum

As mentioned previously, a useful tool for studying the anisotropies is the *angular power spectrum*.
As it is possible to notice in figure 1.3, the angular power spectrum is presented as:

$$\Delta T \equiv \left(\frac{l\,(l+1)}{2\pi} C_l \right)^{1/2} \langle T \rangle \tag{1.17}$$

as function of l, the multipole number, since this function tells the contribution per logarithmic interval in l to the total temperature fluctuation δT of the CMB. Indeed, the detailed shape of the ΔT versus l curve contains significant information about the Universe at the time of photon decoupling and it is possible to extract cosmological information from it.
For low l the dominant effect is the Sachs-Wolf effect, which gives birth to the

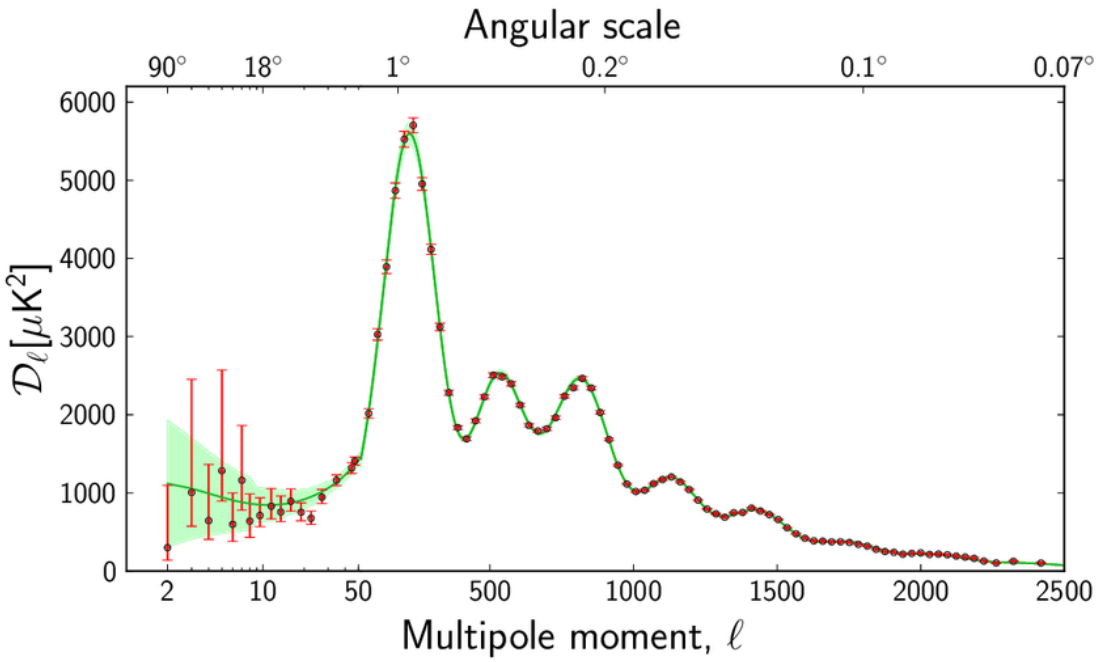

Figure 1.3: The CMB power spectrum as seen by Planck [36]. The red dots with error bars are the data points and the green line is the best fit theoretical model. The shaded region indicates the theoretical error from cosmic variance.

Sachs-Wolf Plateau. The initial fluctuations and the initial conditions of the Universe are measured in this angular scales, which are big ($\geq 1^\circ$), since the Universe did not have enough time to evolve.
Indeed, with a angular resolution of 7°, COBE satellite could see only this portion of power spectrum (up to $l = 28$).
For bigger l, the spectrum increasing up to $l \sim 200$, where there is the first peak, called the *Doppler peak*, caused by the Doppler effect as in equation 1.16. Its position has important implications in the standard cosmological model, in particular in determining the spatial curvature of the Universe.
For angular scales $\leq 1^\circ$, all the perturbations are oscillating: since photons and baryons are still coupled and arranged in the potential wells, they oscillate following compression and expansion phases. Thus, the peaks in the power angular spectrum are due to the *acoustic oscillations*, which corresponds to the compression phases since the peaks correspond to an area hotter then the average and so overdense.
For even smaller angular scales ($l \geq 800$) the dominant phenomenon is due to the *Silk damping*, which is important for determining the curvature of the Universe. Indeed, the curvature is strongly connected to the mean free path of the photons, which depends on the quantity of baryons in the plasma.
Other quantities can be inferred from the power spectrum, for example the second peak gives the quantity of ordinary matter present in the Universe.

1.6 Spectral distortions

CMB spectral distortions are tiny deviations from the perfect black body spectrum (see figure 1.1) and they provide fundamental information regarding the thermal history of the Universe. Indeed, they are important for the standard and non-standard cosmological models, for the study of the inflation era, for a better understanding of the evolution of the Universe, for understanding the baryonic feedback process and for baring the nature of dark matter.
Spectral distortions are originated by processes able to drive matter and radiation out of thermal equilibrium. Examples of such mechanism are the energy-release that heat the baryionc matter, the injection of photons or other particles that electromagnetically interact.
It is possible to distinguish two kind of spectral distortions, the μ and the y (as visible in figure 1.4) but the transition between these two is not sharp and during the gradual transition r type distortions are created.
COBE-FIRAS experiment put a limit on the dimensionless cosmological distortion parameters (95% confidence level) [37]:

- $|\,\mathrm{y}\,| < 2.5 \cdot 10^{-5}$
- $|\,\mu\,| < 3.3 \cdot 10^{-4}$

Later, the TRIS experiment [38] set a new limit with $|\,\mu\,| < 6 \cdot 10^{-5}$ (95% confidence level).
The expected values given by the ΛCDM model are [39]:

- $\mathrm{y} \sim 1 \cdot 10^{-6}$
- $\mu \sim 2 \cdot 10^{-8}$

1.6.1 The physics of CMB spectral distortions

CMB is the most perfect blackbody spectrum known in nature. Let us start from this sentence and briefly recall blackbody properties and relations.
Calling $B_\nu(T)$ the blackbody intensity, the Planck law is:

$$B_\nu(T) = \frac{2h}{c^2}\frac{\nu^3}{e^{h\nu/kT}-1} = \frac{2h\nu^3}{c^2} n_\nu^{\mathrm{bb}}(T) = I_0 \frac{x^3}{e^x - 1} \tag{1.18}$$

where:

- ν is the frequency
- T is the blackbody temperature
- h is the Plank constant
- k is the Boltzmann constant

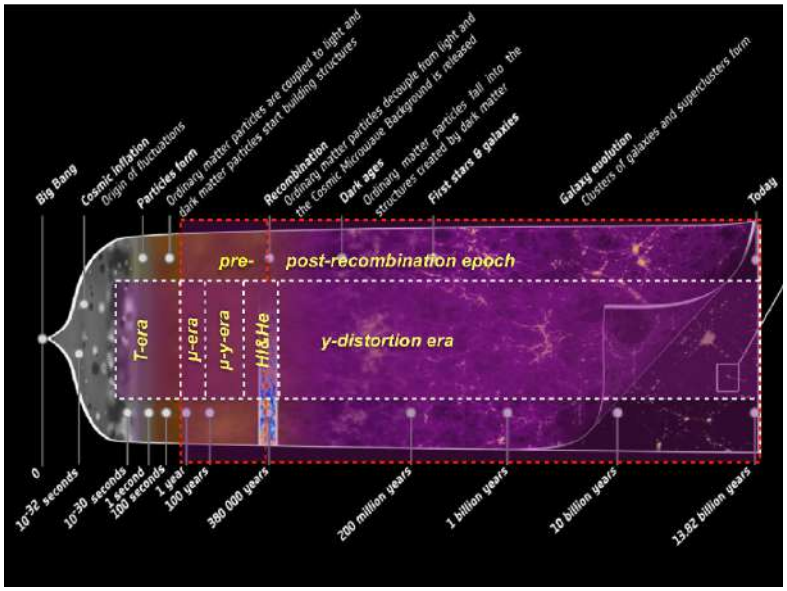

Figure 1.4: CMB spectral distortions arising during the thermal history of the Universe, in pre- and post-recombination era. Figure from [40]

- c is the speed of light
- $n_\nu^{\rm bb}(T) = 1/\left(e^{h\nu/kT} - 1\right)$ is the blackbody occupation number
- $X \equiv h\nu/kT$ is the dimensionless frequency (redshift-independent)
- $I_0 \equiv \left(2h/c^2\right)(kT/h)^3$

Depending on the relationship between $h\nu$ and kT, one can distinguish two limiting cases:

$$B_\nu(T) = \begin{cases} \dfrac{2\nu^2}{c^2} kT \quad h\nu \ll kT \quad \text{Rayleigh-Jeans limit} \\ \\ \dfrac{2h\nu^3}{c^2} e^{-h\nu/kT} \quad h\nu \gg kT \quad \text{Wien law} \end{cases} \tag{1.19}$$

Let us now introduce the total photon number, N_γ, and the energy density, ρ_γ, of the blackbody radiation. They both depend on the photon intensity I_ν, and they are integrated over all the photon energies and direction.

$$\rho_\gamma = \int \frac{I_\nu}{c} d\nu d\Omega = \frac{2h}{c^3} \int \frac{\nu^3}{e^x - 1} d\nu d\Omega = \frac{8\pi h}{c^3} \left(\frac{kT}{h}\right)^4 \int \frac{x^3}{e^x - 1} dx = \frac{8\pi^5 k^4 T^4}{15 c^3 h^3} = a_R T^4 \tag{1.20}$$

$$N_\gamma = \frac{2}{c^3} \int \frac{\nu^2}{e^x - 1} d\nu d\Omega = \frac{8\pi}{c^3} \left(\frac{kT}{h}\right)^3 \int \frac{x^2}{e^x - 1} dx = \frac{16\pi\zeta_3 k^3 T^3}{c^3 h^3} = b_R T^3 \tag{1.21}$$

where $a_R = 4\sigma/c$ is are the radiation constant, with σ the Stefan-Boltzmann constant. $\zeta_{\rm i}$ is the Riemann zeta function.

The important dependence to keep in mind is: $\rho_\gamma \propto T^4$ and $N_\gamma \propto T^3$.

Let us now suppose to increase the blackbody spectrum temperature from a temperature T to a temperature T' by adding some extra energy to the system. We define $\epsilon = \Delta\rho_\gamma/\rho_\gamma(T) \equiv \left(T'/T\right)^4 - 1$ and the photon temperature for small $\Delta\rho_\gamma/\rho_\gamma$ changes as:

$$\frac{\Delta T}{T} = (1+\epsilon)^{1/4} - 1 \simeq \frac{1}{4}\frac{\Delta\rho_\gamma}{\rho_\gamma} \tag{1.22}$$

However, also the photon number density must keep the blackbody relation, $N_\gamma \propto T^3$, thus simultaneously we need to add:

$$\frac{\Delta N_\gamma}{N_\gamma} = \left(\frac{T'}{T}\right)^3 - 1 = (1+\epsilon)^{3/4} - 1 \simeq 3\frac{\Delta T}{T} \tag{1.23}$$

Thus:

$$\frac{\Delta N_\gamma}{N_\gamma} \simeq \frac{3}{4}\frac{\Delta\rho_\gamma}{\rho_\gamma} \tag{1.24}$$

In addition, the photon occupation number needs to change as:

$$\begin{aligned} \Delta_\nu = n_{\rm bb}\left(T'\right) - n_{\rm bb}(T) = \frac{1}{e^{x'}-1} - \frac{1}{e^x - 1} = \\ = -x\partial_x n_{\rm bb}\frac{\Delta T}{T} + \mathcal{O}\left(\frac{\Delta T}{T}\right)^2 = \frac{x e^x}{(e^x-1)^2}\frac{\Delta T}{T} + \mathcal{O}\left(\frac{\Delta T}{T}\right)^2 \end{aligned} \tag{1.25}$$

where $x' = xT/T'$.
We can also define the function $G(x)$ which describes the spectrum of a temperature shift:

$$G(x) \equiv -x\partial_x n_{\rm bb} = \frac{x e^x}{(e^x-1)^2} \simeq \begin{cases} \dfrac{1}{x} & \text{for} \quad x \ll 1 \\ x e^{-x} & \text{for} \quad x \gg 1 \end{cases} \tag{1.26}$$

and for small $\Delta T/T$: $T\partial_T B_\nu \propto x^3 G(x)$.
As will be described later, $G(x)$ is created through the Compton scattering and photon creation processes such as double Compton (DC) and Bremsstrahlung emission.

1.6.2 The thermalization problem

The discussion presented here follows [40].
Under the assumption of a uniform adiabatic expansion of the Universe, the CMB spectrum (assuming also it started as a pure blackbody) is expected to be a perfect blackbody. However, processes that drive matter, radiation and energy out of thermal equilibrium can create momentary spectral distortions in the CMB spectrum. Nevertheless there has to be enough time from the creation

of the distortions to the present, in order to allow the CMB to thermalize again and to restore the blackbody shape. This is the so called *thermalization problem*.
The main actors of the thermalization process are the Compton scattering, the double Compton (DC) and the Bremsstrahlung emission. In particular Compton scattering redistributes the energy of the photons, i.e. shifting them at energies different from the original ones, while DC and Bremsstrahlung emission create new photons, adjusting the total number.
The photon Boltzmann equation describing the formation and the evolution of CMB fluctuations in both real and frequency space is:

$$\frac{\partial n}{\partial t} - Hp\frac{\partial n}{\partial p} = C[n] \tag{1.27}$$

where the spatial dependence is neglected, n is the photon occupation number, $H(t)$ is the Hubble expansion rate, p is the photon momentum and $C[n]$ is the collision term between photons and matter, which incorporates Compton scattering, Bremsstrahlung and DC.
It is possible to see that if collisions are neglected (thus $C[n]=0$), the solution of equation 1.27 has a proportionality: $n \propto a^{-3}$, which is the expected result for a blackbody spectrum conserved by the expansion of the Universe.

1.6.2.1 Compton scattering

Compton scattering is responsible for the redistribution of the energy of the photons. Photons undergo componization when they scatter off free electrons, which are present in the Universe until recombination. To account for these phenomena we can use the so called Kompaneets equation:

$$\left.\frac{\partial n}{\partial \tau}\right|_{\text{Compton}} \simeq \frac{\theta_\text{e}}{x_\text{e}^2}\frac{\partial}{\partial x_\text{e}} x_\text{e}^4\left[\frac{\partial}{\partial x_\text{e}} n + n(n+1)\right] \equiv \frac{\theta_\text{e}}{x^2}\frac{\partial}{\partial x} x^4\left[\frac{\partial}{\partial x} n + \frac{T_\gamma}{T_\text{e}} n(1+n)\right] \tag{1.28}$$

where τ is the Thomson optical depth, $d\tau = N_\text{e}\sigma_\text{T} c\, dt$, $x_\text{e} = h\nu/kT_\text{e}$ is the dimensionless frequency of the electron, $\theta_\text{e} = kT_\text{e}/m_\text{e}c^2$ is the dimensionless electron temperature, T_e is the electron temperature, m_e is the electron mass and T_γ is the photon temperature.
The Kompaneets equation is a diffusion equation, which describes the evolution of the photon occupation number n where photons are repeatedly scattered by thermal electrons in the isotropic medium.
The first term in the brackets of equation 1.28 describes Doppler broadening and Doppler boosting, while the last term accounts for the recoil effect and stimulated recoil, and are important for reaching full equilibrium in the limit of many scatterings.
Finally, it is important to remember that equation 1.28 is obtained from the Compton collision term under the assumptions that $h\nu \ll kT_\text{e}$ and $kT_\text{e} \ll m_\text{e}c^2$.
From equation 1.28 we can infer the Thomson scattering time scale, which de-

scribes the time needed for a photon to be scattered by a free electron

$$t_{\rm T} = (\sigma_{\rm T} N_{\rm e} c)^{-1} \simeq 2.7 \times 10^{20} X_{\rm e}^{-1} (1+z)^{-3} \ \ {\rm sec} \simeq 4.0 \times 10^{4} \left[\frac{X_{\rm e}}{0.16}\right]^{-1} \left[\frac{1+z}{1100}\right]^{-3} \ \ {\rm years} \tag{1.29}$$

where we assumed a standard cosmology with 24% of helium, and $X_{\rm e} = N_{\rm e}/N_{\rm H}$ the ionization fraction of the hydrogen.
This time scale can be understood when compared with the Hubble time scale, H^{-1} (remembering $z_{\rm eq} \simeq 3400$):

$$t_{\rm exp} = H^{-1} \simeq \begin{cases} 4.8 \times 10^{19} (1+z)^{-2} \ {\rm sec} & \text{radiation domination} \\ 8.4 \times 10^{17} (1+z)^{-3/2} \ {\rm sec} & \text{matter domination} \end{cases} \tag{1.30}$$

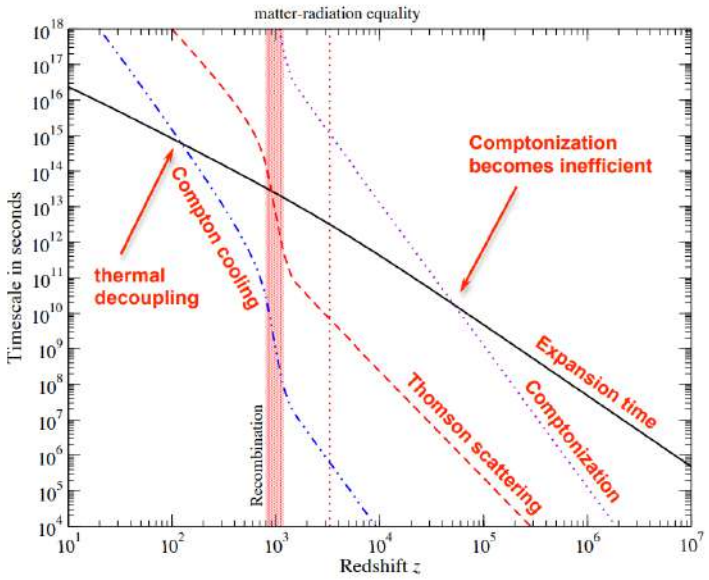

Figure 1.5: Comparison of the Comptonization, Compton cooling and Hubble expansion time-scale. Figure from [40]

As shown in figure 1.5, Thomson scattering timescale is much higher than the Hubble expansion rate until after decoupling ($z \simeq 10^3$), and there we start to see the primordial CMB fluctuations since isotropization process of CMB temperature and polarization anisotropies becomes inefficient.
Another important parameter we can infer from equation 1.28 is the Compton cooling time scale, which describes the time scale on which electrons transfer energy to the photons:

$$t_{\rm e\gamma} \simeq \frac{t_{\rm T}}{4\theta_{\rm e}} \simeq 4.9 \times 10^{5} t_{\rm T} \left[\frac{1+z}{1100}\right]^{-1} \simeq 1.2 \times 10^{29} (1+z)^{-1} \ {\rm sec} \tag{1.31}$$

Now, comparing $t_{\rm e\gamma}$ with the Hubble time scale, we can see that Compton scattering is much faster than the Hubble expansion rate until $z_{\mu y} \simeq 5\,10^4$, and after

it becomes inefficient (also see figure 1.5). $z_{\mu y}$ is the transition from a so-called μ-distortion to the y-type distortion. It is also important to underline that transition is not instantaneous and it takes a range of redshifts where an intermediate regime where the distortions originated is not only a superposition of these two.

1.6.2.2 Bremsstrahlung and double Compton emission

The redistribution of photons in energy by Compton scattering is not sufficient for thermalizing the radiation field and thus it is necessary to take into account the photon number described by the thermal Bremsstrahlung (BR) and the DC emission.
The collision term for BR and DC emission is:

$$\left.\frac{\partial n(\tau,x)}{\partial \tau}\right|_{\rm em} \frac{\mathrm{K_{BR}} e^{-x_{\rm e}} \mathrm{K_{DC}} e^{-2x}}{x^3}[1-n(\tau,x)(e^{x_{\rm e}}-1)] \tag{1.32}$$

where:

$$\mathrm{K_{BR}} = \frac{\alpha}{2\pi}\frac{\lambda_{\rm e^3}}{\sqrt{6\pi}\theta_{\rm e}^{7/2}}\left(\frac{T_{\rm e}}{T_\gamma}\right)^3 \sum_i Z_{\rm i}^2 N_{\rm i} \bar{g}_{\rm ff}\left(Z_{\rm i}, T_{\rm e}, T_\gamma, x_{\rm e}\right) \tag{1.33}$$

$$\mathrm{K_{DC}} = \frac{4\alpha}{3\pi}\theta_\gamma^2 I_{\rm DC} g_{\rm DC}\left(T_{\rm e}, T_\gamma, x\right) \tag{1.34}$$

$$\bar{g}_{\rm ff}(x_{\rm e}) \approx \begin{cases} \frac{\sqrt{3}}{\pi}\ln\left(\frac{2.25}{x_{\rm e}}\right) & \text{for } \; x_{\rm e} \leq 0.39 \\ 1 & \text{otherwise} \end{cases} \tag{1.35}$$

$$g_{\rm DC} \approx \frac{1+\frac{3}{2}x+\frac{29}{24}x^2+\frac{11}{16}x^3+\frac{5}{12}x^4}{1+19.739\theta_\gamma-5.5797\theta_{\rm e}} \tag{1.36}$$

with: $\alpha \approx 1/137$; $I_{DC} = \int x^4 n(1+n)\,\mathrm{d}x$; $\lambda_{\rm e} = h/m_{\rm e}c$.
From eq. 1.32 we can notice that the radiation field is at equilibrium for both BR and DC when there is a blackbody at the temperature of the electrons ($n_{\rm e} = 1/(e^{x_{\rm e}}-1)$); and due to the $1/x^3$ proportionality both BR and DC emission are very relevant at low frequencies.
For $z > 10^3$ and assuming $T_{\rm e} \approx T_\gamma$, eq. 1.33 is:

$$\mathrm{K_{BR}} \simeq 1.4\times10^{-6}\left[\frac{\bar{g}_{\rm ff}}{3.0}\right]\left[\frac{\Omega_{\rm b}h^2}{0.022}\right](1+z)^{-1/2} \tag{1.37}$$

and eq.1.34 is:

$$\mathrm{K_{DC}} \simeq 1.7\times10^{-20}(1+z)^2 \tag{1.38}$$

BR and DC emission are at equilibrium for $z_{\rm DC,BR} \simeq 3.7\times10^5\left(\left[\frac{\bar{g}_{\rm ff}}{3.0}\right]\left[\frac{\Omega_{\rm b}h^2}{0.022}\right]\right)^{2/5}$.
For $z > z_{\rm DC,BR}$ DC emission is dominant, while for $z < z_{\rm DC,BR}$ BR emission is dominant.

1.6.3 Types of spectral distortions from energy release

The types of spectral distortions can be summarized by saying that the Compton-y distortion is generated by scatterings between electrons and photons when the energy exchange is inefficient, while the chemical potential μ distortion when the energy exchange is efficient. We should also recall the transition between these types of spectral distortions is $z_{\mu y} \simeq 5 \times 10^4$.
This result can be better quantified starting from the photon evolution equation:

$$\frac{\partial n}{\partial \tau} \equiv \frac{\theta_e}{x^2}\frac{\partial}{\partial x} x^4 \left[\frac{\partial}{\partial x} n + \frac{T_\gamma}{T_e} n(1+n) \right] \tag{1.39}$$

where in this equation the photon emission is neglected and $n = n(\tau, x)$.

1.6.3.1 Small $y-$distortions

Assuming that for a number of scattering $\tau = 0$, $n = n_{bb} = 1/(e^x - 1)$, and then after a short time $\Delta\tau \ll 1$:

$$\begin{aligned} \Delta n \approx \frac{\Delta\tau\theta_e}{x^2}\frac{\partial}{\partial x} x^4 \left[\frac{\partial}{\partial x} n_{bb} + \frac{T_\gamma}{T_e} n_{bb}(1+n_{bb}) \right] \approx \frac{\Delta\tau\left(\theta_\gamma - \theta_e\right)}{x^2}\frac{\partial}{\partial x} x^4 n_{bb}(1+n_{bb}) \approx \\ \approx \Delta\tau\left(\theta_\gamma - \theta_e\right)\left[4x\, n_{bb}(1+n_{bb}) - x^2 n_{bb}(1+n_{bb})(1+2n_{bb})\right] \approx \\ \approx \Delta\tau\left(\theta_\gamma - \theta_e\right) G(x) \left[x\frac{e^x+1}{e^x-1} - 4 \right] \equiv \Delta\tau\left(\theta_\gamma - \theta_e\right) Y_{SZ}(x) \end{aligned} \tag{1.40}$$

where: $\partial_x n_{bb} = -n_{bb}(1+n_{bb}) = -e^x/(e^x-1)^2 = -G(x)/x$; and $(1+2n_{bb})$ $= (e^x+1)/(e^x-1) = = \coth(x/2)$. $Y_{SZ}(x)$ is the so called Compton-y distortion: named after Sunyaev-Zeldovich, this distortion arises when scattering have inefficient energy exchange.
The Compton-y parameter is:

$$y = \int_0^\tau \frac{k\left(T_e - T_\gamma\right)}{m_e c^2} \mathrm{d}\tau' = \int_0^\tau \frac{k\left(T_e - T_\gamma\right)}{m_e c^2} \sigma_T N_e c\, \mathrm{d}t' \tag{1.41}$$

which depends on the total amount of energy transfer as: $y = \frac{1}{4}\frac{\Delta\rho_\gamma}{\rho_\gamma}$; and on the net energy exchange as: $\frac{\Delta\nu}{\nu} \simeq 4\left(\theta_e - \theta_\gamma\right) \ll 1$, per scattering. This also means that eq. 1.40 applies as long as $|y| \ll 1$. In this regime ($|y| \ll 1$) there are two phenomena the Universe experiences: if $y < 0$ we speak about Compton cooling, and the energy is transferred from photons to electrons; while if $y > 0$ we speak about Comptonization, and the energy is transferred from electrons to photons. The former leads to the negative y-distortions, the latter to the positive ones, and $y > 0$ are the most common since the majority of processes in the Universe tend to heat the matter.
In figure 1.6 a comparison between the CMB blackbody spectrum and Comp-

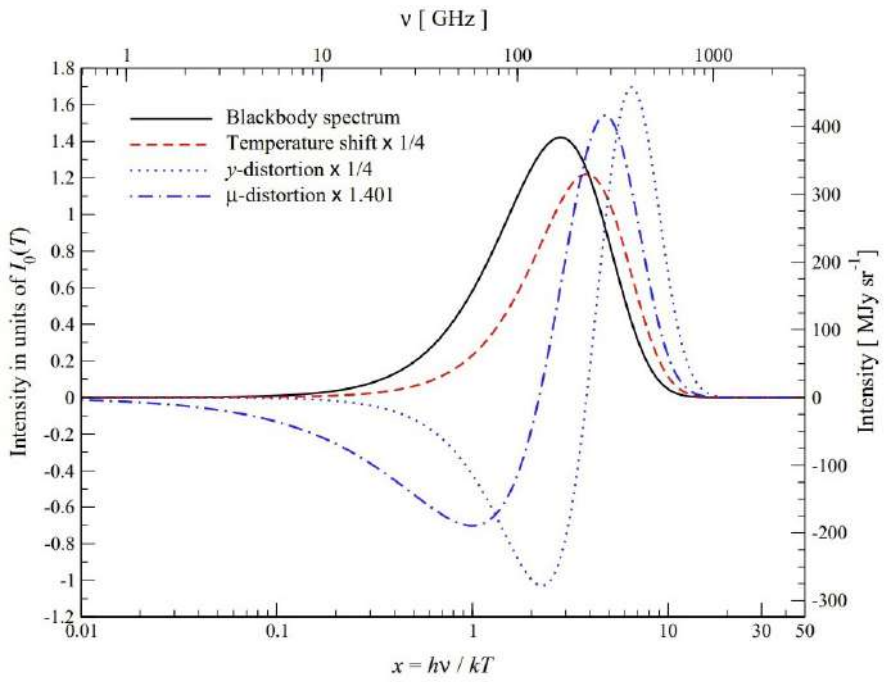

Figure 1.6: CMB Blackbody spectrum in black for T=2.726 K (right y-axis and upper x-axis). Temperature shift (G(x)) in red, Compton y-distortions ($Y_{SZ}(x)$) in dotted blue, and μ-distortions (M(x)) in dashed blue: left y-axis normalized by $I_0(T) = (2h/c^2)(kT/h)^3 \simeq 270$ MJy sr^{-1} $(T/2.726\text{K})^3$. Figure from [40]

ton y-distortions shape is shown. Indeed y-distortions have a deficit of photons in the Rayleigh-Jeans part and an increment of photons in the Wien part:

$$Y_{SZ}(x) = G(x)\left[x\frac{e^x+1}{e^x-1}-4\right] \approx \begin{cases} -\frac{2}{x} & \text{for } x \ll 1 \quad \rightarrow \frac{\Delta I}{I} \simeq \frac{\Delta T}{T} \simeq -2y \\ x(x-4)e^{-x} & \text{for } x \gg 1 \quad \rightarrow \frac{\Delta I}{I} \simeq \frac{\Delta T}{T} \simeq y(x-4) \end{cases} \tag{1.42}$$

As visible in figure 1.6, y-distortions vanishes at $\nu \simeq 217$ GHz.
Since Compton scattering does not change the photons number, $\Delta N_\gamma = 0$, thus $\Delta N_\gamma = 0 \propto \int x^2 Y_{SZ}(x)$, and the energy exchange of electrons with the initial blackbody spectrum is $4y = \Delta\rho_\gamma/\rho_\gamma$, with $\Delta\rho_\gamma \propto \int x^3 Y_{SZ}(x)$

1.6.3.2 Thermal Sunyaev-Zeldovich effect

CMB y-distortions can also be originated in galaxies clusters where hot electrons scatter CMB photons. This is known as the "thermal Sunyaev-Zeldovich

effect". Since $T_e \gg T_\gamma$, eq. 1.41 becomes:

$$y = \int_0^\tau \frac{k\left(T_e - T_\gamma\right)}{m_e c^2} \mathrm{d}\tau' \simeq \int_0^\tau \frac{k T_e}{m_e c^2} \mathrm{d}\tau' \approx \theta_e \tau \tag{1.43}$$

The thermal SZ effect is independent on redshift since the increase in CMB temperature with z makes the signal brighter, compensating for any dimming effects. This makes it a useful tool for studying distant clusters and understanding cosmic properties.
If a cluster is moving with respect to CMB, we need to take into account the Doppler kick, and this phenomenon is known as the kinematic SZ effect. In addition, if electrons velocities are fraction of c, relativistic corrections apply, and the Kompaneets equation as in eq. 1.28 is no longer valid.

1.6.3.3 μ-distortions

μ-distortions appear in the early Universe when many scatterings occur, redistributing the photons in frequency ($y \gg 1$ and $z > 5 \times 10^4$).
Assuming there are neither absorption nor emission phenomena, in presence of many scattering the spectrum is driven towards an equilibrium and thus eq. 1.39 is quasi-stationary:

$$0 \approx \frac{\theta_e}{x^2} \frac{\partial}{\partial x} x^4 \left[\frac{\partial}{\partial x} n + \frac{T_\gamma}{T_e} n(1+n) \right] \tag{1.44}$$

Introducing a constant integration μ_0, the solution is a Bose-Einstein (BE) spectrum with chemical potential μ_0:

$$n_{\mathrm{BE}} = \frac{1}{e^{x_e + \mu_0} - 1} \tag{1.45}$$

The chemical potential can be:

- $\mu_0 > 0$, when there is energy release or photon destruction
- $\mu_0 = 0$, in the condition of full equilibrium
- $\mu_0 < 0$, when there is energy extraction or photon injection

Now we want to derive an expression for the μ-distortions.
Let assume at the beginning we have a blackbody with T_γ, and to have electrons at the same temperature (T_γ=T_e=T_i). If we perturb the number density of the photon field by a quantity $\epsilon_N = \Delta N_\gamma / N_\gamma(T_i)$, and energy densities of the photon field by some $\epsilon_\rho = \Delta \rho_\gamma / \rho_\gamma(T_i)$, and then we wait until equilibrium (by Compton scattering):

$$N_\gamma^{\mathrm{BE}} = N_\gamma(T_i)(1+\epsilon_N) \equiv \frac{N_\gamma(T_f)}{G_2} \int \frac{x_f^2}{e^{x_f + \mu_0} - 1} d\, x_f \tag{1.46}$$

$$\rho_\gamma^{\rm BE} = \rho_\gamma(T_{\rm i})\big(1+\epsilon_\rho\big) \equiv \frac{\rho_\gamma(T_{\rm f})}{G_3}\int \frac{x_{\rm f}^3}{e^{x_{\rm f}+\mu_0}-1}\,d\,x_{\rm f} \tag{1.47}$$

with: $T_{\rm f}$ is the final electron temperature in the modified (Bose-Einstein spectrum) radiation field; $x_{\rm f} = h\nu/kT_{\rm f}$; $G_2 \approx 2.404$; and $G_3 \approx 6.494$. With these two equations we can fix $T_{\rm f}$ and μ_0 as a function of $\epsilon_{\rm N}$ and ϵ_ρ, and assuming the perturbations are small:

$$N_\gamma^{\rm BE} \approx N_\gamma(T_{\rm f})\big[1-\mu_0\mathscr{M}_2^{\rm c}\big] \approx N_\gamma(T_{\rm i})\left[1+3\frac{\Delta T}{T_{\rm i}}-\mu_0\mathscr{M}_2^{\rm c}\right] \tag{1.48}$$

$$\rho_\gamma^{\rm BE} \approx \rho_\gamma(T_{\rm f})\big[1-\mu_0\mathscr{M}_3^{\rm c}\big] \approx \rho_\gamma(T_{\rm i})\left[1+4\frac{\Delta T}{T_{\rm i}}-\mu_0\mathscr{M}_3^{\rm c}\right] \tag{1.49}$$

with $\mathscr{M}_2^{\rm c} \approx 1.3684$ and $\mathscr{M}_3^{\rm c} \approx 1.1106$. Defining $k^{\rm c} = 4\mathscr{M}_2^{\rm c} - 3\mathscr{M}_3^{\rm c} \approx 2.1419$, we can write an expression for μ_0 and $\dfrac{\Delta T}{T_{\rm i}}$:

$$\mu_0 \approx \frac{3}{k^{\rm c}}\left[\frac{\Delta\rho_\gamma}{\rho_\gamma}-\frac{4}{3}\frac{\Delta N_\gamma}{N_\gamma}\right] \tag{1.50}$$

$$\frac{\Delta T}{T_{\rm i}} \approx \frac{\mathscr{M}_2^{\rm c}}{k^{\rm c}}\frac{\Delta\rho_\gamma}{\rho_\gamma}-\frac{\mathscr{M}_3^{\rm c}}{k^{\rm c}}\frac{\Delta N_\gamma}{N_\gamma} \tag{1.51}$$

The following part is dedicated to obtain the spectral shape of the μ-distortions. Assuming $\mu_0 \ll 1$:

$$n_{\rm BE} = \frac{1}{e^{x_{\rm e}+\mu_0}-1} \approx \frac{1}{e^{x_{\rm e}}-1}-\frac{G(x_{\rm e})}{x_{\rm e}}\mu_0+\mathscr{O}\big(\mu_0^2\big) \tag{1.52}$$

Thus $\Delta n = -G(x_{\rm e})\mu_0/x_{\rm e}$ represents the distortion with respect to the blackbody at $T_{\rm e}$. Remembering that the final electron temperature $T_{\rm f} = T_{\rm e}$ also depends on μ_0, and fixing the μ-distortion $M(x)$ such that $\displaystyle\int x^2 M(x)\,d\,x = 0$, we get:

$$M(x) = G(x)\left[\alpha_\mu - \frac{1}{x}\right] \tag{1.53}$$

where $\alpha_\mu = \pi^2/18\zeta(3)$, and having integrated Δn so that $\displaystyle\int x^2\Delta n\,d\,x = -2\mu_0\int \frac{x}{e^x-1}\,d\,x = -\mu_0\pi^2/3$.

In the end, normalizing the relative change of the photon energy density $\Delta\rho/\rho = 1$, the spectral shape of the μ-distortion is:

$$M^*(x) = \frac{3}{k^{\rm c}}M(x) \approx \frac{3}{k^{\rm c}}G(x)\left[\alpha_\mu-\frac{1}{x}\right] \approx \begin{cases} -\dfrac{3}{k^{\rm c}}\dfrac{1}{x^2} & \text{for } x \ll 1 \quad \to \dfrac{\Delta I}{I} \simeq \dfrac{\Delta T}{T} \simeq -\dfrac{\mu_0}{x} \\ \dfrac{3}{k^{\rm c}}\alpha_\mu\, x\, e^{-x} & \text{for } x \ll 1 \quad \to \dfrac{\Delta I}{I} \simeq \dfrac{\Delta T}{T} \simeq \dfrac{1}{2}\mu_0 \end{cases} \tag{1.54}$$

As depicted in figure 1.6, $M(x)$ is shifted towards lower frequencies with respect to $Y_{\rm SZ}(x)$. This also makes the two kinds of spectral distortions distinguishable.

1.6.3.4 Photon production in the μ-era

So far our focus has been solely on Compton scattering as the factor altering the photon field. However in the μ-distortions era also the effects of BR and DC have to be taken into account. By taking into account both emission and absorption, and assuming that the spectrum undergoes changes across a series of quasi-stationary stages, eq. 1.44 for the CMB spectrum becomes:

$$0 \approx \frac{\theta_e}{x^2}\frac{\partial}{\partial x}x^4\left[\frac{\partial}{\partial x}n + \frac{T_\gamma}{T_e}n(1+n)\right] + \frac{K}{x^3}[1-n(e^{x_e}-1)] \tag{1.55}$$

One can find the approximate solution to the differential equation for $\mu(z, x_e) \ll 1$ by inserting $n \approx \frac{1}{(e^{x_e}-1)} - \mu(z, x_e)\frac{G(x_e)}{x_e}$, and assuming $x_e \ll 1$:

$$\mu(z, x_e) \approx \mu_0(z)\, e^{-x_c(z)/x_e} \tag{1.56}$$

where x_c represents the critical frequency, and during the thermalization period it is estimated that $x_c(z) \simeq 10^{-3} \div 10^{-2}$. This range considers the interplay between photon emission and absorption, along with Compton scattering of the photons.
Eq. 1.56 enables the computation of the total photon production rate across redshifts. The resulting differential equation for $\mu_0(z)$ has a specific solution in the case of a single energy release $\left.\frac{\Delta\rho_\gamma}{\rho_\gamma}\right|_i$:

$$\mu_0(z) \approx \frac{3}{k^c}\left.\frac{\Delta\rho_\gamma}{\rho_\gamma}\right|_i e^{-\left(z_i/z_\mu\right)^{5/2}+\left(z/z_\mu\right)^{5/2}} = \mu_i \mathcal{J}(z_i, z) \tag{1.57}$$

where μ_i is defined as $\mu_i = \frac{3}{k^c}\left.\frac{\Delta\rho_\gamma}{\rho_\gamma}\right|_i$, and $\mathcal{J}(z_i, z)$ is the spectral distortion visibility between the injection redshift z_i and z (with $z < z_i$). It reflects the fraction of energy injected at z_i still visible as a distortion at z. When $\mathcal{J}(z_i, z)$ is close to 1, most of the energy remains in the distortion; when it's $\ll 1$, energy has largely thermalized, causing a temperature shift. For a single energy release at $z > z_{DC} \approx 1.98 \times 10^6$, the present chemical potential is heavily suppressed. Continuous energy release in the μ-era allows predicting today's final distortion as (neglecting any extra photon production):

$$\mu_0 \approx \left.\frac{3}{k^c}\frac{\Delta\rho_\gamma}{\rho_\gamma}\right|_\mu \approx \frac{3}{k^c}\int_{z_{\mu y}}^{\infty}\frac{d\left(Q/\rho_\gamma\right)}{dz}\mathcal{J}\left(z', 0\right)dz' \tag{1.58}$$

where $d\left(Q/\rho_\gamma\right)/dz$ denotes the energy release relative to the CMB blackbody and relies on the specific energy release mechanism (refer to following section 1.6.4).

1.6.3.5 Transition between μ and y distortions

As already said, transition between μ and y distortions is not a step function and the distortions in the intermediate-regime ($z \simeq 10^4 \div 3 \times 10^5$) are not only originated by the superposition of μ and y distortions, but contain valuable time-dependent additional information.
Figure 1.7 depicts the thermalization Green's function, $G_{\rm th}(\nu, z_{\rm h})$ (the distortion response) for single energy release. As shown in the figure, temperature shift is created at $z >$ few 10^6, μ-distortions are visible around $z \simeq 3 \times 10^5$, and y-distortions from $z < 10^4$. In figure 1.8 the residual (non-μ/non-y) distortions also called r-type distortions) is depicted. This signal contains information about the time-dependence of the energy-release process and detection limits for different energy release scenarios.

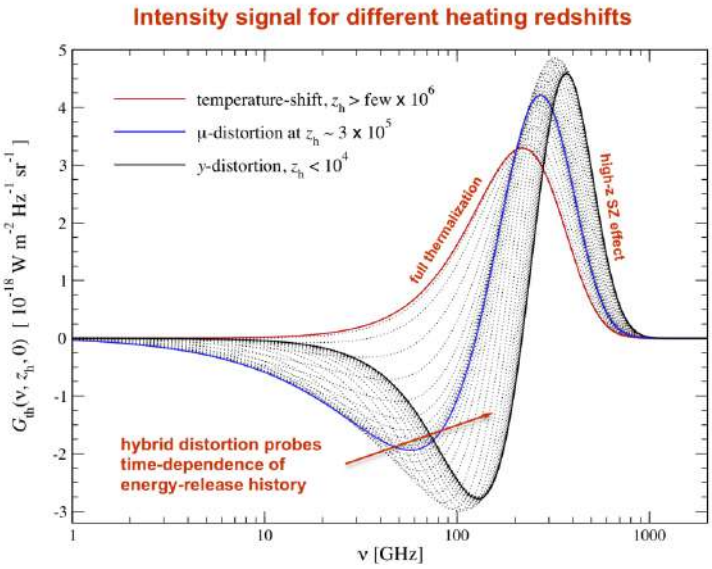

Figure 1.7: Change in the CMB spectrum after a single energy release at different heating redshifts, $z_{\rm h}$: thermalization Green's function, $G_{\rm th}(\nu, z_{\rm h})$. Figure from [40]

1.6.4 CMB spectral distortions signal from various scenarios

We briefly report some of the main distortion signals expected within ΛCDM and more exotic sources of distortions. A picture of the relevant ΛCDM distortions is in figure 1.9.

- Reionization and structure formation.
  Compton y-distortion is caused during reionization by radiation sources like supernova feedback and structure formation shocks. Indeed, they heat the intergalactic medium at low redshifts ($z < 10$), producing hot electrons that partially up-scatter CMB photons. This is the most substantial expected distortion in ΛCDM, and estimations on its amplitude

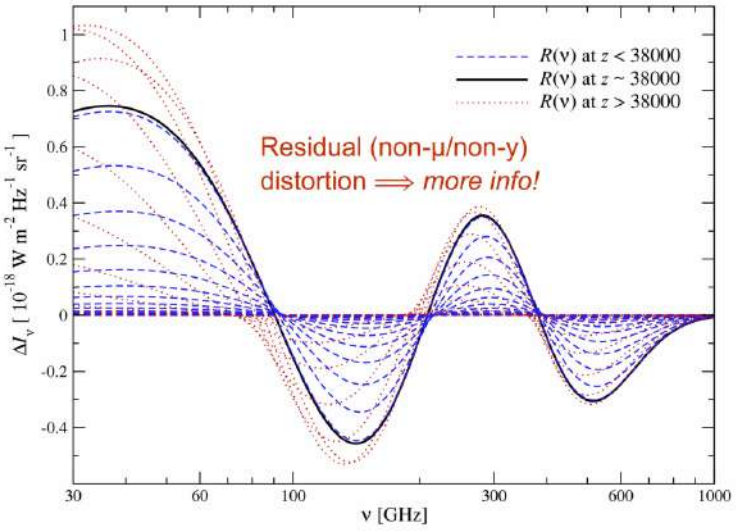

Figure 1.8: Change in the CMB spectrum after a single energy release at different heating redshifts, z_h: residual distortion. Figure from [40]

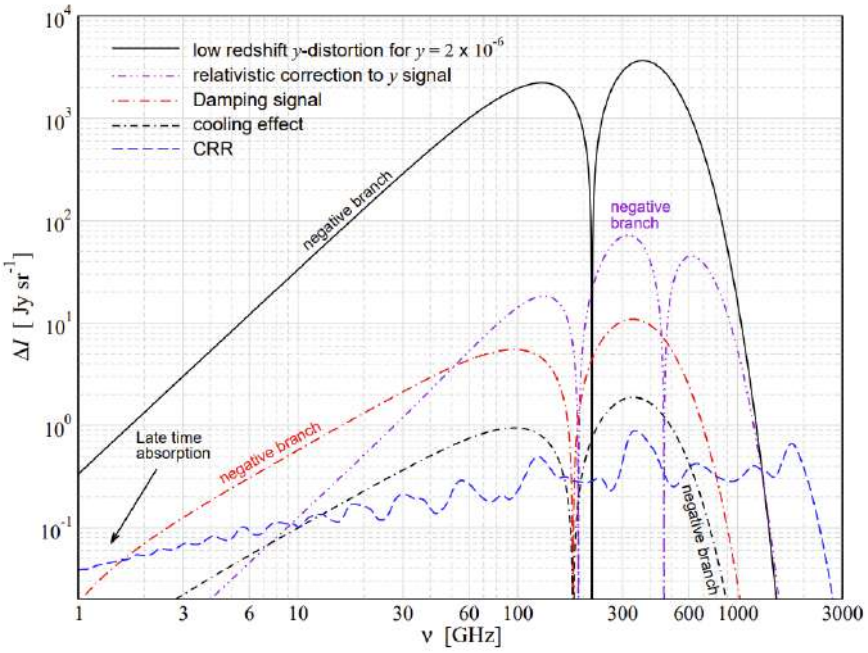

Figure 1.9: Comparison of several CMB monopole distortion signals produced in the standard ΛCDM cosmology. Figure from [40]

are around $y \sim$few $\times 10^{-6}$. In figure 1.9 they are plotted with a fiduciary value of $y \simeq 2 \times 10^{-6}$.

It is also possible to compute the relativistic corrections due to the high gas temperature ($k T_e \simeq 1$ keV). This signal differs from the distortions produced in the early Universe, as visible in figure 1.9. This correction could

provide insights into the average temperature of the intergalactic medium, offering a potential solution to the missing baryon problem.

- Damping of primordial small-scale perturbations.
  Another distortion of the CMB spectrum is caused by the damping of small-scale fluctuations of the CMB temperature set up by inflation at wavelength $\lambda < 1$ Mpc. This mechanism involves mixing blackbodies with different temperatures through Thomson scattering. If we consider blackbody photons inside a box at two temperatures T_1 and T_2 ($T_1 < T_2$), and mean $T_B = 1/2(T_1 + T_2)$, Thomson scattering mixes the two photon distributions without altering the photon number or energy. The averaged distribution, though not a pure blackbody, exhibits a y-type distortion in the Wien tail at the second order in temperature difference. This initiates the thermalization process, with repeated Compton scattering gradually transforming the distortion into a μ-distortion.
  The distortion is sensitive to the amplitude and shape of the power spectrum at very small scales (wavenumbers 1 $\text{Mcp}^{-1} < k < 2 \times 10^4$ Mcp^{-1}: perturbation modes with 1 $\text{Mcp}^{-1} < k < 50$ Mcp^{-1} create y-distortions, while modes with 50 $\text{Mcp}^{-1} < k < 2 \times 10^4$ Mcp^{-1} yield μ-distortions. Accessing these scales through alternative methods is challenging, thus spectral distortions provide a promising new way for constraining inflation within this regime.
  The study of damping of primordial small-scale perturbations was already used to derive first upper limits on the spectral index of scalar perturbations, yielding $n_S < 1.6$ from COBE-FIRAS [37].
  Moreover, the damping signal is also sensitive to primordial non-Gaussianity leading to a spatially varying spectral signal that correlates with CMB temperature anisotropies at large angular scales
  In figure 1.9 the damping signal is depicted with n_S =0.9645. The uncertainty of this signal is strongly related to the uncertainty in the measurement of n_S, that in the ΛCDM is described by a sum of μ and y-distortion with $\mu \approx 2.0 \times 10^{-8}$, $y \approx 3.6 \times 10^{-9}$ and a non-vanishing overall residual at the level of $\simeq$ 20% - 30%.

- Adiabatic cooling for baryons.
  Ordinary matter's adiabatic cooling extracts energy from the CMB photon bath through Compton scattering, resulting in a small yet inevitable distortion directly influenced by the baryon density and helium abundance. The distortion is characterized by negative μ- and y-parameters at the level of $\simeq$few $\times 10^{-9}$.
  The signal is shown in figure 1.9 using Planck collaboration parameters [8]. Its uncertainty is at the $\simeq$ 1% level in ΛCDM, and it cancels part of the damping signal. Nevertheless, it is approximately an order of magnitude weaker and cannot be distinguished within the sensitivity level of next generation CMB spectrometers.
  Additional interactions of dark matter with photons, electrons or protons

could further increase the cooling distortion. This allows placing interesting constraints on the nature of dark matter and its interactions with the standard sectors.

- The cosmological recombination radiation.
  The cosmological recombination is associated with the emission of photons in free-bound and bound-bound transitions of hydrogen and helium. This process causes a small distortion of the CMB and the redshifted recombination photons should still be visible as a tiny spectral distortion ($\simeq$ nK-μK level) present at mm to dm wavelength, called the cosmological recombination radiation (CRR). The amplitude of the CRR depends directly on the number density of baryons in the Universe.
  Furthermore the helium abundance affects the detailed shape of the recombination lines. The positions and widths of these lines depend on when and how rapidly the Universe recombined. Consequently, the CRR provides an independent way to constrain cosmological parameters and map the recombination history. In particular, CRR could provide a new way for directly studying the conditions of the Universe at $z \simeq 10^3$ (HI - recombination), $z \simeq 2000$ (HeI - recombination) and $z \simeq 6000$ (HeII - recombination). Moreover, if something unexpected occurred during various stages of the recombination epoch, atomic species would react, possibly producing additional distortion features that may exceed those of the normal recombination process. This will provide a unique way to distinguish pre- from post-recombination energy release.

- Dark matter annihilation.
  Today the origin and production mechanism of dark matter remain still unclear.
  However, in the ΛCDM model, the WIMP scenario predicts that dark matter should have undergone low-level annihilation throughout the history of the Universe. For specific dark matter models, the level of annihilation around the recombination epoch is tightly constrained with the CMB anisotropies. Indeed, the annihilation of dark matter can cause changes in the ionization history around last scattering ($z \simeq 10^3$), leading to changes of the CMB temperature and polarization anisotropies.
  The current challenge is represented by the fact that for the standard WIMP scenario the expected signal is even smaller than the adiabatic cooling distortion.

- Decaying particle scenarios.
  The CMB spectrum could also be a valuable tool to place constraints on decaying particles in the pre-recombination epoch. This is particularly relevant for decaying particles with lifetimes $t_X \simeq 10^8 \div 10^{11}$s, as the exact shape of the distortion encodes when the decay occurred. Such decays could furthermore create a unique spectral signature that can be distinguished from simple energy release.

This would be another opportunity to study early-Universe particle physics, and this exploration could contribute insights into the physics of gravitinos, axions, and primordial black holes.

- Anisotropic (spectral-spatial) CMB distortions.
  Anisotropies in the spectrum of the CMB are expected in the standard ΛCDM model.
  The primary contribution to anisotropies is due to the Sunyaev-Zeldovich effect caused by the hot plasma inside clusters of galaxies. During the early stages of the Universe, anisotropies in the μ and y distortions are expected to be tiny (relative perturbations $< 10^{-4}$) unless strong spatial variations in the primordial heating mechanism are expected. Another guaranteed source of anisotropic signal arises from Rayleigh scattering of CMB photons in the Lyman-series resonances of hydrogen around the recombination era. Similarly, the resonant scattering of CMB photons by metals appearing in the dark ages or scattering in the excited levels of hydrogen during recombination can lead to anisotropic distortions.

Chapter 2

COSmological Monopole Observer

In this chapter, I will introduce the COSMO (COSmological Monopole Observer) experiment.
COSMO is the focus of my Ph.D. thesis, for which I contributed to develop and test the readout electronics. The primary objective of the COSMO experiment is to measure the CMB isotropic component of the y-distortions utilizing a cryogenic differential Fourier Transform Spectrometer.
Here, I will provide a review of the experiment, focusing on the methodology to extract such information from the monopole, and then discussing the design and components themselves.

2.1 Introduction to COSMO

COSMO is a cryogenic pathfinder experiment aimed at measuring the CMB isotropic component of the y-distortions. It will be operated on the Antarctic plateau at the Italian-French station Concordia (Dome-C), this ground-based experiment will benefit from exceptional logistics support, including reliable power, communication infrastructure, and resident personnel for operational efficiency. The site selection is based on its optimal conditions for astronomical observations in millimeter waves, facilitated by favorable atmospheric conditions and low precipitable water vapor levels. These conditions theoretically enable the separation of spectral distortions from the atmospheric emission and galactic and extra-galactic foregrounds. In figure 2.1, it is possible to observe the isotropic brightness of the various signals. As it is shown, spectral distortions are very tiny with respect to the other isotropic backgrounds, such as the atmospheric emission, the astrophysical foregrounds, the instrument emission, and the CMB monopole itself, which is observed by COSMO. Finally, in our pursuit to measure spectral distortions, COSMO must detect the absolute photon flux.

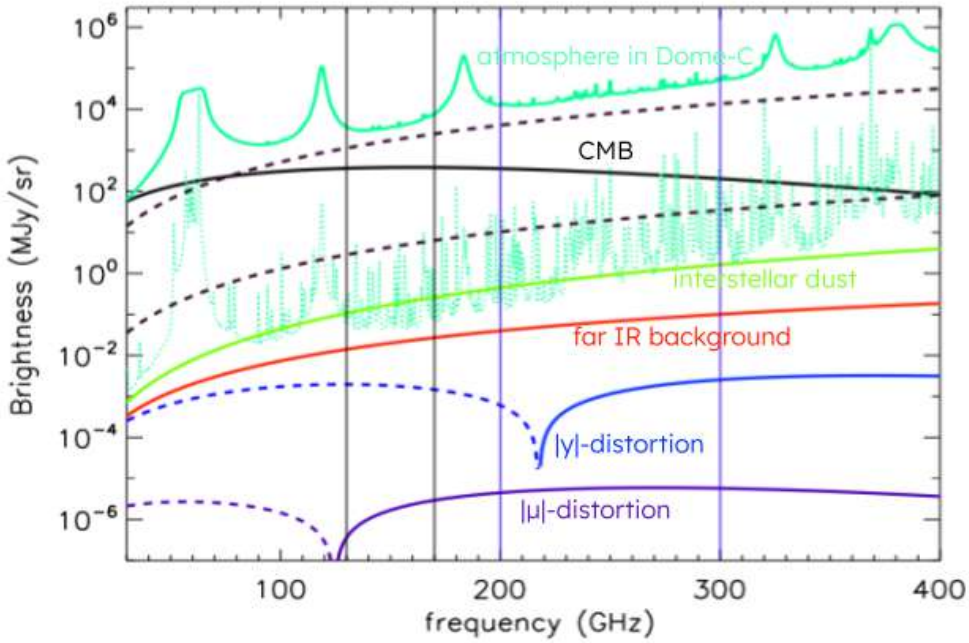

Figure 2.1: Isotropic brightness. From top to bottom in continuous lines: Antarctic atmosphere in Dome-C at zenith (solid green); CMB (solid black); interstellar dust - Galactic average (green); far infrared background from unresolved galaxies (solid red); absolute value of the y-distortion in blue (negative branch is dashed); absolute value of the μ-distortion in violet (negative branch is dashed). The two black dashed lines are the expected emission of the window of the receiver: the upper line is for the ground based pathfinder, while the lower line is the balloon-borne implementation of COSMO. The dotted light green line represents the atmospheric emission at stratospheric balloon altitude at zenith. The two couples of vertical lines (black and violet) represent the observation bands of COSMO in its ground-based implementation. [41]

2.2 COSMO: method

COSMO is a cryogenic differential Fourier Transform Spectrometer (FTS) in Martin Puplett Interferometer (MPI) configuration [42, 43]. A 3D rendering of the FTS is in figure 2.2.
MPI, with its two input ports, has wire grid polarizers (typically made by Tungstenium), and a movable delay line introduces a controlled delay between the two beams. This delay is varied during the observation, allowing the interferometer to disentangle different frequencies. A detector measures the resulting interferogram, which is a pattern of intensity variations as a function of the introduced delay. This interferogram is then Fourier anti-transformed to obtain the spectrum of the incoming radiation.
The instrument is intrinsically differential since it measures the difference between the powers of two input beams, having two input ports. Thus COSMO

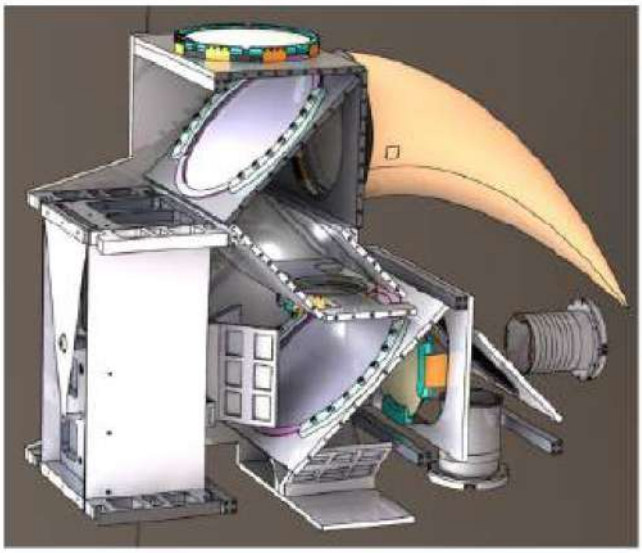

Figure 2.2: 3D rendering of the FTS

will have one port looking at the sky (port A) and the other one looking at the internal cryogenic reference blackbody (port B) and it will measure the spectrum of the difference in brightness at the two input ports. For calibration purposes only another blackbody at different temperature replaces the sky.
A simplified instrument model can be described as:

$$I_{\rm sky}(x) = R \int_0^\infty A\Omega(\sigma)\left[B_{\rm sky}(\sigma) - B_{\rm ref}(T_{\rm ref},\sigma)\right]\epsilon(\sigma)[1+\cos(4\pi\sigma x)]\,d\sigma \qquad (2.1)$$

where: $I_{\rm sky}$ is the signal measured by the detector as a function of the optical path difference, x, between the two arms of the interferometer (which is scanned by means of a moving roof-mirror); σ is the wave-number; $A\Omega(\sigma)$ is the optical throughput of the detector; $B_{\rm sky}(\sigma)$ is the sky brightness present at input port A; $B_{\rm ref}(T_{\rm ref},\sigma)$ is the brightness of the reference blackbody at temperature $T_{\rm ref}$ present at input port B; $\epsilon(\sigma)$ is the spectral efficiency of the instrument; the constant R is the responsivity of the instrument.
For calibration purpose, an external blackbody at a known temperature $T_{\rm ext}$ fills input port A, and the measured signal is:

$$I_{\rm cal}(x) = R \int_0^\infty A\Omega(\sigma)[B_{\rm ext}(T_{\rm ext},\sigma) - B_{\rm ref}(T_{\rm ref},\sigma)]\,\epsilon(\sigma)[1+\cos(4\pi\sigma x)]\,d\sigma \qquad (2.2)$$

Since the quantity we are interested in is $B_{\rm sky}(\sigma)$, the process is straightforward: anti-transforming equation 2.2 one can get the quantity $RA\Omega(\sigma)\epsilon(\sigma)$, which is then plugged in equation 2.1 to estimate $B_{\rm sky}(\sigma)$.
It is important that $B_{\rm sky}$ and $B_{\rm ref}$ are cryogenic and close to $T_{\rm CMB}$ in order to avoid saturation or non-linearity effects in the detectors.
As shown in figure 2.1, even if Dome-C is one of the best site on Earth for

millimeter wave observations being extremely cold and dry, we still have to deal with atmospheric emission. First of all the impact of atmospheric emission can be mitigated selecting a suitable range of frequencies. Indeed COSMO will cover the frequency bands 130-170 GHz and 200-300 GHz. Scanning strat-

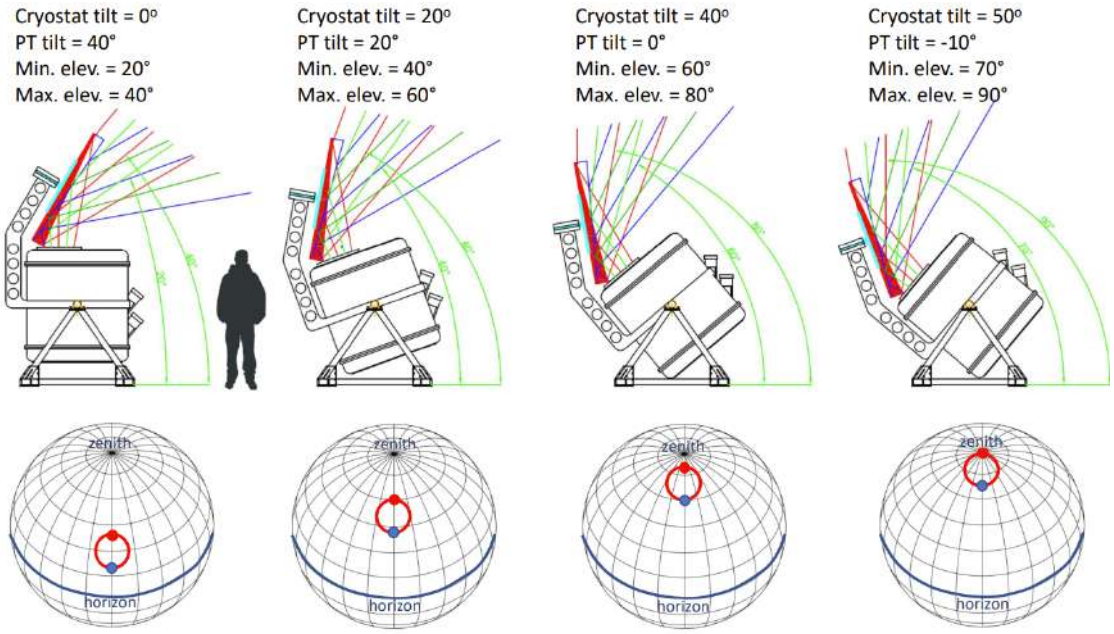

Figure 2.3: COSMO scan strategy. Up: The COSMO instrument with the external spinning wedged flat mirror, steering the instrument beam in the sky while spinning. The mirror is sketched in two positions (red and blue) corresponding to maximum and minimum elevation of the beams. Down: beam scan pattern over the celestial sphere. The two dots mark represent the maximum and minimum elevations. [41]

egy is the other relevant tool: COSMO will perform fast elevation scans in order to separate atmospheric emission and its long-term fluctuations from the monopole of the sky brightness. A fast spinning (>600 rpm), wedged flat mirror steers the bore-sight direction on a circle, 20 ° in diameter, scanning several times a range of elevations (and the corresponding optical depths of the atmosphere) while the cryogenic interferometer scans the optical path difference. The maximum optical path difference introduced by the moving roof mirror is +/− 2 cm, corresponding to a spectral resolution of about 10 GHz.
COSMO scanning strategy is depicted in figure 2.3.
Note that the latitude of the Dome-C site (75° S) allows for crosslinked sky scans * at constant elevation, which are not possible from the South Pole, similar to those obtained in circumpolar stratospheric balloon flights, as visible in the lower part of the figure 2.3. Indeed, the geographic latitude of Dome-C allows for these crosslinked scans because the site's position lets the telescope cover

*Crosslinked sky scans refer to scanning the sky in such a way that different parts of the sky are observed multiple times, but from different angles or with intersecting scan paths. This helps in reducing systematic errors and improving the overall quality of the data.

the sky in a way that keeps the elevation constant while scanning different regions of the sky.
With this scanning path, the recorded interferogram (equation 2.1) is the one due to the monopole, which is constant during the sky scan plus the one due to atmospheric emission, which is modulated by the beam elevation variations during the sky scan. An example of the expected interferogram is reported in

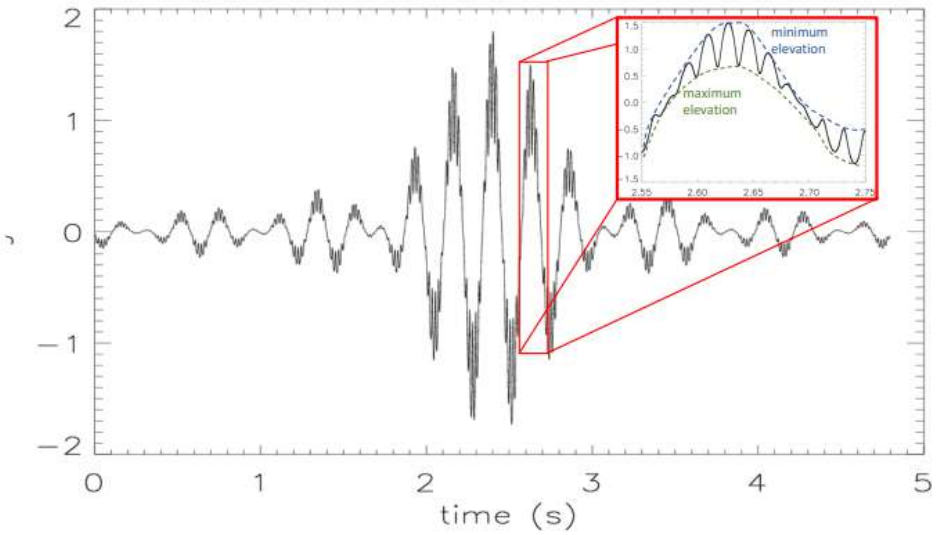

Figure 2.4: Example of expected interferogram obtained while the flat wedged mirror is spinning. For each position x of the roof mirror in the MPI (corresponding to a different time on the abscissa), the signal changes due to the fast variation of the observed elevation. In this example one full scan of the roof mirror is shown (at a mechanical speed of ~0.25 cm/s, from -1.27 cm to +1.27 cm of optical path difference). The zoomed inset shows interferograms corresponding to several elevations in between the maximum and minimum positions. [41]

figure 2.4. To be significant, the resulting interferogram needs to be properly sampled (I will treat later the problem of sampling, in chapter 4).
Once we get the interferograms modulated by different elevations e, then we can antitrasform them to estimate the measured brightness spectra for the different elevations. The resulting antitrasformed interferogram is a function of the frequency. For each of them we use the $\csc(e)$ law to extrapolate to zero air-mass, and thus to estimate the isotropic component of the sky brightness (see figure 2.5). COSMO will measure one interferogram every few seconds, allowing to remove slower atmospheric fluctuations, mitigating the effects of $1/f$ noise, which is characteristic of the atmospheric fluctuations.

2.3 COSMO: design and components

The experiment is housed in a modified thermally insulated ISO20 shipping container to protect the electronic instrumentation from the extremely low tem-

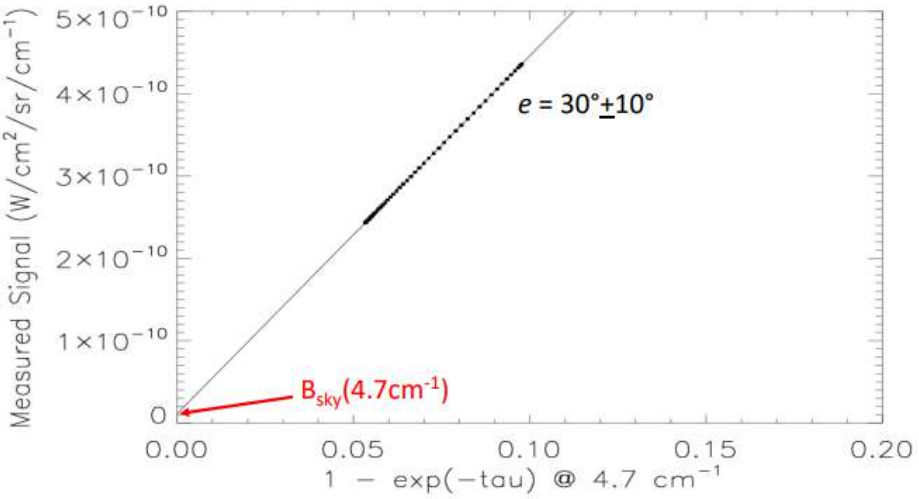

Figure 2.5: Cosecant law extrapolation to zero air-mass to estimate the isotropic component of the sky brightness for each frequency. [41]

perature, as COSMO will operate during the Antarctic winter. In a section of the shelter, the openable roof allows the receiver to observe the sky. The shelter is mounted on a palafitte on top of a hardened snow berm. A 3D rendering of the COSMO specific shelter is in figure 2.6.

2.3.1 The optical system

The instrument is designed with and optical aperture of 22 cm in diameter, producing a diffraction limited beam at the longest wavelength (2.4 mm) of $\sim 0.7^{\circ}$ FWHM.
The foreseen FWHM of the main beam is around 20°, the first side-lobe level is below -15 dB and the far side-lobe level is below -30 dB. The choice of the optical aperture is a tradeoff between the size of the optical aperture and the need to monitor the effects of anisotropic foregrounds. A sketch of the optical setup is in figure 2.7.

2.3.2 The cryogenic FTS

The telescope and the FTS are located inside a cryostat to minimize their radiative background, as shown in figure 2.8.
The cryogenic FTS is a MPI, with two delay lines terminated with roof-mirrors. The interferogram is obtained by introducing a variable difference in the lengths of the two delay lines. This is achieved through the linear movement of one of the two roof-mirrors.

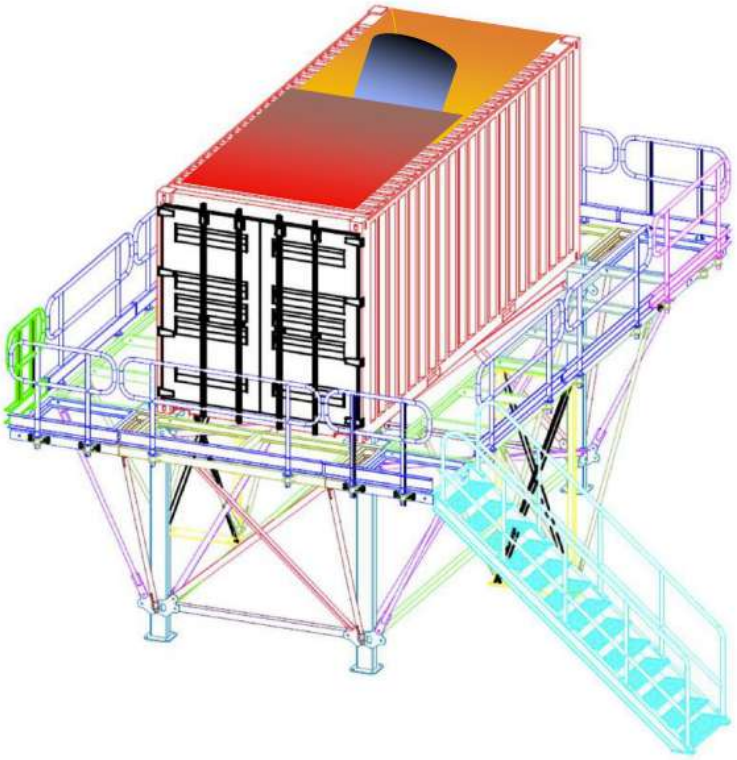

Figure 2.6: 3D rendering of the COSMO shelter.

The radiation coming from the FTS is coupled to the detectors by two arrays of nine multimoded feed-horns, working in the 130-170 GHz and 200-300 GHz range, respectively. The low-frequency array consists of Winston cone antennas, while the high-frequency array hosts linear profiled antennas, a picture in figure 2.9. Specifically, the low-frequency array consists of 7 plates and a circular waveguide floor, while the high-frequency array is one piece with a separate circular waveguide floor. Both are made of ergal (Al7075) and will be tightened with ergal screws to ensure compatibility with the rest of the focal plane and to avoid differential thermal contractions during the cryostat cooling phase. The output beam from the FTS is split into two exit ports by the output polarizer. In each output port, a focal plane array is placed, consisting of multimode horn antennas feeding multimode lumped elements kinetic inductance detectors (LEKIDs). The reflected beam serves the high-frequency band array, while the transmitted one serves the low-frequency band array.
The 18 COSMO LEKIDs will be made by 30 nm thick Aluminum, on a 4 inch Si wafer. The designed detectors' time constant is $\tau \sim 60\ \mu$s. In order to maximize the signal-to-noise ratio, the waveguides area and the KIDs are multimode, allowing the propagation of 10 to 19 modes in the 130-170 GHz range and of 23 to 42 modes in the 200-300 GHz range.
COSMO cryostat will have two pulse tube refrigerators (model SRP-082B2S-

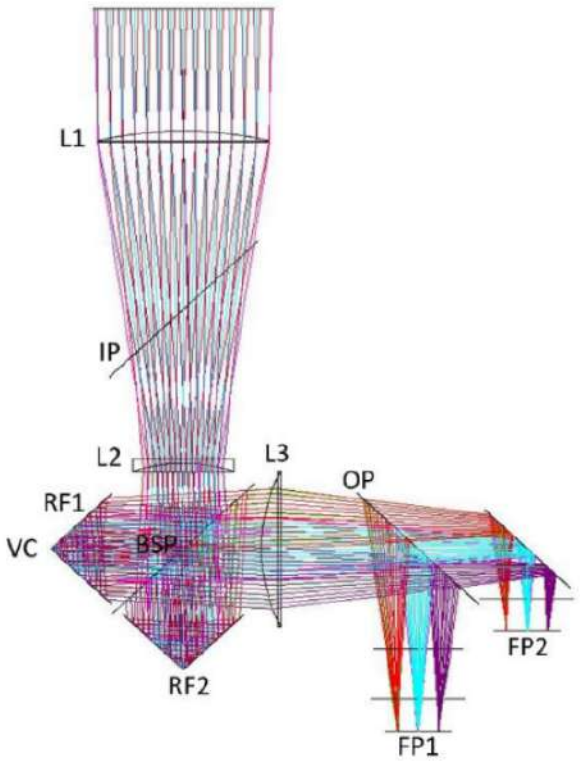

Figure 2.7: Ray tracing simulation of the focusing optics. L1 (the primary lens) is the light collector lens, L2 (the secondary lens) produces a nearly parallel beam for the FTS, L3 (the tertiary lens) focuses radiation of the focal planes FP1 and FP2. The Differential FTS is constituted by the input polarizer IP, the beamsplitter polarizer BSP, the roof mirrors RF1 and RF2 (the delay of the spectrometer is achieved by moving one of the two), the output polarizer OP. The input polarizer IP transmits radiation from the sky and reflects radiation from the cryogenic reference blackbody. [41]

F70H from Sumitomo Heavy Industries), each with a cooling power of 35 W at 45 K on the first stage and 0.9 W at 4.2 K at the second stage. Additionally, the second stage uses 6061 Al vacuum shell, drum-like structures of fiberglass tubes to support the two stages, and optimized thermal shields for the optical window and the lower temperature apertures.
The COSMO cryostat is similar to the one used for the QUBIC experiment [44], see figure 2.10.

The interferometer will be cooled at a temperature of 2.7 K to mitigate the systematic effects in the measurement of the CMB, while the detectors will be cooled at 250 mK by a sub-K ^{3}He evaporation cooler.
Inside the cryostat, there will also be a cryogenic reference blackbody, one of the key element of the experiment. This is a cavity with the inner surface covered by a microwave absorber. The cavity structure is made of copper to achieve a very uniform temperature. The accuracy of the blackbody is closely related to

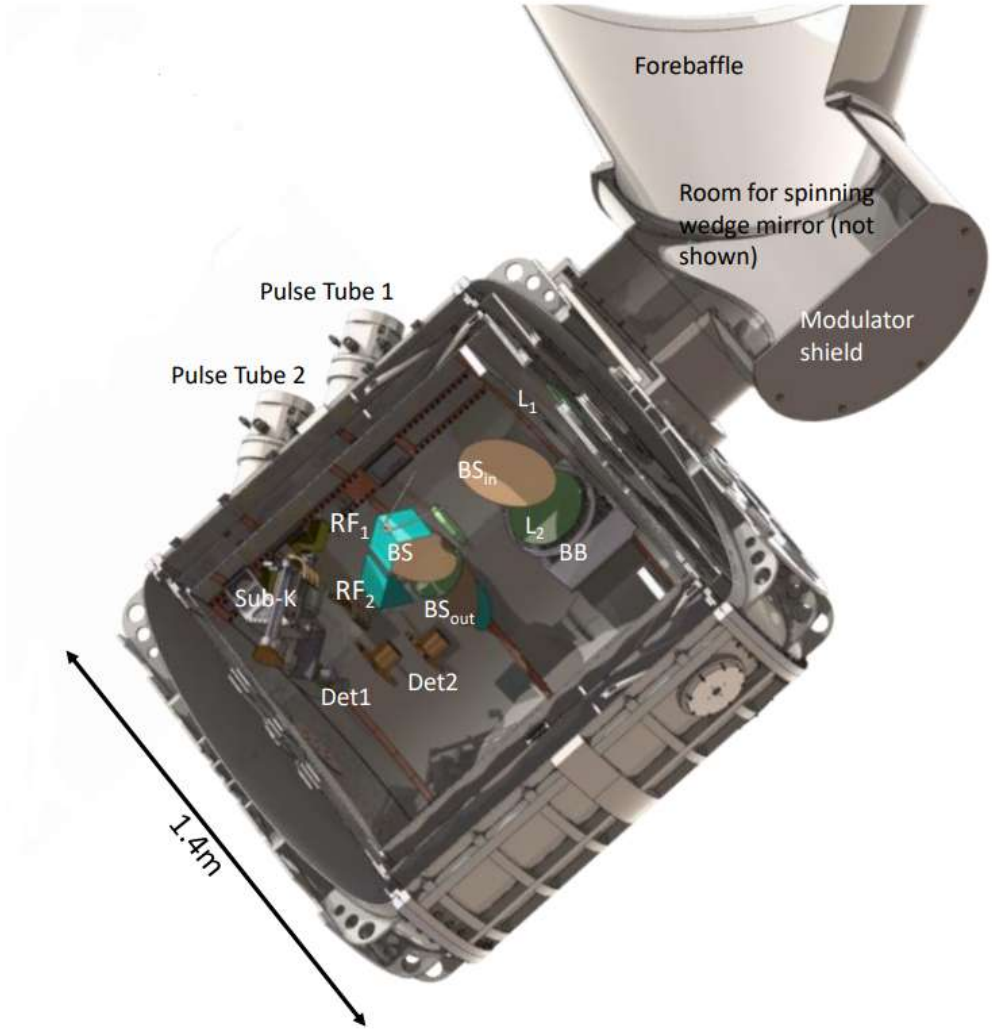

Figure 2.8: Rendering of the accommodation of the COSMO instrument inside its cryogenic system.

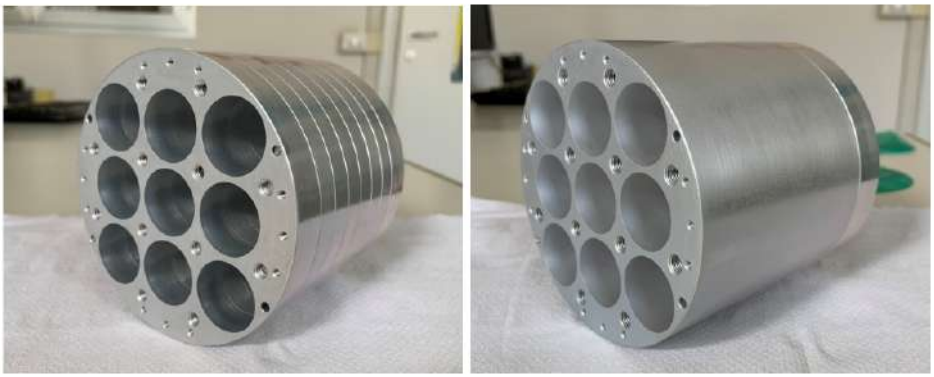

Figure 2.9: Low-frequency array on the left, high-frequency array on the right.

Figure 2.10: 3D rendering of the COSMO cryogenic system.

the accuracy of the instrument itself, leading to have an emissivity very close to 1 (within 100 ppb).

2.4 General description of the readout electronics

The main goal of the COSMO readout electronics is to achieve a sampling rate of approximately 60 kHz, and this value one of the motivation behind building and developing a readout electronics system using commercial devices. This high rate is necessary due to the geometry of the multimode KIDs, which have base-band frequencies between 80 and 130 MHz, and an expected time constant, $\tau \sim 60\ \mu$s. Indeed, the noise in detectors typically extends up to a maximum frequency, $f_{\max}$, which is related to the system's time constant, τ, and typically determined by the relationship $f_{\max} \simeq 3/\tau$, meaning the bandwidth of the noise is set by this characteristic time; therefore, the frequency range of significant noise is primarily governed by the system's dynamics. When considering how to handle this noise, one option is to sample the signal at $f_{\max}$, which ensures that all of the relevant noise is captured, and subsequently, data can be averaged or filtered digitally if the signal does not extend across this entire frequency range. On the other hand, subsampling (sampling below $f_{\max}$) introduces additional complexities; while it may seem like a good idea to reduce data size, it can lead to residual noise in the subsampled data.
The high sampling rate is required to accommodate the fast rotation of the

wedge-spinning mirror. The mirror is expected to spin at a minimum speed of 600 rpm (10 Hz). Multiplying this by the number of beams (60, corresponding to 1° per beam), we expect 600 samples per second. To satisfy the Nyquist criterion, the sampling rate must be at least three times higher: $600 \cdot 3 = 1.8$ kHz, which is the minimum required sampling rate. For the interferometer, with a length of 254 mm and 128 discrete roof mirror positions, the step size is 1.98 mm. The speed of the interferometer is calculated by dividing this step size by the time for one full rotation of the spinning mirror, 0.1 s, yielding a velocity of 19.8 mm/s. The total time to acquire an interferogram is therefore $254\,\text{mm}/19.8\,\text{mm/s} \approx 13\,\text{s}$. With this configuration, COSMO can effectively remove atmospheric fluctuations that occur on timescales slower than 13 seconds.

The architecture of the readout electronics developed, tested and described in this thesis is depicted in figure 2.11.
Following figure 2.11, the FPGA digitally generates the readout signal in the I-Q domain, which is converted to analog by the two DACs (one for I and one for Q signal) and split into the I+, I-, Q+, Q- components to feed the modulator. At this point, the signal is upconverted from the baseband to the RF band using a local oscillator, and it is eventually attenuated before entering the cryostat to excite the resonance frequencies of the KIDs. Before exiting from the cryostat, the signal is amplified by a low-noise amplifier (LNA), then it is downconverted to the baseband by the demodulator and converted from analog to digital before being acquired.
The FPGA, a Xilinx Kintex 7, is mounted in a PXI FPGA Module, NI PXIe-5782. This solution allows to implement COSMO firmware and software in a LabVIEW environment. The host computer used is a DELL Precision 3930 RackWorkstation, Core i9.
The architecture is based on commercial IQ transceiver, and by modulating the signal with a Local Oscillator (LO) it is possible achieve any frequency in the IQ mixer band.
Modulator and demodulator are, respectively, ADL 5386 [*] and ADL 5387 [†] by Analog Devices. The LO is a Valon 5009 [‡], used to achieve the desired working frequency band. Filters SLP-44+ [§] and SLP-250+ [¶] are used to effectively cut off unwanted harmonics generated by the LO and the modulator/demodulator. Moreover, they define the bandwidth of the readout electronics, allowing a total bandwidth of about 88 MHz (between -44 MHz and +44 MHz with respect to the LO).

[*] https://www.analog.com/en/products/adl5386.html
[†] https://www.analog.com/en/products/adl5387.html
[‡] https://www.valonrf.com/frequency-synthesizer-6ghz.html
[§] https://www.minicircuits.com/WebStore/dashboard.html?model=SLP-44
[¶] https://www.minicircuits.com/WebStore/dashboard.html?model=SLP-250

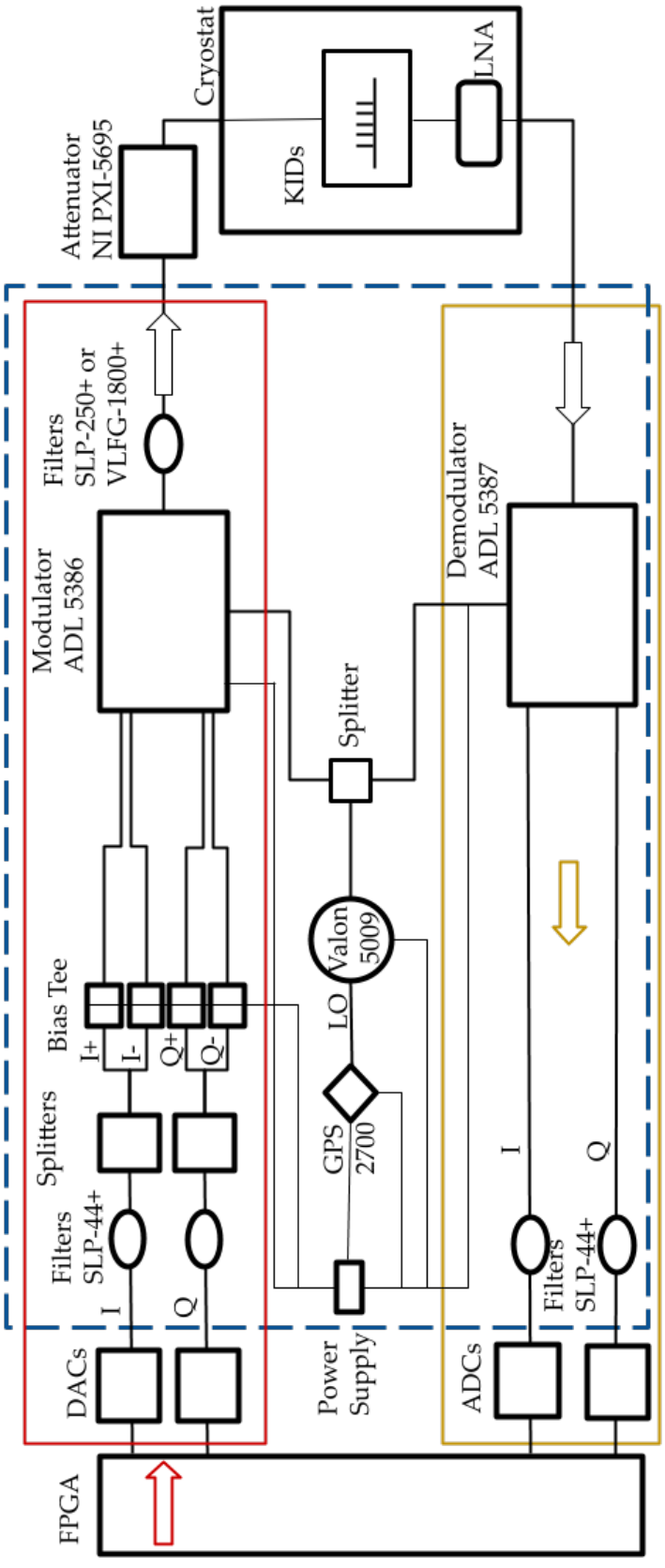

Figure 2.11: Readout electronics block diagram. The signal path follows the arrow. The blue box represents the modular elements of the readout electronics, a picture of them is in figure 5.1. The red and yellow boxes represent, respectively, the signal-in and the signal-out parts of the readout electronics.

The attenuator is a NI PXI-5695 [*], with a fixed stage of attenuation at 28 dB (with frequency dependence) and a variable attenuation stage ranging between (with frequency dependence) 11 and 44 dB. The two stages of attenuation can also be used in series.
All these components are detailed and discussed in chapter 5.
As shown in figure 2.11, the signal is attenuated to a power level that does not alters the superconducting state of the detectors. After attenuation, the signal enters the cryostat, where the KIDs and a Low Noise Amplifier (LNA) are located. The LNA amplifies the signal to ensure a sufficient signal-to-noise ratio before acquisition.
Regarding the KIDs, the majority of the test described in this thesis are done using the Niobium KIDs present in the Milano-Bicocca laboratory, cooled down in a 4 K cryostat, a DK-408D2 Gifford-McMahon (section 6.2). Their resonant frequencies are between 1.89 and 2.05 GHz at approximately 5 K. The Gifford-McMahon has temperature oscillations of about 25 mK on a timescale of 1 Hz.
An array of Aluminum KIDs cooled down in a dilution fridge is also used during the test campaign performed at Sapienza University in Rome (section 6.3). Their working bandwidth is centered at 310 MHz.

[*] https://www.ni.com/docs/en-US/bundle/pxi-5695-specs/page/specs.html

Chapter 3

Kinetic Inductance Detectors

In this chapter I will introduce the Kin+tic Inductance Detectors (KIDs).
KIDs are highly sensitive superconducting devices used for detecting electromagnetic radiation across a broad range of wavelengths, from millimeter to optical. They operate at temperatures below their superconducting critical temperature, which depends on the material. For aluminum, this critical temperature is approximately 1.2 K, requiring sub-kelvin temperatures achieved using cryogenic systems. They exploit the kinetic inductance effect, which arises from the inertia of the Cooper pairs in a superconducting material. When incoming photons hit the superconductor with enough energy to break Cooper pairs, quasiparticles are generated. This process changes the inductance and, consequently, the resonance frequency of a superconducting resonator circuit. The resulting frequency shift is measured.
To achieve the desired spectral resolution in CMB experiments, KIDs are often combined with techniques such as Fourier Transform Spectroscopy (FTS). This combination enables the separation and precise measurement of different frequency components of incoming radiation.
One of the key advantages of KIDs is their multiplexing capability: each detector is a superconducting resonator with a unique resonant frequency, spaced within a wide RF band, enabling the simultaneous readout of multiple detectors to minimize the heat load.
Furthermore, KIDs operate at cryogenic temperatures, where superconductivity is maintained. This requirement necessitates sophisticated cryogenic systems for cooling, but it also ensures minimal thermal noise and high detection efficiency.

3.1 Superconductivity

The phenomenon of superconductivity was observed for the first time in 1911 by Heike Kameringh Onnes and his colleagues, who experimentally discovered that mercury has *practically zero* resistance when cooled down to approximately 3 K [45].

A superconductor is a material that exhibits zero resistance R to DC electrical current when cooled below its critical temperature T_c, which is specific of the material. This disappearance of R is accompanied by the expulsion of magnetic field (B-field) lines from the material, increasing the magnetic flux at the surface - a phenomenon known as the Meissner effect.
When R drops to zero below T_c, according to Ohm's Law, an infinite DC current could be generated by applying a finite voltage. However, superconductors have non-zero impedance, as their reactance (both capacitive and inductive) does not vanish with R. The non-zero inductance of the superconductor prevents the instantaneous formation of an infinite current. Beyond a maximum current, the critical current I_c, the superconductor reverts to its normal state. Similarly, the superconductivity can be destroyed by applying an external B-field whose strength exceeds the material's critical field B_c.
According to Bardeen-Cooper-Schrieffer (BCS) theory [46], when a superconductor is cooled below T_c a supercurrent is created. Supercurrent consists of paired normal charge carriers (electrons) which are called Cooper pairs (CPs), while the remaining charge carriers not in pairs are called quasiparticles (QP). QP have the same spin and charge of electrons, but their effective mass $m*$ differs from the rest mass of an electron, m_e. On the other side, CP can be modeled as quasi-bosons, with mass $2m_e$ and charge $2e$, and they are bound together by the electron-phonon interaction, with binding energy at absolute-zero:

$$\Delta_0 = \frac{3.52}{2} k_B T_c \tag{3.1}$$

where k_B is the Boltzmann's constant. Typically Δ_0 is $\mathcal{O}(10^{-3})$eV, around three orders of magnitude smaller than the one of semiconductors.
Thus the absorbed radiation with energy greater than $2\Delta_0$ can break CPs into QPs allowing us to estimate the total power absorbed in the device, P_{abs}.
Let's now re-derive equation 3.1 underling the dependence on T_c and the absorbed optical power, P_{abs}. The absorbed optical power P_{abs} is the portion of the total optical power incident on a detector that is effectively absorbed by the system. It is given by:

$$P_{abs} = \epsilon_{opt} \eta_{det} P_{opt} \tag{3.2}$$

where ϵ_{opt} is the optical efficiency, which accounts for losses due to the optics; η_{det} is the quantum efficiency of the detector, which represents the fraction of photons absorbed by the detector and converted into an electrical signal; and P_{opt} is the total incident optical power.

3.1.1 Quasiparticle Generation and Recombination

The generation (and recombination) of QPs are due to the absorption (and emission) of thermally generated phonons in the material. This can be produced by temperature fluctuations, or absorption of incoming photons with energy $h\nu \geq 2\,\Delta_0$.

An empirical expression for the QP lifetime, τ_{QP}, by [47] is:

$$\tau_{\mathrm{QP}} = \frac{\tau_{\max}}{1 + n_{\mathrm{QP}}(T)/n^*} \tag{3.3}$$

where τ_{max} is the experimentally observed maximum lifetime, $n_{\mathrm{QP}}(T)$ is the number density of thermally generated QP, and n^* is the crossover density, which is observed to be roughly constant at temperatures $T_c/10 \lesssim T \lesssim T_c/2$ and for a wide range of materials, $n^* \sim 100 \mu\mathrm{m}^{-3}$.
To separate the contribution given by thermal phonon absorption (variation of T_{base}) and pair-breaking photons (P_{abs}), the total number density of QPs can be written as the sum over these two contributes:

$$n_{\mathrm{QP,tot}} = n_{\mathrm{QP}}(T) + n_{\mathrm{QP}}(P) \tag{3.4}$$

For temperature $T \ll T_c$, the number density of thermal QP, $n_{\mathrm{QP}}(T)$, is:

$$n_{\mathrm{QP}}(T) \simeq 2N_0\sqrt{2\pi k_{\mathrm{B}} T \Delta_0} e^{-\Delta_0/k_{\mathrm{B}}T} = \frac{N_{\mathrm{QP}}(T)}{\Sigma} \tag{3.5}$$

with N_0 the density of states at the Fermi level, $N_{\mathrm{QP}}(T)$ the total number of thermally generated QP, and Σ the volume of the inductor, as a KID can be seen as a component of an electric circuit, as will be explained in section 3.4.2 .
The total number of optically generated QP (for incoming photon at frequency ν):

$$N_{\mathrm{QP}}(P) = \frac{\epsilon_{\mathrm{opt}} N_{QP}(\nu) P_{\mathrm{abs}} \tau_{QP}}{h\nu} = \frac{N_{QP}(\nu) P_{\mathrm{opt}} \tau_{QP}}{h\nu} \tag{3.6}$$

where $N_{QP}(\nu) = \dfrac{\eta_{\mathrm{det}} h\nu}{\Delta_0}$ is the number of QP produced per absorbed photons of frequency ν; η_{det} is the detector quantum efficiency (typically $\sim 80\%$).
Putting together equation 3.5 and equation 3.6, it is possible to get $N_{\mathrm{QP,tot}}$ and rederive the expression of the energy gap as function of power and temperature:

$$\Delta(T,P) = \frac{\Delta_0}{2}\left(1 + \sqrt{1 - \frac{2N_{\mathrm{QP,tot}}}{\Sigma N_0 \Delta_0}}\right) \tag{3.7}$$

3.2 The Two-Fluid Model

Since several KID parameters that will be discussed above depend on the conductivity σ of the superconductor, let us introduce this parameter following the two-fluid model of superconductivity by Mattis and Bardeen [48]. According to this theory, it is possible to relate the Drude conductivity σ_{d} in a normal conductor to the CPs and QP of a superconductor.
In a conductor, the equation of motion for a charge carrier is:

$$m^* \dot{v} = -eE - \frac{m^* v}{\tau_{\mathrm{s}}} \tag{3.8}$$

where m^* is the effective mass of the charge carrier, v is the drift velocity (which is $\propto e^{j\omega\tau_s}$, with ω the frequency of a time-varying electromotive force), and the second term on the right-hand side of the equation is a damping term related to the scattering of charges off of the material, with τ_s the characteristic time of collision.
Recalling some relations given by the Ohm's Law for the Drude conductivity $J = \sigma_d E$, and for the current density $J = n_e e v$, and putting them in equation 3.8 and solving in function of the Drude conductivity:

$$\begin{aligned}\sigma_d(\omega) &= \frac{n_e e^2 \tau_s}{m_e} \frac{1}{1 + j\omega\tau} = \frac{\sigma_n}{1 + j\omega\tau_s} = \\ &= \frac{\sigma_n}{1 + \omega^2 \tau_{s^2}} - j \frac{\sigma_n \omega \tau_s}{1 + j\omega^2 \tau_s^2} = \sigma_1 - j\sigma_2\end{aligned} \tag{3.9}$$

where σ_n is the normal conductivity, $\sigma_n = n_e e^2 \tau_s / m^*$. Note that in a normal conductor $\sigma_d \approx \sigma_n$ at frequencies ω below the optical range ($\omega\tau_s \ll 1$), since τ_s is short, on the order of $10^{-14} s$.
Thus the Drude conductivity can be split into real (σ_1) and imaginary (σ_2) parts, which represents the dissipative response (i.e., actual conduction), and the inductive or reactive response (i.e., energy storage in the material), respectively.

3.3 Kinetic Inductance

The inductance L is defined as the ratio of the applied voltage over the rate of change of the current: $L = \frac{V}{d\mathrm{I}/d\mathrm{t}}$.
Indeed, when a voltage is applied to a circuit, current does not start to flow instantaneously but firstly some energy from the applied voltage has to be stored in a B-field, via the inductance. The energy stored in the inductance is $E_L = \frac{1}{2} L I^2$.
The total inductance is the sum of the magnetic (or geometric) and kinetic inductances:

$$L_{tot} = L_g + L_k \tag{3.10}$$

From the energy point of view, the kinetic inductance L_k accounts for the energy stored in the supercurrent as the kinetic energy of the Coopers pairs. Thus the kinetic inductance arises from the inertia of the CPs: charge carriers scatter (or break apart, in the case of CPs), thus the kinetic energy (velocity) of the remaining charge carriers increases in order to keep the current constant. However, this increase in velocity cannot happen instantaneously.
The magnetic (geometric) inductance L_m depends on the geometry of the superconducting film, such as length, width, and thickness.
It is possible to define the kinetic inductance fraction:

$$\alpha = \frac{L_k}{L_{tot}} \tag{3.11}$$

By equating the energy in the kinetic inductance with the kinetic energy of CP, it is possible to get an expression of the kinetic inductance:

$$\frac{1}{2}L_{\mathrm{k}}I^2 = \frac{1}{2}2m_{\mathrm{e}}v_{\mathrm{CP}}^2 N_{\mathrm{CP}} \tag{3.12}$$

where v_{CP} is the CP velocity and N_{CP} is the total number of CPs.

3.4 Lumped-element KID

Let us now present circuit model for a lumped-element KID (LEKID), the kind of detectors that are used in the COSMO experiment.
By creating a RLC resonant circuit from superconducting components, the variation of the quasiparticle density in the superconductor alters the kinetic inductance, L_{k}. As a consequence, the resonant frequency ω_0, defined as

$$\omega_0 = \frac{1}{\sqrt{L_{\mathrm{tot}}C_{\mathrm{r}}}} \tag{3.13}$$

(with C_{r} is the coupling capacitance, $C_{\mathrm{r}} = \dfrac{1}{L_{\mathrm{tot}}\omega_0^2}$) is altered.
The variation of the resonant frequency can be sensed by the readout electronics. Hence this circuit can be used as a photon-detector.
Moreover, by varying the physical and geometrical characteristics of the apparatus it is possible to fabricate many resonant elements with different resonant frequencies in order to place several LEKIDs on a single transmission line, achieving a very high multiplexing factor which leads a significant reduction of the heat load on the cryogenic system.

3.4.1 Photon detection

When a photon with energy E larger than the energy gap of the superconductor, 2Δ, is absorbed, the quasiparticles are brought out of thermal equilibrium, leading to a variation in the number of QPs (and CPs). The change in the number of QPs alters the superconductivity of the metal, and this change can be detected by incorporating the superconductor into a resonant circuit. Thus, the detection of photons can be achieved by observing the change in the resonance parameters.

An important parameter is Q, the quality factor of the resonant circuit. It expresses how much a resonant system is capable of storing energy without dissipation:

$$Q = 2\pi\frac{\text{energy stored}}{\text{energy dissipated per cycle}} = 2\pi f_0\frac{\text{energy stored}}{\text{dissipating power}} \tag{3.14}$$

Remembering that $\omega_0 = 2\pi f_0$ is the resonant angular frequency, and τ is the time constant for which, when a resonant circuit is excited, it oscillates, dissipating energy exponentially, the quality factor can rewritten as:

$$Q = \omega_0 \tau \tag{3.15}$$

and calling Δf the bandwidth of the resonator, it can be shown that:

$$Q = \omega_0 \tau = \frac{f_0}{\Delta f} \tag{3.16}$$

3.4.2 LEKID parameters

Let us start with a schematic of a LEKID in figure 3.1 and a list of the parameters:

- Z_0: feedline impedance
- C_c: coupling capacitance
- C_r: resonator capacitance
- L_{tot}: total resonator inductance
- R_{eff}: effective resistance, in series with L_{tot}
- Z_{eff}: effective impedance coupled to a feedline with characteristic impedance Z_0
- ϵ_a: the asymmetry parameter which accounts for a frequency dependent asymmetry in the resonator impedance

Starting from the LEKID equation of resonant frequency, equation 3.13, the derivative with respect to L_k is:

$$\frac{d f_0}{d L_k} = -\frac{\alpha f_0}{2 L_k} \tag{3.17}$$

The asymmetry parameter ϵ_a, is defined as [49]:

$$\epsilon_a = \frac{C_r}{C_c Q_i} \tag{3.18}$$

with C_c the coupling capacitance, and Q_i the internal quality factor.
Being Z_r the total resonator impedance:

$$Z_r = j\omega_0 L - \frac{j}{\omega_0 C} + R \tag{3.19}$$

Q_i is defined as:

$$Q_i = \frac{\Im(Z_r)}{\Re(Z_r)} = \frac{\omega_c L_{tot}}{R_{eff}} = \frac{\omega_c E_r}{P_{diss}} \tag{3.20}$$

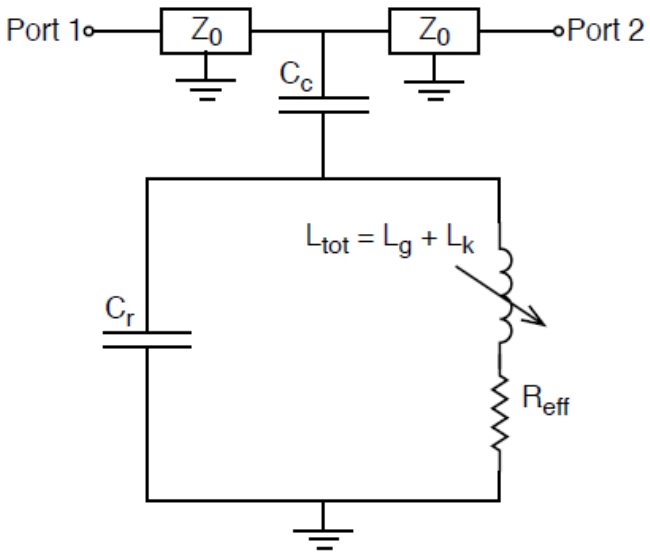

Figure 3.1: Schematic of a LEKID

with E_r the stored (internal) energy of the resonator, P_{diss} the dissipated power. The coupling quality factor Q_c is defined as:

$$Q_c = \frac{2(C_r + C_c)}{\omega_0 C_c^2 Z_0} \tag{3.21}$$

An additional term is given by the external loss factor, Q_{loss}, which is typically of the order of $\sim 10^6$ and it accounts for various parasitic effects that can degrade the overall quality of the resonator.
Thus, the measured resonator quality factor, Q_r is:

$$\frac{1}{Q_r} = \frac{1}{Q_i} + \frac{1}{Q_c} + \frac{1}{Q_{loss}} \tag{3.22}$$

To obtain an expression for the transmission response, S_{21}, as a function of frequency for a capacitively coupled resonator let's start by defining the scattering matrix S.
The scattering matrix is very useful for describing microwave circuits in terms of the reflected and transmitted waves as a function of the incident one. For a two-port network, the S-matrix is a 2×2 matrix:

$$\begin{pmatrix} V_1^- \\ V_2^- \end{pmatrix} = \begin{pmatrix} S_{11} & S_{12} \\ S_{21} & S_{22} \end{pmatrix} \begin{pmatrix} V_1^+ \\ V_2^+ \end{pmatrix} \tag{3.23}$$

where applies the convention that V_n^+ is the incident signal at the n-th port, and V_n^- is the reflected signal at the n-th port.
Therefore S_{21} is the signal injected into port 1 and outgoing from port 2.
Following [50], the scattering parameter S_{21} for a LEKID, which can be seen as

RLC circuit in series with Z_0 (feedline impedance) and Z_{eff} (effective impedance) is:

$$S_{21} = \frac{1}{1+2\frac{Z_0}{Z_{\text{eff}}}} = \frac{1}{1+\frac{\omega^2 M^2}{2Z_{\text{eff}}Z_0}} \tag{3.24}$$

where the effective impedance of the coupled resonator is:

$$Z_{\text{eff}} = \frac{\omega^2 M^2}{Z_{\text{res}}} \tag{3.25}$$

with M the mutual inductance between the the feedline and the resonator.
The expression of the S_{21} coefficient of the carrier tone expressed as function of the frequency, base temperature, optical power, and thus quality factor, can be written as follows when near the resonance (first-order approximation with respect to $\delta x = \frac{\omega-\omega_0}{\omega_0}$):

$$S_{21}(\omega, T, P) = 1 - \frac{1}{1+2Z_{\text{r}}/Z_0} = 1 - \frac{1+j\epsilon_{\text{a}}}{1+j\epsilon_a\frac{Q_{\text{r}}}{Q_{\text{c}}}}\frac{Q_{\text{r}}}{Q_{\text{c}}}\left[\frac{1}{1+\frac{2jQ_{\text{r}}\delta x}{1+j\epsilon_{\text{a}}Q_{\text{r}}/Q_{\text{c}}}}\right] \tag{3.26}$$

where Z_{r} near the resonant frequency is:

$$Z_{\text{r}}(\omega) \simeq Z_0\left[\frac{Q_{\text{c}}}{2Q_{\text{i}}} + jQ_{\text{c}}\delta x\right]\frac{1}{1+j\epsilon_{\text{a}}} \tag{3.27}$$

With the assumption that $\epsilon_{\text{a}} \ll 1$, equation 3.26 becomes:

$$S_{21}(\omega, T, P) = 1 - \frac{Q_{\text{r}}}{Q_{\text{c}}}\frac{1}{1+2jQ_{\text{r}}\delta x} \tag{3.28}$$

This equation represents a circle in the complex plane defined by $I = \Re(S_{21})$ and $Q = \Im(S_{21})$ centered in $\left(\frac{1}{2} + \frac{Q_{\text{r}}}{2Q_{\text{i}}}, 0\right)$. A simulation of the IQ plane is in figure 3.2.
In figure 3.3 is plotted the magnitude as function of the resonant frequency, while in figure 3.4 there is the phase.
Far from the resonance frequency, $S_{21} \simeq 1$, which means that the signal is transmitted without being modified. Thus there is no phase or amplitude variation since the KID does not attenuate frequencies far from its resonance.
The depth of the S_{21} trace (in dB) is :

$$D = 20\log_{10}\left(1 - \frac{Q_{\text{r}}}{Q_{\text{c}}}\right) \tag{3.29}$$

A KID is read out by selecting a test tone at the resonating frequency ω corresponding to a base temperature. As illustrated in previous equations (and in figure 3.2), the IQ circle varies with temperature. It is possible to follow the resonant frequency as a function of temperature variation, resulting in an arc trajectory in the IQ plane.
This is indeed the quantity we are able to track with our Niobium KIDs, as introduced in section 2.4, and better described later in chapter 6.

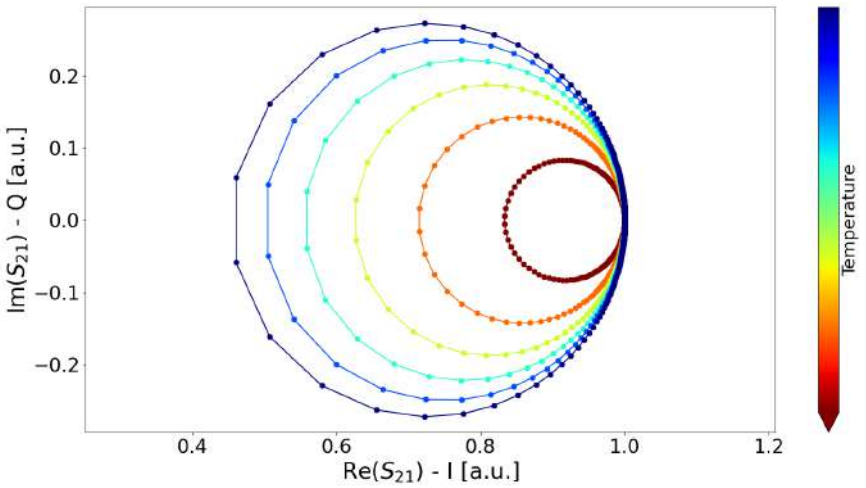

Figure 3.2: Simulated IQ plot according as equation 3.28, where I is the real part of S_{21}, and Q the imaginary one. The temperature varies by changing Q_i. Smaller temperatures in blue, higher in red.

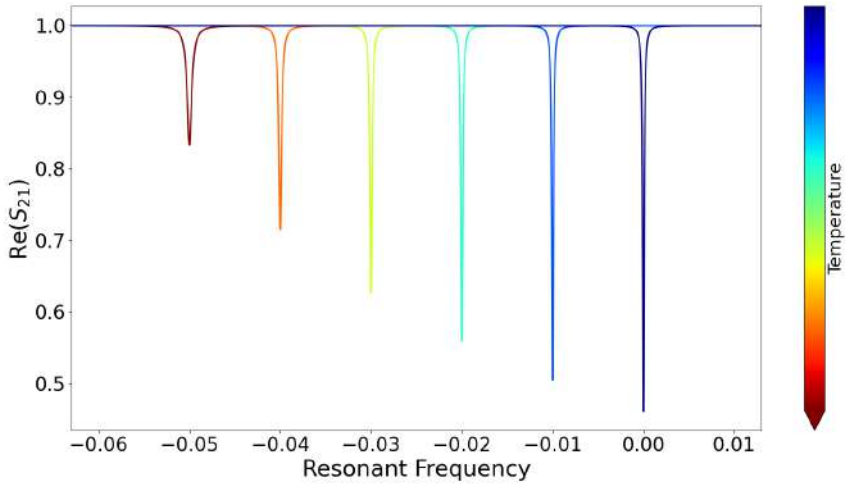

Figure 3.3: Simulated arg(S_{21}) plot as function of the resonant frequency shift, according as equation 3.28. The temperature varies by changing Q_i. Smaller temperatures in blue, higher in red.

3.4.2.1 Amplitude and phase of a resonator

As said before, when photons with energy E greater the CPs binding energy 2Δ hit the superconductor, CPs are broken into QPs with an efficiency η:

$$\delta N_{QP} = \eta \frac{E}{\Delta} \tag{3.30}$$

The consequences of this mechanism are:

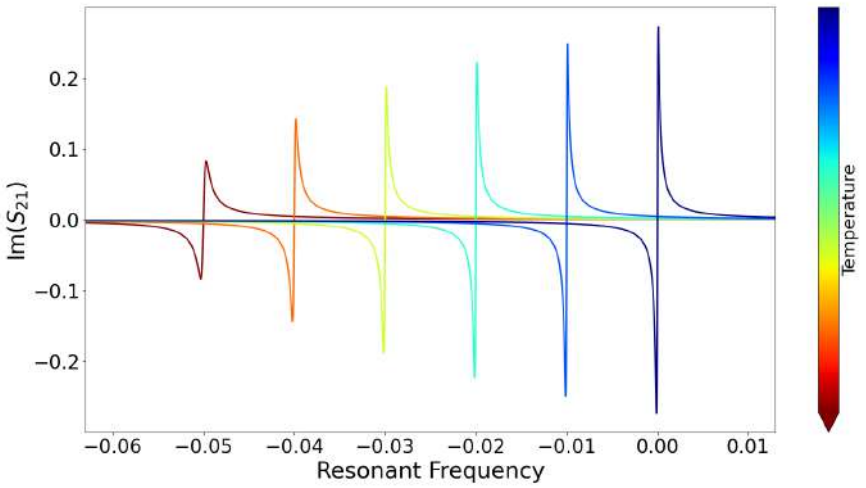

Figure 3.4: Simulated phase(S_{21}) plot as function of the resonant frequency shift, according as equation 3.28. The temperature varies by changing Q_i. Smaller temperatures in blue, higher in red.

- the decrease of the number of CPs leading to an increase of the kinetic inductance
- the increase of the number of QPs leading to an increase of the surface resistance and thus a decrease of the quality factor Q_i

After an energy release event, QPs can diffuse proportionally to the diffusion constant of the material, D_c, for a distance $l \sim D_c \tau_{QP}$. τ_{QP} is the QP lifetime or the recombination time, it is a characteristic of the material, it depends on the temperature and it is an exponential law expressing that after some time two QPs eventually meet and they recombine emitting a phonon.
Amplitude and frequency of each resonance vary by exciting the detector with a tone associated to the resonant frequency. Starting from the equation of S_{21}(eq. 3.28), it is possible to estimate the frequency and amplitude variation:

$$\delta f = \frac{f_0}{2Q_c} \delta \left[\mathrm{Im}\left(\frac{1}{1-S_{21}} \right) \right] \tag{3.31}$$

$$\delta A = \frac{1}{Q_c} \delta \left[\mathrm{Re}\left(\frac{1}{1-S_{21}} \right) \right] \tag{3.32}$$

3.4.2.2 Quasi-particle lifetime

The QP lifetime τ_{QP} is the average time in which a QP finds another QP and they recombine into a CP. It is a parameter that affects the sensitivy of the detector, since the longer the QPs live the more accurate is the determination of their

population. The theoretical lifetime as a function of temperature as given by Kaplan [51]:

$$\tau_{\mathrm{QP}}^{-1} = \frac{\sqrt{\pi}}{\tau_0}\left(\frac{2\Delta}{K_{\mathrm{B}}T_{\mathrm{c}}}\right)^{5/2}\left(\frac{T}{T_{\mathrm{c}}}\right)^{1/2} e^{-\Delta/(k_{\mathrm{B}}T_{\mathrm{c}})} = \frac{n_{\mathrm{QP}}}{\tau_0}\frac{4\Delta^2}{2N_0(K_{\mathrm{B}}T_{\mathrm{c}})^3} \tag{3.33}$$

where τ_0 is the parameter that accounts for the electron-phonon coupling strength in the material.

3.4.2.3 Temperature Responsivity

Temperature responsivity is the change in the LEKID's resonant frequency f_0 in response to a change in base temperature. The expression is:

$$R_{\mathrm{T}} = \frac{df_0}{dT} = \frac{df_0}{d\sigma_2}\frac{d\sigma_2}{dn_{\mathrm{QP}}}\frac{dn_{\mathrm{QP}}}{dT} \tag{3.34}$$

with (the analytical solution is in [49]):

- $$\frac{df_0}{d\sigma_2} = \alpha\frac{f_0}{2\sigma_2} \tag{3.35}$$
- for $T_{\mathrm{base}} \ll T_{\mathrm{c}}$:
$$\frac{dn_{\mathrm{QP}}}{dT} \simeq \frac{n_{\mathrm{QP}}}{T}\left(\frac{1}{2} + \frac{\Delta_0}{k_{\mathrm{B}}T}\right) \tag{3.36}$$

3.4.2.4 Optical Responsivity

Optical responsivity is the change in the LEKID's resonant frequency in response to a change in absorbed optical power at a fixed temperature:

$$R_{\mathrm{P}} = \frac{df_0}{dP_{\mathrm{abs}}} = \frac{df_0}{d\sigma_2}\frac{d\sigma_2}{dn_{\mathrm{QP}}}\frac{dn_{\mathrm{QP}}}{dP_{\mathrm{abs}}} \tag{3.37}$$

with:

- $$\frac{df_0}{d\sigma_2}\frac{d\sigma_2}{dn_{\mathrm{QP}}} \simeq -\frac{\alpha f_0}{4N_0\Delta_0}\left(1 + \sqrt{\frac{2\Delta_0}{\pi k_{\mathrm{B}}T}}\right) \tag{3.38}$$
- $\frac{dn_{\mathrm{QP}}}{dP_{\mathrm{abs}}}$ depends on the dominant phenomena of absorption, as reported by [49].
  Let us start writing the rate of change in the total number density of QP:
$$\frac{dn_{\mathrm{QP}}}{dt} = \Gamma_{\mathrm{opt}} + \Gamma_{\mathrm{ro}} + \Gamma_{\mathrm{therm}} + \Gamma_{\mathrm{rec}} = \tag{3.39}$$
$$= \frac{\eta_{\mathrm{det}}P_{\mathrm{abs}}}{\Delta\Sigma} + \frac{\epsilon_{\mathrm{ro}}P_{\mathrm{ro}}}{\Delta\Sigma} + \gamma N_0^2 8\pi k_{\mathrm{B}}T\Delta e^{-2\Delta/k_{\mathrm{B}}T} - \frac{n_{\mathrm{QP}}}{\tau_{\mathrm{QP}}} \tag{3.40}$$

with: Γ_{opt} the QP generation rate due to absorbed optical power; Γ_{ro} the QP generation rate due to microwave readout power; Γ_{therm} the QP generation rate due to thermal phonons; Γ_{rec} the QP recombination rate into CPs; η_{det} the efficiency of QP generation from absorbed optical power; ϵ_{ro} the internal QP generation efficiency for absorbed readout power; $\gamma = 1/(n_{opt}\tau_{opt})$ a constant relating the number density of QP to the QP recombination time.

- case a: QP generation is dominated by the absorption of photons. This behavior has been observed in Al KIDs (e.g. [52] and [53]), where the absorption of optical photons leads to the creation of QPs. Equation 3.40 becomes:

$$\frac{d n_{QP}}{d t} \simeq \frac{\eta_{det} P_{abs}}{\Delta\Sigma} + \gamma n_{QP}^2 \tag{3.41}$$

  and it can be shown that $\frac{d n_{QP}}{d P_{abs}}$ is:

$$\frac{d n_{QP}}{d P_{abs}} = \frac{1}{2}\sqrt{\frac{\eta}{\gamma P_{abs}\Delta\Sigma}} = \frac{n_0}{2P_{abs}}\frac{1}{1 + j\omega\tau_{QP}/2} \tag{3.42}$$

  This indicates that the responsivity decreases with the square root of the absorbed power, demonstrating high sensitivity to optical signals.

- case b: QP generation is dominated by thermal phonon generation, or the recombination time that does not depend on P_{abs}.
  Equation 3.40 becomes:

$$\frac{d n_{QP}}{d t} \simeq \frac{\eta_{det} P_{abs}}{\Delta\Sigma} + \Gamma_{therm} - \frac{n_{QP}}{\tau_{eff}} \tag{3.43}$$

  In this case, the rate of QP generation is influenced not only by the absorbed optical power but also by the thermal environment of the detector.
  It can be shown that $\frac{d n_{QP}}{d P_{abs}}$ is:

$$\frac{d n_{QP}}{d P_{abs}} = \frac{\eta\tau_{eff}}{\Delta\Sigma}\frac{1}{1 + j\omega\tau_{eff}} \tag{3.44}$$

  This indicates that the QP density is not solely reliant on the optical power but also on the thermal noise in the system. As a result, the KID may exhibit limited sensitivity to variations in optical power when thermal effects dominate.
  This behavior has been observed in TiN KIDs (e.g. [54] and [55]).

- case c: intermediate case. An effective "dark" power loading on the device is visible, P_{dark}, which generates a constant background of QP

whose rate of creation is independent of absorbed optical power. Equation 3.40 becomes:

$$\frac{d\,n_{\mathrm{QP}}}{d\,t} = \frac{\epsilon_{\mathrm{ro}} P_{\mathrm{ro}}}{\Delta\Sigma} + \gamma N_0^2 8\pi k_{\mathrm{B}} T \Delta e^{-2\Delta/k_{\mathrm{B}}T} - \gamma n_{\mathrm{QP}^2} \tag{3.45}$$

and $\frac{d\,n_{\mathrm{QP}}}{d\,P_{\mathrm{abs}}}$ is:

$$\frac{d\,n_{\mathrm{QP}}}{d\,P_{\mathrm{abs}}} = \sqrt{\frac{\eta_{\mathrm{det}}}{\Delta\Sigma\gamma}} \frac{1}{\sqrt{P_{\mathrm{dark}} + P_{\mathrm{abs}}}} \tag{3.46}$$

This indicates that the responsivity of the detector is influenced by both the dark power and the absorbed optical power, leading to a more complex response. As the absorbed power increases, the contribution of the dark power becomes less significant, allowing for improved sensitivity.

3.5 Sensitivity

Noise equivalent power (NEP) is the standard expression for sensitivity, typically measured in $\mathrm{W}/\sqrt{\mathrm{Hz}}$. It denotes the noise power within a measurement bandwidth of 1 Hz. Equivalently, according to the Shannon-Nyquist sampling theorem, it represents the noise power measured after integration of 0.5 seconds.
NEP is the sum of various noise contributions, including photon noise, amplifier noise (usually dominated by the first amplification stage provided by cryogenic low noise amplifiers (LNAs)), detector noise (also known as generation-recombination noise), two level system (TLS) noise, and readout noise:

$$\mathrm{NEP}_{\mathrm{tot}} = \sqrt{\mathrm{NEP}^2_{\mathrm{phot}} + \mathrm{NEP}^2_{\mathrm{ampl}} + \mathrm{NEP}^2_{\mathrm{G\text{-}R}} + \mathrm{NEP}^2_{\mathrm{TLS}} + \mathrm{NEP}^2_{\mathrm{readout}}} \tag{3.47}$$

Before analyzing these various types of noise in detail, one consideration is necessary.
KIDs are photon noise limited detectors (under the conditions of being in a high optical load environments, with low internal noise and optimized readout electronics), and photon noise follows Poisson, or shot noise statistics. This means that in a measurement dominated by shot noise, the Signal-to-Noise Ratio (SNR) increases as the square root of the mean number of detected events, $\sqrt{N}$.
In a sub-mm observation, the detector noise is limited by the shot noise of the background of in-band photons emanating from the receiver, optical system, atmosphere and astronomical source.
Let's have have a look at all the noise contributions.

3.5.1 Power Spectral Density

Before starting this section on noise, let us introduce the concept of
Power Spectral Density (PSD) is a measure used in signal processing to describe the power distribution of a signal across different frequencies, typically expressed in units of power per Hertz (e.g., W/Hz or dB/Hz). Mathematically, it is defined as the Fourier transform of the autocorrelation function of a signal. For a continuous signal $x(t)$ the PSD $S_x(f)$ can be expressed as:

$$S_x(f) = \lim_{T\to\infty} \frac{1}{T} \int_{-T/2}^{T/2} x(t)x^*(t+\tau)\,d\tau \tag{3.48}$$

where x^* denotes the complex conjugate of x, and T is the observation time.
In practice, the PSD provides insight into how the power of a signal is distributed over frequency, revealing which frequencies contain the most energy.
In particular, when dealing with KIDs, phase noise becomes a critical factor in determining the overall performance and sensitivity of the readout system, since the phase variation of the KIDs is directly proportional to the variation of absorbed energy.
Phase PSD refers to the phase information of the signal's frequency components. While the traditional PSD quantifies power, the phase PSD provides the phase relationship between different frequency components. This can be essential for understanding the signal's behavior, particularly in systems where phase relationships affect performance, as in the case of this thesis' readout electronics.

3.5.2 Generation-Recombination Noise

Generation-Recombination (GR) noise arises from the instantaneous uncertainty in the rate of QPs recombining into CPs, or equivalently, the rate at which CPs are broken into QP pairs. Assuming a steady state (the recombination/generation rates are equivalent: $\Gamma_{\text{gen}} = \Gamma_{\text{rec}}$), the uncertainty in the number of CPs is:

$$\delta N_{\text{CP}} = \sqrt{\left(\Gamma_{\text{rec}} + \Gamma_{\text{gen}}\right)\delta t} = \sqrt{2\Gamma_{\text{rec}}\delta t} \tag{3.49}$$

where δt is the measurement integration time with measurement bandwidth δf ($\delta t = 1/(2\delta f)$).
The recombination rate is:

$$\Gamma_{\text{rec}} = \frac{N_{\text{QP}}}{2\tau_{\text{QP}}} \tag{3.50}$$

Thus equation 3.49 becomes:

$$\delta N_{\text{CP}} = \sqrt{\frac{N_{\text{QP}}}{2\tau_{\text{QP}}\delta f}} \tag{3.51}$$

Dividing this equation by the square-root of the measurement bandwidth, and multiplying by the frequency responsivity to fluctuations in the number of QP, it is possible to get the frequency noise PSD (expressed in Hz/$\sqrt{\text{Hz}}$):

$$PSD_{\text{f, GR}} = \sqrt{\frac{N_{\text{QP}}}{2\tau_{\text{QP}}}} \frac{df_0}{dN_{\text{QP}}} \tag{3.52}$$

and NEP for generation-recombination is:

$$NEP_{\text{GR}} = \frac{PSD_{\text{f, GR}}}{\frac{df_0}{dN_{\text{QP}}} \frac{dN_{\text{QP}}}{dP_{\text{opt}}}} \tag{3.53}$$

GR noise is proportional to the number of QPs, which depends on the temperature of the KID, on its critical temperature, and on the power of the signal. The quasiparticle life time τ_{QP}, is typically 10-100 μs in the case of Al KIDs. This implies that there is no MKID response above this frequency, and the GR noise behaves as white noise below the frequency of $1/(2\pi\tau_{\text{QP}})$.

3.5.3 Two-Level System Noise

Nonthermal two-level system (TLS) fluctuations occur throughout the amorphous dielectric layer of the substrate. The TLS systems have electric and magnetic dipoles which can interact with external fields around the device. These interactions manifest as fluctuations in the complex permittivity and/or permeability of the material.
TLS noise depends on four parameters: frequency, readout power, temperature and the materials of both the superconducting resonator and the substrate.
The TLS noise can be modeled as a random fluctuations of the resonator capacitance C_r (see, e.g. [56]), which, however, are indistinguishable from fluctuations in kinetic inductance, both inducing the increase in resonant frequency with increasing base temperature.
In [56] a semi-empirical model for the TLS noise spectral density is presented, where the noise PSD has spectrum $S_{\text{X}} \propto f^{-\alpha}$ (where "X" refers to a generic label for a particular kind of signal) with spectral index $\alpha \sim 0.5$, and depends on microwave readout power and T_{base} as:

$$S_{\text{X, TLS}} \propto T^{-t} P_{\text{ro}} \tag{3.54}$$

where t = 1.5 -2.
NEP_{TLS} can be found by dividing equation 3.54 by a responsivity (e.g., R_T or R_P).

3.5.4 Amplifier Noise

KIDs require very low input power to be excited, and their output signal must be amplified by cryogenic LNAs. However, this amplification, even at low temperatures adds Johnson-Nyquist noise to the signal.

Johnson-Nyquist noise in a resistor arises from the thermal motions of electrons, resulting in voltage fluctuations across its terminals. According to [57], the RMS voltage contribution from Johnson-Nyquist noise is derived by considering a simple circuit model comprising a white noise generator with resistance R, which transfers power to a resistive load with resistance R_{L}. The power transferred from the noise generator to the load is:

$$P = \langle I^2 \rangle R_{\mathrm{L}} = \frac{\langle V^2 \rangle R}{(R + R_{\mathrm{L}})^2} \tag{3.55}$$

Considering a perfect match between the source and the load, R=R_{L}:

$$P = \frac{\langle V^2 \rangle}{(4R)} \tag{3.56}$$

and the RMS voltage is (assuming the resistance to be constant with respect to frequency):

$$\langle V^2 \rangle = 4RP = 4k_B T \int_{f_0}^{f_1} R\,df = 4k_{\mathrm{B}} T R B \tag{3.57}$$

where T is the temperature of the Thevenin equivalent of the circuit, and B is the bandwidth over which the voltage is being measured.
The PSD of the voltage fluctuations (in V^2/Hz, with $Z = R$ the input impedance of the LNA) is:

$$e_{\mathrm{V,\,amp}} = 4k_{\mathrm{B}} T_{\mathrm{amp}} Z \tag{3.58}$$

and PSD in frequency unit is obtained by diving by the voltage responsivity:

$$e^2_{\mathrm{f,\,amp}} = \frac{e^2_{\mathrm{V,\,amp}}}{|dV/df_0|^2} \tag{3.59}$$

Recalling equation 3.28, using that the probe frequency f_{pro} is the frequency at which a signal is sent into the system, the voltage responsivity is:

$$\frac{dV_{\mathrm{out}}}{df_0} = V_{\mathrm{in}} \frac{dS_{21}}{f_{\mathrm{out}}} \simeq -2jV_{\mathrm{in}} \frac{Q_{\mathrm{r}}^2 f_{\mathrm{pro}}}{Q_{\mathrm{c}} f_0^2} \frac{1}{\left(1 + 2jQ_{\mathrm{r}}\delta x\right)^2} \tag{3.60}$$

and near the resonance, $\delta x \ll 1$:

$$\frac{dV_{\mathrm{out}}}{df_0} \simeq -2jV_{\mathrm{in}} \frac{Q_{\mathrm{r}}^2}{Q_{\mathrm{c}} f_0} \tag{3.61}$$

Now recalling equation 3.59, it is possible to rewrite (in $\mathrm{Hz}^2/\mathrm{Hz}$):

$$e^2_{\mathrm{f,\,amp}} = 4k_{\mathrm{B}} T_{\mathrm{amp}} Z_0 \left(\frac{Q_{\mathrm{c}}^2 f_0^2}{4Q_{\mathrm{r}}^4} \right) = k_{\mathrm{B}} T_{\mathrm{amp}} \left(\frac{Q_{\mathrm{c}}^2 f_0^2}{Q_{\mathrm{r}}^4 P_{\mathrm{ro}}} \right) = k_{\mathrm{B}} T_{\mathrm{amp}} \left(\frac{f_0^2}{Q_{\mathrm{r}}^2 P_{\mathrm{ro}}} \right) \tag{3.62}$$

where $P_{\mathrm{ro}} = V_{\mathrm{in}}^2 / Z_0$ is the the probe tone power, and having assumed $Q_{\mathrm{r}} \simeq Q_{\mathrm{c}}$.
The LNA contribution to the NEP is:

$$NEP_{\mathrm{amp}} = \frac{e_{\mathrm{f,\,amp}}}{\frac{df_0}{dN_{\mathrm{QP}}} \frac{dN_{\mathrm{QP}}}{dP_{\mathrm{opt}}}} \tag{3.63}$$

3.5.5 Photon Noise

Photon noise depends on the total optical power P_{opt}, which is assumed to be an incoherent emission from a thermal blackbody source.
Let us consider a light with central frequency ν and bandwidth $\Delta\nu$. The total number of modes is the product of the number of spatial, temporal and polarization modes:

$$N_{\text{modes}} = N_{\text{spatial}} N_{\text{temporal}} N_{\text{pol}} = \left(\frac{A\Omega\nu^2}{c^2}\right)(\tau_{\text{int}}\Delta\nu)(n) \tag{3.64}$$

where $A\Omega$ is the optical throughput of the detector, τ_{int} is the integration time, n is the number of polarization modes (1 or 2).
The photon arrival times follow Bose-Einstein statistics, with a mean number of photons per mode and a blackbody temperature T , is:

$$n_{\text{occ}} = \frac{\langle N_{\text{phot}}\rangle}{\text{mode}} = \frac{1}{e^{h\nu/k_{\text{B}}T} - 1} \tag{3.65}$$

Fixing $n = 2$, the total optical power is:

$$P_{\text{opt}} = \left(N_{\text{mode}} \cdot \frac{\langle N_{\text{phot}}\rangle}{\text{mode}} \cdot \text{Energy per photon}\right)/\tau_{\text{int}} = \tag{3.66}$$

$$= \left(\frac{\text{nA}\Omega\nu^2}{c^2}\right)(\tau_{\text{int}}\Delta\nu)\, n_{\text{occ}} \frac{h\nu}{\tau_{\text{int}}} = \tag{3.67}$$

$$= \text{A}\Omega\Delta\nu\left(\frac{2h\nu^3}{c^2}\frac{1}{e^{h\nu/k_{\text{B}}T} - 1}\right) = \tag{3.68}$$

$$= \text{A}\Omega\Delta\nu B_\nu(\nu T) \tag{3.69}$$

where $B_\nu(\nu T)$ is the brightness of a black-body (the Planck law).
The incident power which is absorbed by the detectors is:

$$P_{\text{abs}} = \epsilon_{\text{opt}}\eta_{\text{det}} P_{\text{opt}} = \epsilon_{\text{opt}}\eta_{\text{det}} A\Omega\Delta\nu B_\nu(\nu T) \tag{3.70}$$

where ϵ_{opt} is the optical efficiency and η_{det} the quantum efficiency of the detectors.
The variance of n_{occ}, recalling that its probability distribution function is the Bose-Einstein distribution, is [58]:

$$\sigma^2_{\text{n}_{\text{occ}}} = n_{\text{occ}} + \frac{n^2_{\text{occ}}}{N_{\text{modes}}} \tag{3.71}$$

The mean-squared noise power input to the optical system is:

$$\sigma^2_{\text{P}} = \sigma^2_{\text{n}_{\text{occ}}} N_{\text{modes}}\left(\frac{h\nu}{\tau_{\text{int}}}\right) = \frac{h\nu P_{\text{opt}}}{\tau_{\text{in}}} + \frac{P^2_{\text{opt}}}{N_{\text{modes}}} \tag{3.72}$$

Finally, the noise spectral density is obtained by dividing equation 3.72 by the measurement bandwidth, $B = f_s/2 = \tau_{\text{int}}$:

$$S_X = \text{NEP}^2_{\text{phot}} = h\nu P_{\text{opt}} + \frac{P^2_{\text{opt}}}{N_{\text{modes}} B} \tag{3.73}$$

And in frequency units:

$$e_{\text{f, phot}} = \text{NEP}_{\text{phot}} \frac{d f_0}{d N_{\text{QP}}} \frac{d N_{\text{QP}}}{d P_{\text{opt}}} \tag{3.74}$$

3.5.6 Readout Noise

The readout noise is characterized by its PSD, S_X [X^2/Hz], which consists of two key components: additive white Gaussian noise (WN) and a $1/f$ (flicker noise, FN) component.
The WN is frequency-independent and results in a flat PSD, representing noise that is distributed uniformly across all frequencies. On the other hand, FN is frequency-dependent and dominates at lower frequencies, decreasing as the frequency increases. The $1/f$ knee, or corner-frequency f_c, is the frequency at which the flicker noise and white noise contributions are equal. This corner-frequency is critical in setting performance limits for the system. Specifically, it sets the lower limit for the telescope's scan speed and the readout rate necessary to map science targets effectively. If the scan speed is too slow, the flicker noise becomes dominant, degrading the signal-to-noise ratio and thus reducing the quality of the data. In contrast, a faster scan speed helps push the effective frequency of the noise above the 1/f knee, where white noise dominates, improving the overall signal quality.

3.5.6.1 White Noise

The WN level in each readout channel must be designed to be lower than the noise from both the LNA and the detectors, regardless of the multiplexing factor. The phase between the in-phase I and quadrature Q components of the readout signal is defined as $\Phi = \arctan(Q/I)$ and the PSD of this phase noise, S_Φ. is measured in of rad^2/Hz.
For convenience, the PSD S_Φ is often expressed in decibels relative-to-the-carrier (dBc/Hz), calculated as $10\log_{10}(S_\Phi)$). The noise from both the amplifier and the detectors is frequently expressed in terms of the PSD of their fractional frequency fluctuations, $S_{\delta f/f}$ (in [1/Hz]). According to [56], the phase noise S_Φ can be converted into fractional frequency noise $S_{\delta f/f}$ using a known or estimated the resonator's quality factor, Q_r:

$$S_{\delta f/f} = \frac{S_\Phi}{16 Q_r^2} \tag{3.75}$$

where $\frac{\delta f}{f} = \frac{\delta \phi}{4Q_r}$.
The frequency noise of the LNA $S_{\delta f/f,\text{ampl}}$ can be estimated according to [59]:

$$S_{\delta f/f,\text{ampl}} \simeq \frac{k_B T_N Q_c^2}{P_{ro} Q_r^4} \tag{3.76}$$

where k_B is Boltzmann's constant, T_N is the noise temperature of the LNA and P_{ro} is the power in the microwave probe tone.
The WN floor (in [dBc/Hz]) for a single probe tone is set by the bit-width of the ADCs. Given an effective number of bits (ENOB) and ADC sampling frequency f_s, this floor is:

$$WN_{\text{floor}} = -20\log_{10}\left(2^{\text{ENOB}}\right) - 10\log_{10}\left(f_s/2\right) \tag{3.77}$$

For an ENOB of 10-bits and f_s = 512 MHz, this noise floor is ≈-144 dBc/Hz.
For a multitone comb of N tones, the WN level of each tone can be estimated as:

$$WN_{\text{floor}} + 10\log_{10}(N) + \text{CF} \tag{3.78}$$

where CF is the crest factor of the waveform, in dB:

$$\text{CF} = 20\log_{10}\frac{|V_{\text{peak}}|}{V_{\text{rms}}} \tag{3.79}$$

3.6 Comparison with TESs

KIDs are often regarded as the successors to Transition-Edge Sensors (TESs), particularly in applications involving submillimeter, far-infrared, and millimeter-wave observations. TESs, which have a well-established track record, have been employed in numerous successful ground-based, balloon-borne, and space-based observatories. They are also the chosen technology for several ongoing and planned experiments, such as the Simons Observatory [60].
TESs consist of a superconducting absorber integrated into a voltage-biased circuit, operating near the edge of its superconducting transition. When photons are absorbed, the resultant heating increases the TES resistance, causing a drop in current under a constant voltage bias. This change is measured using a superconducting quantum interference device (SQUID) and a low-noise amplifier (LNA). The voltage bias introduces negative electrothermal feedback, enabling the TES to quickly return to its superconducting state after absorbing a photon.
While both KIDs and TESs are highly sensitive and effective astronomical detectors, they have distinct advantages and drawbacks, particularly in terms of their readout systems. TES readouts traditionally employ time-domain multiplexing (TDM), where multiple detectors are sequentially sampled using SQUID switches. However, TDM has inherent limitations, such as a finite multiplexing factor (typically 64–128, as achieved by [61] and by [62] and the need for extensive cryogenic wiring, which increases thermal noise. Although frequency-domain multiplexing (FDM) is now used in some TES systems (e.g. in [63]), it

does not entirely mitigate these challenges.
In contrast, KIDs inherently use FDM for readout, enabling them to read thousands of detectors via a single cryogenic feedline and LNA. Their readout electronics, apart from the LNA, are room-temperature, simplifying the system. However, KIDs lack the self-regulating mechanism provided by TES electrothermal feedback, which can make them more challenging to bias and operate. Additionally, KID signal processing must account for raw data corrections to relate the signal output to absorbed optical power.
Indeed, the primary distinction between these two devices lies in their system NEP. As demonstrated in the equations describing KIDs, their NEP is inherently dependent on the absorbed power, whereas TESs exhibit NEP components that also remain independent of the absorbed power.
Despite these differences, both technologies remain essential in advancing astronomical instrumentation, with their suitability often determined by specific experimental requirements. A comprehensive comparison can be found in [49].

Chapter 4

COSMO readout: Firmware & Software implementation

This chapter is dedicated to the description of the COSMO electronics readout firmware and software.
In particular there will be a comprehensive description of the generation, acquisition and analysis of the tones, together with the implementation of tones searching, and a brief description of the GUI (Graphical User Interface).
The software developed by me is written in LabVIEW, while the majority the firmware was written in VHDL by the electronic engineer working at Milano-Bicocca.

4.1 Considerations about the COSMO Firmware and Software

Figure 4.1 presents a schematic of the functionalities of the COSMO readout electronics firmware and software.
After initializing the parameters to allow the Firmware to work, the user can choose between finding the resonance frequencies of the KIDs or sending and acquiring the comb signal (a broad-spectrum signal composed of the frequencies used to simultaneously read out multiple KIDs pixels) to measure the amplitude and phase variation of the KIDs, if the resonance list is already known.
The process for finding the resonance frequencies is described in detail in section 4.3 and section 4.4.
Regarding the comb signal, here are some considerations. The synthesized sequence generating the comb follows a fixed pattern: data are stored in a block RAM inside the FPGA chip, and they are periodically fed to the DACs (Digital to Analogue Converter).
The generated waveform is continuous, allowing for cyclic reading and avoiding discontinuities. A detailed description is in section 4.2.2. This enables the use of the Digital Down Conversion (DDC) strategy to evaluate the amplitude and phase variations of each KID tone, as explained in section 4.2.3. DDC is im-

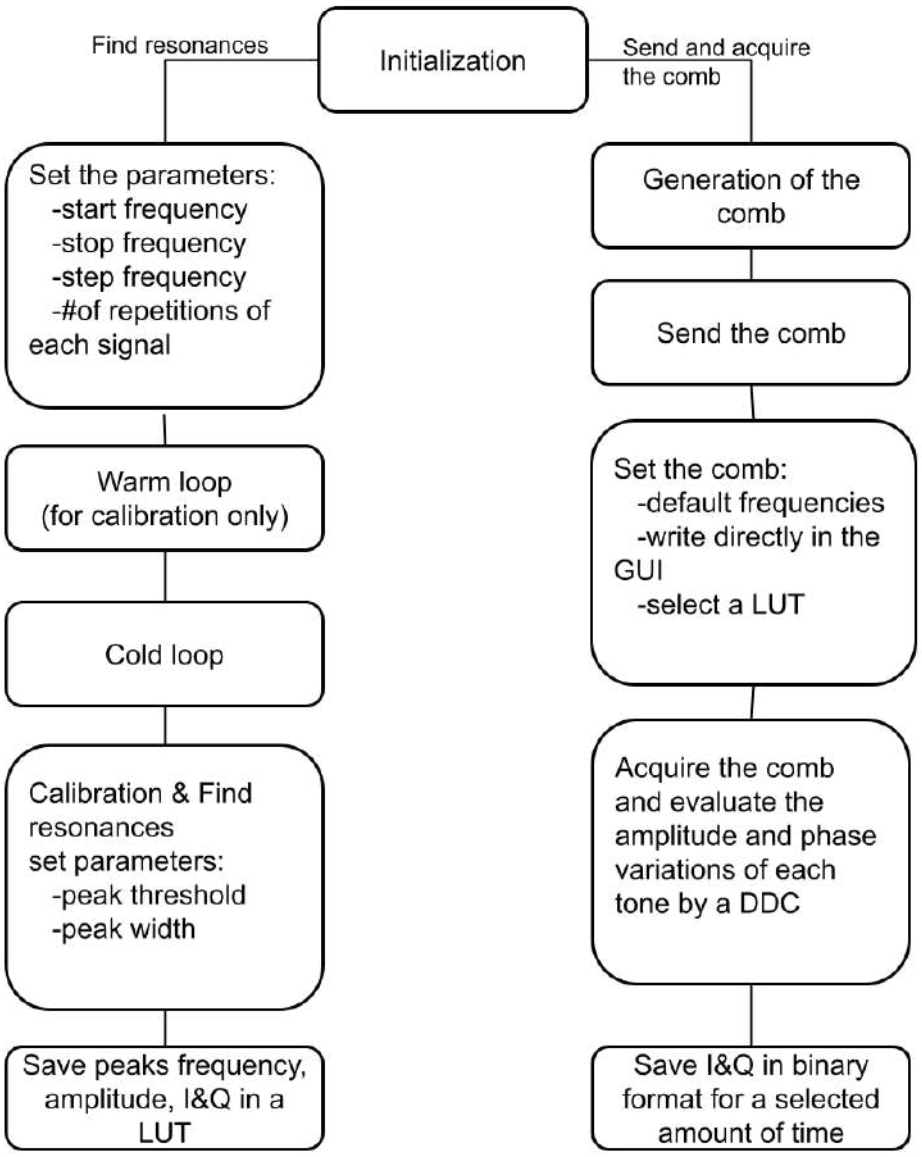

Figure 4.1: Schematic of the functionalities of COSMO firmware and software.

plemented in the firmware, as detailed in section 4.2.4. However, this approach imposes a limitation, as it precludes the generation of arbitrary waveforms. Specifically, the choice of a sampling rate of approximately 60 kHz, as explained in section 2.4, limits the available waveforms to multiples of this value.
The reading structure of the acquired signal is limited by the two ADCs (Analog-to-Digital Converters), which operate at 250 MS/s. The waveform memory consists of 4096 samples. The choice of 4096 samples is based on the following considerations:

- the target sampling rate is up to 60 kHz, so the integration time of each sample can be as short as $1/(60 \cdot 10^3$ Hz)= 16 μ s

- With the ADCs' sampling rate of 250 MS/s, the time per sample is $\rightarrow$ $1/(250 \cdot 10^6) = 4$ ns
- Therefore, 16 μ s / 4 ns=4000, which is approximately 4096 (the nearest power of 2, 2^{12})

The implication of this choice is that if the sampling rate of the readout needs to be halved, the memory size would need to be doubled, requiring more resources.

4.2 Theory of tones detection

4.2.1 IQ modulation

Let us start from a brief mathematical description of I-Q modulation.
Let us call the frequency of the LO, ω_{LO} (typically called the carrier frequency), and let us put the LO frequency at the middle of the base-band, and let us consider a signal S with frequency ω. Such sinusoidal curve can be decomposed into the in-phase (I=cos(ωt)) and quadrature (Q=sin(ωt))) components. Also the LO signal S_{LO} can be decomposed into the in-phase I_{LO}=cos($\omega_{LO} t$) and quadrature Q_{LO}=sin($\omega_{LO} t$) components. Both signals S an S_{LO} are sent to the mixer that multiply them component by component.
Multiplying the signal S for the LO signal S_{LO}, there are the *up* and *down* components (where the *down* component is generated when the Q signal is phase-shifted by π, which is also equivalent to switching I with Q):

$$S_{\mathrm{LO}}\, S = I_{\mathrm{LO}}\, I - Q_{\mathrm{LO}}\, Q + i\,(I_{\mathrm{LO}} Q + Q_{\mathrm{LO}} I) \tag{4.1}$$

and:

$$I_{\mathrm{up}} = I_{\mathrm{LO}}\, I = \frac{1}{2}\cos((\omega_{\mathrm{LO}} + \omega)\, t) + \frac{1}{2}\cos((\omega_{\mathrm{LO}} - \omega)\, t) \tag{4.2}$$

$$I_{\mathrm{down}} = I_{\mathrm{up}} \tag{4.3}$$

$$Q_{\mathrm{up}} = Q_{\mathrm{LO}}\, Q = \frac{1}{2}\cos((\omega_{\mathrm{LO}} - \omega)\, t) - \frac{1}{2}\cos((\omega_{\mathrm{LO}} + \omega)\, t) \tag{4.4}$$

$$Q_{\mathrm{down}} = -Q_{\mathrm{up}} \tag{4.5}$$

The total signal is the sum of the components:

$$S_{\mathrm{up}} = I_{\mathrm{up}} + Q_{\mathrm{up}} = \cos((\omega_{LO} + \omega)\, t) + i \sin((\omega_{LO} + \omega)\, t) \tag{4.6}$$

$$S_{\mathrm{down}} = I_{\mathrm{down}} + Q_{\mathrm{down}} = \cos((\omega_{LO} - \omega)\, t) + i \sin((\omega_{LO} - \omega)\, t) \tag{4.7}$$

As it is shown in equation 4.6 and equation 4.7, it is possible to achieve both higher and lower frequencies with respect to the signal.
IQ modulation is a way to move signals from baseband to RF, while the inverse process (moving the signal from RF back to the baseband frequency) is the IQ demodulation. In general this process enables the generation and acquisition of

signals in the baseband frequency domain, allowing communication with devices operating at higher frequencies, such as, in this case, KIDs. Moreover, dealing with signals in the baseband domain typically results in more manageable signal processing, as it involves lower frequencies and simpler circuitry compared to RF processing.
However, as shown before, when modulating a signal using IQ modulation results in a spectrum with both positive and negative frequency components. These components are mirrored around the carrier frequency due to the nature of the modulation process. Thus it's essential to eliminate one of these mirrored components in order to avoid redundancy and reduce interference from adjacent channels or unwanted frequency components, leading to improved signal quality and system performance.
This can be done using both filters and, in the case of the choice of this readout electronics components, also using single-side band modulator and demodulator.

4.2.2 Generation of the comb signal

The signal is digitally generated and then it is converted into voltages using DACs. Such output signal is the sum of sinusoidal functions of all the frequencies needed to excite the KIDs array. This is also known as *comb* signal.
The digital generation of a single frequency f with phase ϕ is a finite sequence of sines and cosines:

$$I_{\text{tone}_k} = \sum_{n=0}^{N-1} A_n \cos\left(2\pi \frac{f_k}{f_{\text{DAC}}} n + \phi\right) \tag{4.8}$$

$$Q_{\text{tone}_k} = \sum_{n=0}^{N-1} A_n \sin\left(2\pi \frac{f_k}{f_{\text{DAC}}} n + \phi\right) \tag{4.9}$$

where f_{DAC} is the DAC sample rate, and A_n is the amplitude of the $n-$th signal. The comb is thus obtained by summing the sines and cosines signals with different frequency f of each of the k tones. This readout electronics has been developed to generate and acquire a maximum of 18 tones, corresponding to the number of pixels of COSMO KIDs, as explained in 2.3.
There are few considerations to take into account before going on:

- The amplitude A_n should be maximized to enhance the signal quality, while ensuring it does not exceed the dynamic range of the DAC. Specifically, the maximum value of the sum of all amplitudes must not exceed $2^{N_{\text{bit}}-1}$.

- The phase of each tone is initially set to zero. However, randomizing the phases may be preferred to mitigate potential spikes and excess noise. When all phases are set to zero, the initial power is particularly high, causing an initial spike. Nonetheless, this spike does not affect the functionality of the readout electronics.

- The generated sequence has a finite length since it has to be saved, determined by the duration of the DAC output, which is equal to the inverse of its sample rate f_{DAC}. Consequently, the number of samples in a period T is given by $N_{\mathrm{s}} = T f_{\mathrm{DAC}}$. It is necessary for the sequence to be cyclically repeatable to avoid discontinuities across cycles. However, this requirement imposes limitations on the available frequencies. If a signal is not an integer multiple of f_{DAC}/N, a discontinuity would be generated, leading to spurious frequencies.

4.2.3 Digital Down Conversion

After the signal is generated and converted from digital to analog domain, it passes through the analog components of the readout electronics and eventually stimulates the detectors. Subsequently, the signal needs to be analog-to-digital converted, acquired, saved, and analyzed.
The chosen strategy for the COSMO readout electronics is to employ Digital Down Conversion (DDC) to analyze the acquired signal. The DDC translates one or more intermediate frequency (IF) channels, centered around specified frequencies, into base-band signals. This enables easier processing and analysis of the signals.
DDC is performed *digitally*, which offers flexibility in terms of adjusting parameters such as center frequency, bandwidth, filtering characteristics without the need for hardware modifications, and it allows to achieve high speed in the digital processes. Moreover, DDC facilitates the simultaneous processing of multiple channels or bands.
Finally, its mathematical description is very close to the IQ modulation explained in 4.2.1.
Let us consider the comb signal S with amplitude A_{comb}, frequency ω_{comb} and phase ϕ_{comb}. It can also be represented as N cosine and sine functions with different amplitudes and phases:

$$\begin{aligned} S = A_{\mathrm{comb}}\left[\cos\left(\omega_{\mathrm{comb}} t + \phi_{\mathrm{comb}}\right) + i \sin\left(\omega_{\mathrm{comb}} t + \phi_{\mathrm{comb}}\right)\right] = \\ = \sum_{i=1}^{N} A_i \left[\cos\left(\omega_i t + \phi_i\right) + i \sin\left(\omega_i t + \phi_i\right)\right] \end{aligned} \tag{4.10}$$

At this point, it is necessary to ensure that the available frequencies are quantized, ensuring that each period aligns with an integer multiple of the FPGA duty cycle time T, as explained in section 4.2.2. In other words, the COSMO readout electronics' cycle time is 16.38μs (corresponding to a sampling rate of around 60 kHz, its inverse), and the frequencies have to fulfill the condition:

$$\omega_i = \frac{2\pi n}{T} \qquad n \in \mathbb{Z}^+ \tag{4.11}$$

The goal is to extract the amplitude and phase of each individual sinusoidal function that makes up the comb signal.

To achieve this, the signal S needs to be split into its I and Q components:

$$S_I = \sum_{i=1}^{N} A_i \cos\left(\omega_i t + \phi_i\right) \tag{4.12}$$

$$S_Q = \sum_{i=1}^{N} A_i \sin\left(\omega_i t + \phi_i\right) \tag{4.13}$$

These components must be treated separately but in a similar manner.
For simplicity, let us consider the I component and the index $i = 1$ in equation 4.12 (thus I am taking into account the first frequency value). This signal is then multiplied by the sine of the frequency to be extracted (in this example, the frequency value corresponding to the first one sent, ω_1):

$$S_1 = S_I \cdot \sin(\omega_1 t) = \sum_{i=1}^{N} \left[\frac{A_i}{2} \sin\left((\omega_i - \omega_1) t + \phi_i\right) + \frac{A_i}{2} \sin\left((\omega_i + \omega_1) t + \phi_i\right) \right] \tag{4.14}$$

and this expression can be rewritten to underline the information being searched for:

$$S_1 = \frac{A_1}{2} \sin(\phi_1) + \sum_{i=2}^{N} \frac{A_i}{2} \sin\left((\omega_i - \omega_1) t + \phi_i\right) + \sum_{i=1}^{N} \frac{A_i}{2} \sin\left((\omega_i + \omega_1) t + \phi_i\right) \tag{4.15}$$

Then, by utilizing the periodicity described in equation 4.11, and the fact that all the summations have a null mean over a period T, the result is:

$$\langle S_1 \rangle_T = \frac{A_1}{2} \sin(\phi_1) \tag{4.16}$$

Thus, after performing the same calculation with the S_Q signal (which, of course, has to be multiplied by $\cos(\omega_1 t)$), both the amplitude and phase of the first tone can be extracted.
Finally, this process can be performed for all the other tones in order to get each A_i and ϕ_i.

4.2.3.1 Digital Down Conversion vs Fast Fourier Transform

The DDC for a small number of tones as in this application (18 tones), has a lower computational complexity with respect to the Fast Fourier Transform (FFT) algorithm. Indeed, the DDC performs $\mathcal{O}(nN)$ operations, where n is the number of tones (here 18) and N is the number of samples in the input signal.
DDC involves processing each tone individually, resulting in a linear scaling with both the number of tones (n) and the number of samples (N). Conversely, the FFT algorithm has a computational complexity of $\mathcal{O}(N \log N)$. While the FFT becomes highly efficient for large datasets (specifically when $n > \log_2 N$) due to its logarithmic complexity scaling with the number of samples N, it may not offer significant advantages over DDC when dealing with a small number of

tones. Additionally, when computational resources are limited, DDC provides a practical solution due to its simpler processing requirements.
Finally, in DDC, each tone is processed independently, meaning that if an error occurs during the processing of a specific tone, it only affects that particular tone. Since the calculations associated with each tone are carried out separately, errors can be localized to individual tones, making them easier to identify and correct. On the other hand, in FFT, the values of all tones are intertwined throughout the computation until the final step. This means that if an error occurs at any point during the FFT computation, it can propagate and affect all tones, making it challenging to isolate and correct the error. The tangled nature of FFT computations makes it difficult to trace back errors to their source.

4.2.3.2 Digital Down Conversion inaccuracy

While DDC offers advantages in certain scenarios, it also has drawbacks that need to be considered, particularly regarding its frequency selectivity and susceptibility to frequencies that do not satisfy the quantization equation 4.11.
Regarding frequency selectivity, DDC is narrow around the selected frequencies due to the nature of the downconversion process. This means that it may not be effective in capturing signals that are spread across a wide frequency range or signals that fall outside the selected frequency bands. Moreover, frequencies that do not exactly satisfy the quantization equation of the DDC can introduce inaccuracies in the measurements of the amplitudes and phases of the tones. This is because the DDC is designed to process signals at specific frequencies determined by the sampling rate and the number of samples, and frequencies that do not align with these quantized values may not be accurately captured or may introduce errors into the measurements. Non-quantized frequencies, as well as noise with different frequencies, can introduce errors into the measurements made by the DDC.
Let's delve into a more quantitative analysis focusing on the effect DDC on a single tone with an arbitrary frequency ω_1, which undergoes downconversion to a frequency ω_0. Thus, considering for example the component I, equation 4.12 becomes:

$$S_I = A\cos\left(\omega_1 t + \phi\right) \tag{4.17}$$

After downconversion the signal S_I becomes:

$$S_{\mathrm{DDC}} = S_I \cdot \sin\left(\omega_0 t\right) = \frac{A}{2}\sin\left(\left(\omega_0 + \omega_1\right) t + \phi\right) + \frac{A}{2}\sin\left(\left(\omega_0 - \omega_1\right) t + \phi\right) \tag{4.18}$$

The mean over a period T is the integral over such period:

$$S' = \frac{1}{T}\int_0^T S_{\mathrm{DDC}}\, d\mathrm{t} =$$

$$= \begin{cases} \frac{A}{2}\sin(\phi) & \text{if } \omega_1 = \omega_0 \\ -\frac{A}{2T}\left[\frac{\cos\left((\omega_0+\omega_1)T+\phi\right)-\cos\phi}{\omega_0+\omega_1} + \frac{\cos((\omega_0-\omega_1)T)+\phi-\cos\phi}{\omega_0-\omega_1}\right] & \text{if } \omega_1 \neq \omega_0 \end{cases} \tag{4.19}$$

Considering the case $\omega_1 \neq \omega_0$, with $\omega_1 - \omega_0 = \Delta\omega \ll \omega_0$, a first order approximation of the previous result is:

$$S' = \frac{A}{2}\left[\sin\phi + \frac{1}{2\omega_0}\left(\sin\phi - \omega_0 T \Delta\omega \cos\phi\right)\right] + o(\Delta\omega T) \tag{4.20}$$

$\Delta\omega$ allows to quantify how much the downconverted frequency deviates from the original frequency. A smaller value of $\Delta\omega$ indicates a higher accuracy of the downconversion process, while a larger value indicates greater inaccuracy.
In equation 4.20, when $\omega_0 \gg 1/T$, the error introduced by a frequency misalignment is the lowest for $\phi = \pi/2$ and the highest when for $\phi = 0$.

4.2.4 Tone detection: implementation on FPGA

Once the comb signal returns, it undergoes digitization by ADCs and subsequent analysis.
Specifically, the COSMO readout electronics employs two ADCs: one for the I component and one for the Q component, each operating at 250 MS/s (half of the DACs' speed).

As previously mentioned, each tone can be processed independently. This is achieved by dedicating specific portions of the FPGA to the analysis of each tone, facilitating efficient parallel processing of multiple tones simultaneously.
The firmware part responsible for analyzing each tone is called the *tone detector*. In total, there are 18 independent tone detectors running in parallel, with each one dedicated to analyzing a specific tone.
At the arrival of each sample, the following operations must be performed at the same rate:

- acquisition of I and Q signals
- multiplication of I and Q signals with the multiplicative parameters p_j and accumulation of the results:

$$p_j = 2^{\text{bit}-1}\sin\left(2\pi\frac{f}{f_{DAC}}j\right) \tag{4.21}$$

  Thus the result signals, normalized by $N2^{\text{bit}-1}$, in order not to exceed the

maximum, as discussed in section 4.2.2, are:

$$S_I = \frac{1}{N 2^{\text{bit}-1}} \sum_{j=0}^{N-1} p_j I_j \tag{4.22}$$

$$S_Q = \frac{1}{N 2^{\text{bit}-1}} \sum_{j=0}^{N-1} p_j Q_j \tag{4.23}$$

Indeed, when a new sample is measured, it is multiplied by the corresponding parameter, and their sum is accumulated. At the end of the period, the sum are S_I and S_Q. When a new period starts, the accumulated number is reset to 0.

The multiplicative parameters are computed by the host computer prior to acquisition, specifically when the tones are modified or initially selected, and then they are stored in memory.
A shared buffer is utilized for loading the parameters linked to different tones, necessitating the identification of each tone detector by a unique ID number.

4.3 Searching for resonant tones: chirp

In order to excite a resonance, it is necessary to know its frequency, which also depends on temperature. For this reason it is mandatory that our readout electronics is able to find the resonant frequencies of the detectors.
The strategy implemented here involves the use of chirp signals. A chirp signal is a sinusoidal time varying signal characterized by an amplitude A and an instantaneous generic phase ϕ:

$$\text{chirp}(t) = A\cos\big(\phi(t)\big) \tag{4.24}$$

In a linear chirp (a chirp signal in which the frequency increases or decreases linearly over time), the instantaneous frequency can be written as:

$$f(t) = \beta t + f_0 \qquad \text{where: } \beta = \frac{f_f - f_0}{t_f - t_0} \tag{4.25}$$

where f_0 is the initial (sweep) frequency at time t_0, f_f is the final (sweep) frequency in the time window bounded by the final (sweep) time t_f, and β is the changing rate.
For a linear chirp, the instantaneous frequency is defined as the derivative of the phase $\phi(t)$ with respect to time: $\frac{d}{dt}\phi(t) \equiv 2\pi f(t)$, and thus the phase is found by integrating the rate of change:

$$\phi(t) = \phi(t_0) + 2\pi \int_0^t f(\alpha) d\alpha = \phi(t_0) + 2\pi\left(f_0 t + \frac{\beta t^2}{2}\right) \tag{4.26}$$

Thus equation 4.24 for a linear chirp becomes:

$$\text{chirp}(t) = A\cos\left(2\pi\left(f_0 t + \frac{\beta t^2}{2}\right)\right) \tag{4.27}$$

4.3.1 Chirp strategy

The strategy implemented is the following. The basic idea is to divide the entire frequency band into small sub-bands (where ideally at least one resonance can be found), send a chirp signal through the analog electronics and eventually the detectors, acquire the signal and evaluate its variation. The Fast Fourier Transform (FFT) is then applied to analyze the frequency content: in the absence of any KID resonance, the FFT of the signal within a small sub-band is expected to be closer to a delta function, peaked at a certain frequency. However, when the chirp signal excites a resonant tone, the FFT signal becomes broader, indicating the presence of a KID resonance.
On the contrary, analyzing the entire frequency band with only one chirp signal results in the FFT capturing all frequency components simultaneously, leading to overlapping signals that are indistinguishable.
The final goal, as said before, is to find the KIDs resonant frequencies, saved them in a LUT to be recalled when the comb signal needs to be sent to the KIDs in order to excite them and evaluate the amplitude and phase variation.
Operationally, the chirp is represented as a complex number, where the real part corresponds to the signal's amplitude, and the angle of the complex number is determined by the product of two distinct linear functions with different slopes. The first function is defined between the start and stop frequencies, accounting for the frequency variation over time. The second function defines the time progression, which is based on the number of samples and the sampling rate. These two functions together create the characteristic frequency sweep of the chirp signal.

4.3.2 Chirp how to use: an example with the Nb KIDs

As already mentioned in section 2.4, the majority of the tests are done with Nb KIDs present in the criofacility at University of Milano-Bicocca. Specifically, this test was performed in the 4 K cryocooler cooled by a SHI RDK-408D2 Gifford-McMahon. The Nb KIDs have resonant frequencies between ∼1.893 GHz and ∼ 2.040 GHz (at a temperature $T \simeq 5$ K), spanning a total band of around 150 MHz. The Nb KIDs working frequencies are then reached by the readout electronics by placing the LO approximately at the middle of the desired RF band, and where no other tones are present. In this test and with this temperature ($T \simeq 5$ K), the LO was placed at 1.957 GHz, after having looked at the S_{21} scattering parameter obtained by the VNA (Vector Network Analyzer).
Independently of the real KIDs bandwidth, this readout electronics has a limited bandwidth due to the SLP-44+ analog filters, placed at the input and output of the transceiver, as explained in section 2.4. Thus, to perform the chirp measurement (as described in section 4.3.2), I decided to split the effective 90 MHz bandwidth into sub-bands of 150 kHz width, which appeared to me a reasonable choice because the width of the Nd KIDs resonances (approximately 400 kHz).

Before finding the KIDs resonances, it is a good practice also to normalize the final result so that it is possible to compare the chirp result to a VNA sweep (and thus the readout electronics can be also used in a VNA-like configuration, also very useful to evaluate some properties of the KIDs themselves).
The steps towards the normalization are the following:

- acquisition of the so called *warm loop*, in figure 4.2. With this slang-terminology I am describing the procedure of making the signal passing through all the components of the readout electronics only without entering the cryostat (and so we call it *warm*). Referring to figure 2.11, this signal path corresponds to skipping the cryostat box.

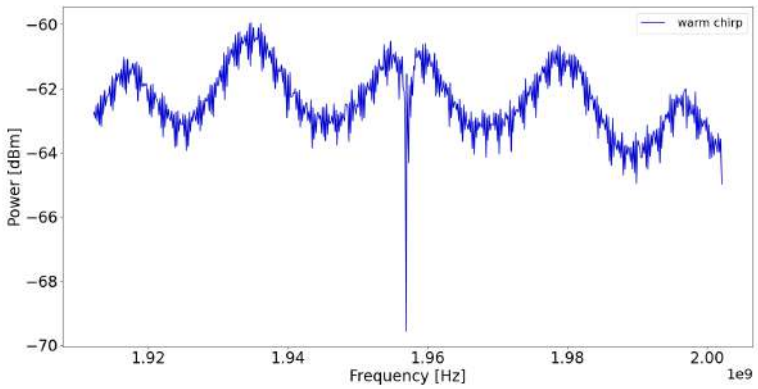

Figure 4.2: Warm loop chirp.

- acquisition of the so called *cold loop*, in figure 4.3. With this slang-terminology I am describing the procedure of making the signal passing through all the components of the readout electronics, and also through cryostat exciting the KIDs (and thus is *cold*). Referring to figure 2.11, this signal path corresponds to a complete loop of the signal, passing through each component represented in the figure.
- evaluating the normalization factor ($\text{Fact}_{\text{norm}}$): $\text{amplitude}_{\text{cold}}/\text{amplitude}_{\text{warm}}$ and getting the median value.
- the calibrated chirp is given by: $\text{amplitude}_{\text{cold}} - (\text{amplitude}_{\text{warm}} \cdot \text{Fact}_{\text{norm}})$ (figure 4.4)

From figure 4.4, the frequencies of the resonant tones are found by using a peak detector VI function implemented in LabVIEW, after having fixed a threshold and a width value of the peaks.
At the end, the tones and their amplitude are saved.
Then, this method of getting the S_{21} scattering parameter (as described in eq. 3.28) and finding the resonances is also compared to what can be measured with the VNA. The comparison among the frequencies found using the VNA and our

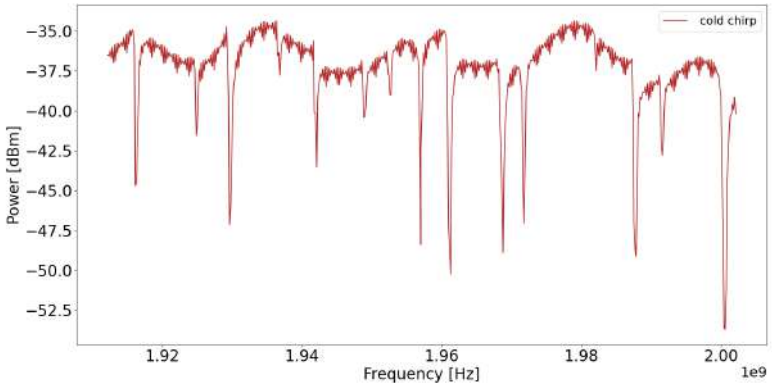

Figure 4.3: Cold loop chirp.

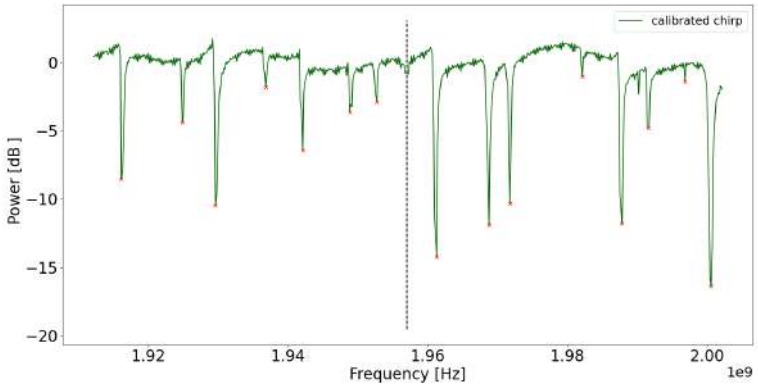

Figure 4.4: Calibrated chirp. The vertical dotted line is the LO position.

readout electronics is visible in figure 4.5 (note that as said before, the COSMO readout electronics with the SLP-44+ filters has a bandwidth of around 90 MHz, while the Nb KIDs array spans over around 150 MHz).
The process of searching for resonance frequencies takes a variable amount of time depending on how many times each chirp step are repeated. For example there is no need to repeat more than once each chirp step in the warm configuration, while there is the need to repeat at least 3 times each step chirp in the cold case, in order to mitigate the effect of the 1 Hz oscillation inside the 4 K cryocooler.
In the first case the chirp takes about 4 minutes, and it scales linearly with the number of repetitions of each chirp step.

4.4 Searching for resonant tones: another strategy

The chirp strategy to find the resonances described above has no limitations when dealing with our Nb KIDs, as they have wide resonances and thus the

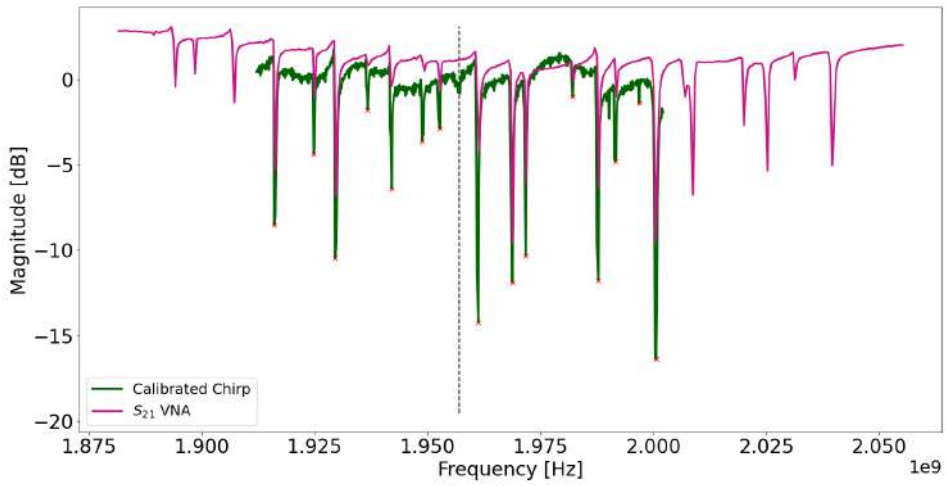

Figure 4.5: Comparison between the S_{21} parameter found by the COSMO readout electronics (in green) and the VNA together with a LNA inside the cryostat (in purple). The VNA signal is down-shifted to bring it closer to the other signal. The dotted black vertical line represents the LO position.

frequency resolution is low. However, it is not optimal when dealing with resonators with narrower resonances.
Indeed when the resonances are deeper and narrower, a smaller step frequency is required to detect with sufficient accuracy the position of the transmission minima. The limitation given by the above strategy (chirp) is determined bt the fact that the minimum step frequency corresponds to the sampling frequency (approximately 60 kHz).
COSMO KIDs are expected to be similar to the OLIMPO ones [64], with a Q-factor of the order of few 10^4 and a width of approximately 20 kHz. This requires a sampling rate between 1 and 2 kHz in order to accurately reconstruct the curve as described by equation 3.28.
The solution to this problem is achieved by generating in the firmware a very precise tone by performing a CORDIC algorithm, and evaluating its variation when a resonance is present.

CORDIC stands for Coordinate Rotation Digital Computer. It's an iterative algorithm used for efficiently calculating various mathematical elementary functions, particularly sine and cosine, as in this case. The CORDIC algorithm operates by iteratively rotating a vector through a series of small angles until it reaches the desired angle or achieves the desired result.
One of the key features of CORDIC is its ability to perform these calculations using only simple operations such as shifts, additions, and lookup-tables, making it suitable for implementation in hardware on simple processors.

Let us describe the rotation of a vector:

Iteration	θ	$\cos(\theta)$	$\tan(\theta)$
0	45°	0.70710678	1
1	26.565°	0.89442719	0.5
2	14.036°	0.9701425	0.25
3	7.1250°	0.99227788	0.125
4	3.5763°	0.99805258	0.0625
5	1.7899°	0.99951208	0.03125
6	0.89517°	0.99987795	0.015625
7	0.44761°	0.99996948	0.0078125
8	0.22381°	0.99999237	0.00390625
9	0.11191°	0.99999809	0.001953125
10	0.055953°	0.99999952	0.0009765625

Table 4.1: CORDIC LUT with $n = 10$

- the initial vector has coordinates: $(x_{\text{in}}, y_{\text{in}})$
- the vector is then rotated by an angle θ, reaching the coordinates $(x_{\text{R}}, y_{\text{R}})$:

$$\begin{bmatrix} x_{\text{R}} \\ y_{\text{R}} \end{bmatrix} = \cos\theta \begin{bmatrix} 1 & -\tan\theta \\ \tan\theta & 1 \end{bmatrix} \begin{bmatrix} x_{\text{in}} \\ y_{\text{in}} \end{bmatrix} \tag{4.28}$$

From equation 4.28, a rotation implies four multiplication (and additions), however in the FPGA it is preferable to reduce as much as possible them.
Indeed, the CORDIC algorithm permits to perform rotations without multiplications based on this procedure:

1. rotate the initial vector by an arbitrary angle θ is equal to rotate the vector by several smaller angles, as:

$$\theta = \sum_{i=0}^{n} \theta_i \tag{4.29}$$

2. the small angles θ_i can be chosen in a way that:

$$\tan(\theta_i) = 2^{-i} \qquad \text{for } i = 0, 1, ..., n \tag{4.30}$$

The accuracy of calculations increase with the number n.
The multiplications by $\cos(\theta)$ act as scaling factor, k, since both the x and y components need to be multiplied by the same scaling factor.
From equation 4.30, a CORDIC LUT with arbitrary precision can be obtained: see table 4.1. Moreover, once the number of iterations is fixed (i.e. $n = 10$), it is

possible to directly evaluate the scaling factor and store it:

$$K = \cos(45^\circ) \cdot \cos(26.565^\circ) \cdot \ ... \ \cdot \cos(0.055953^\circ) \simeq 0.60725303 \tag{4.31}$$

Therefore, omitting the scaling factor term, the equations for the CORDIC algorithm are:

$$\begin{cases} x[i+1] = x[i] - \sigma_i 2^{-i} y[i] \\ y[i+1] = y[i] + \sigma_i 2^{-i} x[i] \end{cases} \tag{4.32}$$

where $\sigma_i \in \{+1, -1\}$ determines the sign of the elementary angle.
These equations show that the CORDIC algorithm always performs a certain number of rotations with the predefined angles (i.e., 10 rotations), and the only thing that the algorithm must determine is whether each rotation is clockwise ($\sigma_i = +1$) or counter-clockwise ($\sigma_i = -1$) during each iteration.
The way the rotation is chosen to be clockwise or counter-clockwise is the following: if the desired rotation is larger (smaller) than previously achieved rotation, then rotation is counter-clockwise (clockwise) in the next iteration. This process applies until all the n iterations of the algorithm are performed.
The error is given by:

$$\theta_{\text{error}} = \theta - \sum_{i=0}^{n} \theta_i \tag{4.33}$$

and thus equation 4.32 becomes:

$$\begin{cases} x[i+1] = x[i] - \sigma_i 2^{-i} y[i] \\ y[i+1] = y[i] + \sigma_i 2^{-i} x[i] \\ z[i+1] = z[i] - \sigma_i \tan^{-1}\left(2^{-i}\right) \end{cases} \tag{4.34}$$

where the equation for z accounts for the error.
In this way it is possible to generate a very precise monochromatic frequency, whose amplitude variation can be detected.

4.4.1 CORDIC Strategy

Compared to the chirp-based strategy, the CORDIC one must be a firmware-implemented approach, in order not to suffering by the limitation due to the sampling frequency (approximately 60 kHz)
The chosen CORDIC precision is as follows:

- number of iterations, n: 17
- word length in FPGA: 26 (26 bits fixed point)

These values are chosen to be a good compromise between using too many FPGA resources and achieving a useful precision. Thus, with this architecture the precision in the generated frequency with the selected COSMO DACs and ADCs is approximately 7 Hz, which is notably high.

Frequency range [MHz]	Minimum step frequency
3000 - 6000	5 kHz
1500 - 3000	2.5 kHz
750 - 1500	1.25 kHz
375 - 750	1 kHz
187.5 - 375	500 Hz
93.75 - 187.5	250 Hz
46.875 - 93.75	100 Hz
23.4375 - 46.875	50 Hz

Table 4.2: LO (Valon 5009) minimum step frequency increment with external reference as function of the output frequency range.

The primary limitation, however, could be dictated by the Local Oscillator (LO) minimum step size, as detailed in table 4.2. However, several tests were conducted to verify that by shifting the monochromatic frequency generated with the CORDIC, even with the minimum step (7 Hz) and with larger steps, the actual output frequency from the electronics was as requested, without limitations due to the LO.
With this architecture, it is possible to send one tone at time. Therefore, to meet the requirement of sending multiple frequencies so that to sweep the entire band, I implemented a for-loop cycle that considers the start, stop and step frequencies.
The acquisition of the signal, given that one tone is sent at a time, involves simply capturing the amplitude, normalizing it, and converting it in dBm.
The results are saved in a text file with four columns: frequency, I, Q, and amplitude.

4.4.2 CORDIC how to use: an example with the Al KIDs

As described in 4.3.2, the same considerations and procedure apply here:

- warm signal: in figure 4.6.
- cold signal: in figure 4.7.
- evaluating the normalization factor ($\text{Fact}_{\text{norm}}$): $\text{amplitude}_{\text{cold}}/\text{amplitude}_{\text{warm}}$ and getting the median value.
- the calibrated chirp is given by: $\text{amplitude}_{\text{cold}} - (\text{amplitude}_{\text{cold}} \cdot \text{Fact}_{\text{norm}})$ (figure 4.8)

The resonant tones also in this case are found by using the peak detector function VI, after having fixed a threshold and a width value, as reported in 4.3.2,

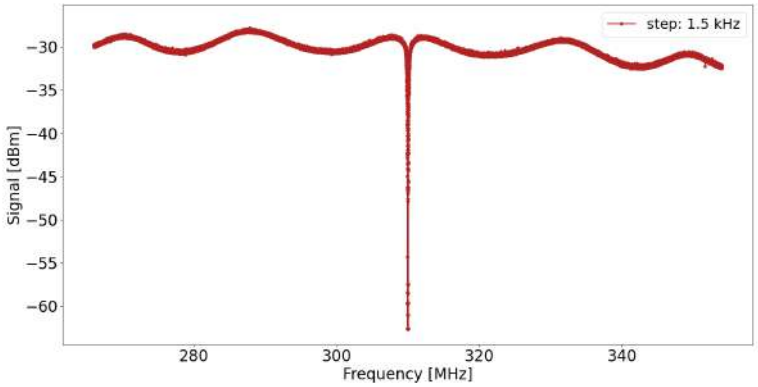

Figure 4.6: Warm signal of the entire band, with a frequency step of 1.5 kHz, and the LO placed at 310 MHz.

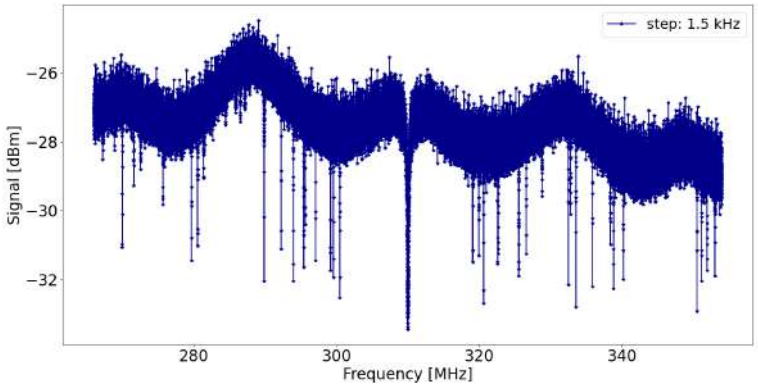

Figure 4.7: Cold signal passing through the cryostat, exciting the KIDs, with a frequency step of 1.5 kHz, and the LO placed at 310 MHz. Note that the signal background (the part without resonances) is broad and noisy because KIDs require very low power, which need to be amplified before acquired (also with a warm amplifier), degrading the signal-to-noise ratio.

and, at the end, frequency, I, Q, and amplitude are saved.
Performing this method with 90 MHz bandwidth with a step frequency of 1 kHz takes about 20 minutes.

4.5 Data saving

Files are saved as binary format following this structure:

- line 1-36: I and Q values of the 18 tones. 64 bits data.
- line 37: POSIX time, to have a time-tagging. Also known as Unix time or Epoch time, is a system for tracking time that represents the number of

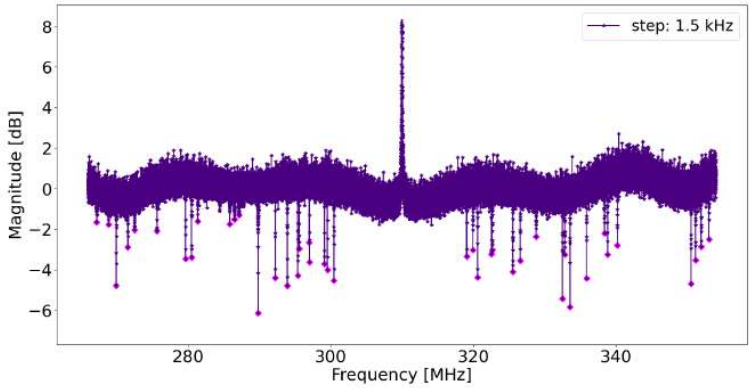

Figure 4.8: Calibrated signal. The resonant tones found are in fuchsia.

seconds (or milliseconds or microseconds for higher precision) that have elapsed since the Unix Epoch, which is defined as 00:00:00 UTC on January 1, 1970 (excluding leap seconds). POSIX time is a single integer value that increases monotonically over time.

- line 38: sampling rate - ticks. Ticks are the numbers of a 40 MHz clock pulsations used to evaluate the sampling rate of this readout electronics. Each tick corresponds to 25 nanoseconds. The sampling rate is evaluated as: $1/(\text{number of ticks} \cdot 25) \cdot 10^9$.
- line 39: zeros line.
- line 40: end of package in ASCII format.

4.6 FPGA and Host computer

The FPGA, a Kintex 7, is mounted in a PXI FPGA Module, NI 5782.
The NI 5782 is an analog dual-input, dual-output, intermediate-frequency (IF) transceiver adapter module designed to work with the NI FlexRIO FPGA module.
The NI 5782 features two analog input (AI) channels with 14-bit sample rates of up to 250 MS/s. The AI channels have SNR of about 70 dB. The NI 5782 also has two analog output (AO) channels with 16-bit sample rates of up to 500 MS/s when using both AO channels. The connectors are SMA type, and the input impedance per connector is 50 Ω.
The ADC part number is ADS62P491[†], a dual ADC with 14-bit resolution.
While the DAC part number is DAC5682Z [‡], a dual DAC with 16-bit resolution.

[†] https://www.ti.com/product/ADS62P49
[‡] https://www.ti.com/product/DAC5682Z

This module allows to implement COSMO firmware and software in a LabVIEW environment, facilitating the process. The host computer used is a DELL Precision 3930 Rack Workstation, core i9.
The host computer is used to control the readout electronics.

4.6.1 COSMO Graphical User Interface

The LabVIEW VI, *Cosmo main*, can be used by the user as a Graphical User Interface (GUI), a screen in figure 4.9.
Here a detailed list of the *COSMO main* functionalities:

- choose between performing the resonant tones search or sending the comb:
  - once the resonant tones search modality is selected, the user must specify and fix the start, stop and step frequency. Then it should be performed the *warm* baseline, which in principle, when nothing changes (i.e. the LO frequency, the cables, the filters) should not be repeated.
    The *warm* baseline is saved as: “warm_YY_MM_DD-h_m_s.txt".
    The same applies to the *cold*-search for resonances.
    Cold data are saved as: “cold_YY_MM_DD-h_m_s.txt". The normalization procedure having both cold and warm signal was descried in section 4.3 and in section 4.4.
  - On the contrary, when the comb signal is selected, the sent frequencies can be chosen from the default ones, manually inserted by the user, or the ones found after the calibration process saved in a LUT.
- Monitor the sent comb signal in real time.
- Monitor in real time the received comb signal.
- Select the attenuation level of the NI-5695 attenuator at a specific central frequency.
- Save data: data can be saved in binary files using either big-endian or little-endian formats. Additionally, the users can specify the duration of the file in terms of time and choose to split it into equal length files.
- Stop processes.

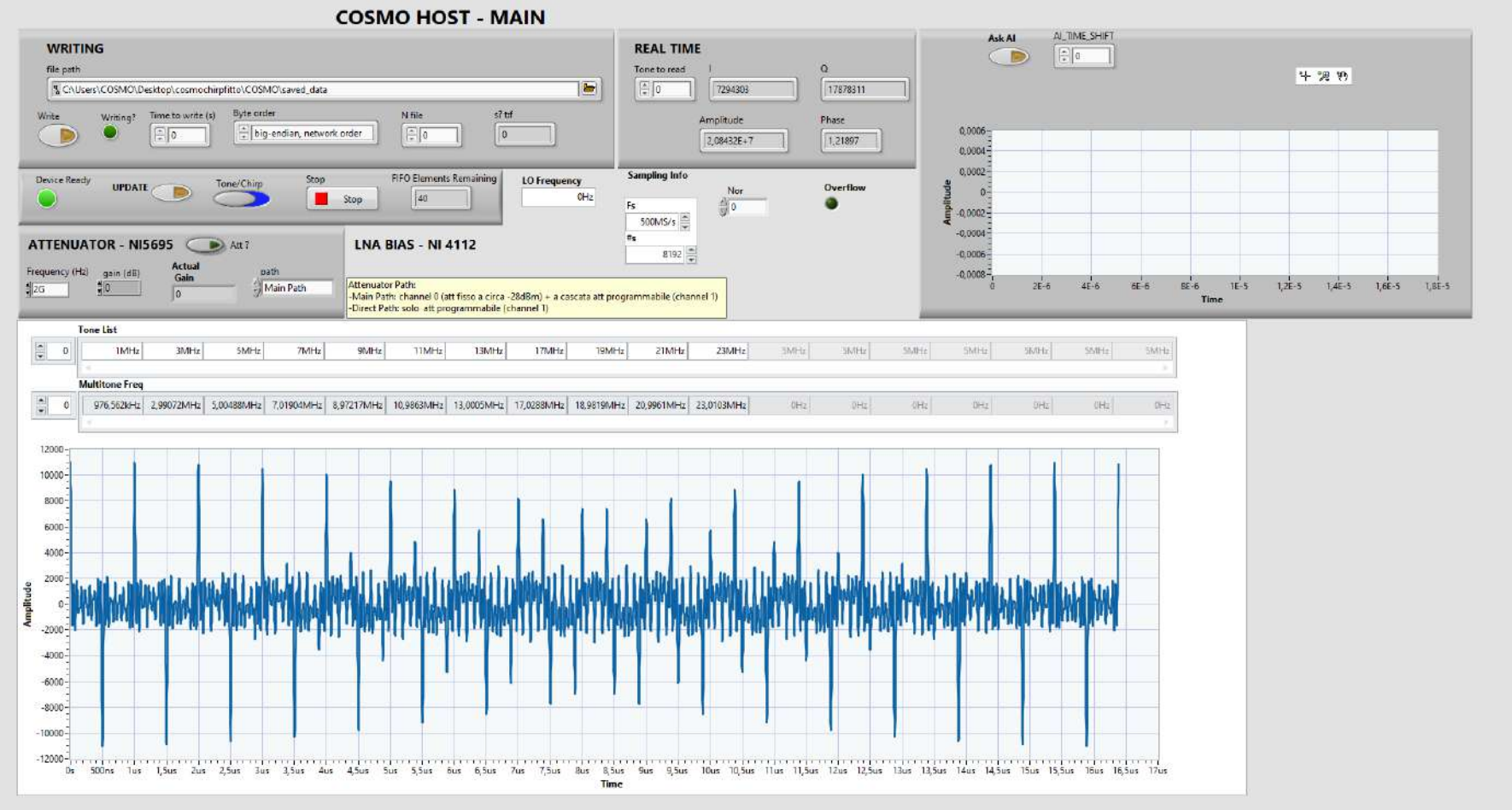

Figure 4.9: COSMO GUI developed by me in LabVIEW.

4.6.2 FPGA utilization

The COSMO firmware, able to generate, detect and find up to 18 tones, has the following device utilization:

- Total slices: 36.4 %. Slices are the fundamental units of FPGA architecture, consisting of several components such as LUTs, flip-flops, multiplexers, and other logic elements.
- Registers: 13.2 %. Registers in FPGA are flip-flops used to store binary state information, often part of sequential logic circuits, and they are used to implement state machines, counters, and shift registers.
- LUTs: 23.2 %. LUTs are configurable logic blocks that implement combinational logic functions. Each LUT can be programmed to produce any output based on its inputs.
- Block RAMs: 21.5 %. Block RAMs (BRAMs) are dedicated memory blocks within the FPGA, used for storing larger amounts of data compared to distributed RAM (which uses LUTs). BRAMs are essential for applications requiring substantial data storage like buffers, caches, and large lookup tables, and they can be configured in various modes (single-port, dual-port, etc.).
- DSP48s: 4.7 %. DSP48 blocks are specialized units designed for high-speed arithmetic operations, improving overall performances.

Since each tone has its dedicated *tone detector*, the architecture can be easily scalable by adding other *tone detector*s.
The most relevant limitation is given by the fact that the multiplicative factors must be saved in memories inside the FPGA. Moreover, lowering the sampling rate (i.e passing from about 60 kHz to about 30 kHz) increases the frequency resolution by the same factor but requires saving more multiplicative parameters. The multiplicative parameters are saved in Block RAMs, whose utilization was only 21.5 %, thus it could be easily possible to reach a sampling rate 4 times slower.

4.7 Investigate the minimum input power to the NI-5782 transceiver

The NI-5782 transceiver's maximum input power is 10 dBm, according to its specifications. However, the minimum input power requires further analysis.
The adopted strategy is based on the capacity of the COSMO readout electronics to detect a signal variation without adding a significant level of noise.
To achieve this, I decided to use the signal generated by the CORDIC strategy,

as described in 4.4, in configuration *warm loop*. This allows monitoring the entire base-band.
The entire bandwidth is monitored from -44 MHz to +44 MHz with a 100 kHz step, with progressively higher levels of attenuation. The attenuation is obtained by using the variable attenuator (channel 1) of the NI PXI-5695, described and characterized in 5.6.
The results are plotted in figure 4.10. As it is shown, the minimum input power should be not lower then approximately -40 dBm, since after this value the signal becomes to be very noisy. This means that a LNA is required to have enough power back in the FPGA.

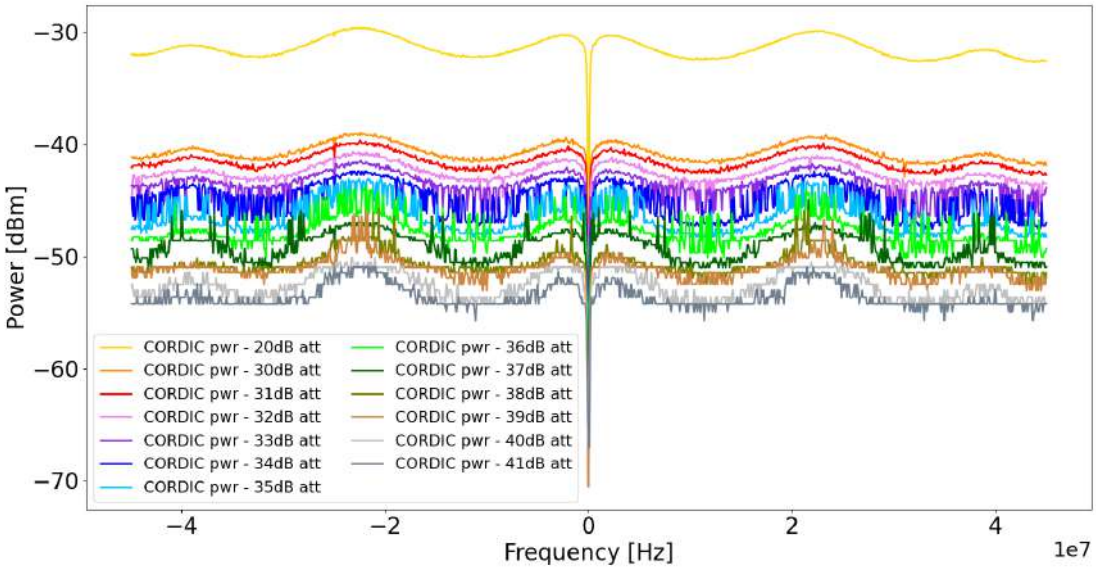

Figure 4.10: Power as function of the base-band frequency, with different levels of attenuation. The legend is intended to be read as: power exiting from the signal generated with the CORDIC strategy minus the attenuation commanded to the NI PXI-5695 variable attenuator.

Chapter 5

Readout electronics

This chapter focuses on presenting each component of the readout electronics, including a comprehensive characterization of them. A picture is in figure 5.1. In this phase, the goal is to thoroughly examine and document the features and performance of individual elements. The primary objective is to validate their performance in accordance with the specifications provided in the datasheets. Each component is represented in the schematic in figure 2.11, composing the full readout chain.
The measurements were performed with a signal analyzer, Anritsu MS2830 [*], a VNA Keysight N5245B [†], and a power meter HP 438A [‡].

5.1 Local Oscillator Valon 5009

5.1.1 Datasheet specifications

The selected Local Oscillator (LO) is the Valon 5009[§]. This module operates on a PLL-synthesized RF signal source programmable within the range 23.5 MHz ÷ 6 GHz, and it features variable output power level control, allowing adjustments from approximately -15 dBm to +15 dBm in 0.5 dB steps.
It has two output sources, both sharing an internal Temperature-Compensated Crystal Oscillator (TCXO) as reference or, alternatively, they can be locked to an external frequency reference. In COSMO setup, I implement the latter by utilizing an external GPS (see section 5.2) driving a Cesium LO. This configuration ensures exceptional stability in the LO's output frequency, a topic that will be elaborated upon in a subsequent detailed analysis. The synthesizers within the Valon 5009 are integrated Voltage-Controlled Oscillator/Phase-Locked Loop (VCO/PLL) integrated circuits. The VCO fundamental frequency spans from

[*] https://www.anritsu.com/en-us/test-measurement/products/ms2830a
[†] https://www.keysight.com/us/en/product/N5245B/pna-x-microwave-network-analyzer-900-hz-10-mhz-50-ghz.html
[‡] https://www.sglabs.it/public/SgLabs_HP20438A.pdf
[§] https://www.valonrf.com/frequency-synthesizer-6ghz.html

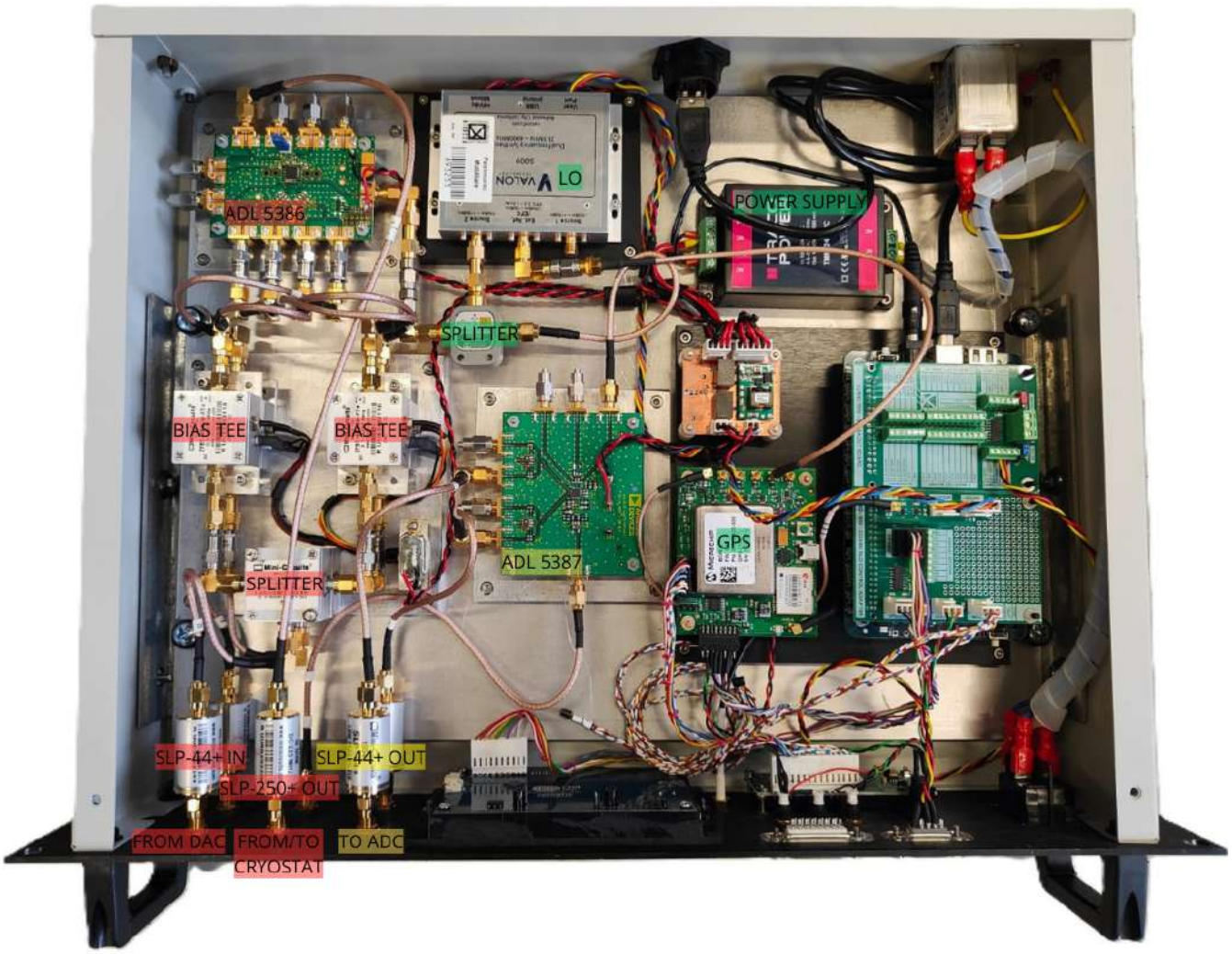

Figure 5.1: Readout electronics picture: modular components. The color code is the same as described in figure 2.11: red labels are for signal-in components, yellow for signal-out ones of the readout electronics.

3000 MHz to 6000 MHz, and lower frequencies are derived through cascaded digital dividers. Due to the digital nature of these dividers, the output frequency does not exhibit a pure sine wave and instead has an harmonic content. Indeed, it produces a clipped sine wave as its output waveform and harmonics are typically at -12 dBc, with odd harmonics being more pronounced. To mitigate this there are filters in our readout electronics.
Temperature stability needs to be taken into account, and as per the datasheet, the Valon 5009 demonstrates a remarkable stability of ±0.5 ppm between -20°C and +70° C. To verify this, I conducted thorough assessments of temperature variations and their impact on the LO performance, with a thermometer attached to the LO. This analysis is in the following sub-paragraph.
Power connections for the LO are established through a DC power supply. The optimal input voltage for peak performance is specified as 6 V at approximately 600 mA maximum. Given our utilization of a single source, a lower current is absorbed.
Before performing the LO characterization, I developed a Python class to command and control the Valon 5009 autonomously. This not only streamlines the process but also circumvents potential limitations associated with the manufacturer's software, working only in Windows.
The communication interface for the Valon 5009 involves both the USB port and a 3.3 V TTL serial interface at the user port. A default baud rate of 115200 is established for communication. Through the developed Python class, a range of functionalities is accessible: it is possible to set the source number, to set and get the frequency, to set and get the level of attenuation with respect to the output power at a certain frequency and other additional features (i.e performing a sweep in frequency).
The typical output power is approximately +15 dBm within the frequency range of 100 to 4000 MHz, aligning with our designated range of interest.

5.1.2 Characterization analysis

It is necessary to assess both frequency and output power stability of the LO. Indeed, the requirements for power going to the modulator and demodulator are less stringent, as dictated by the specifications in their respective datasheets, as reported upon in their sections below. Conversely, maintaining precise frequency stability over time is of enormous importance, as any frequency shift induced by the LO impacts the performance of the readout electronics.
For the measurement of both power and frequency the signal exiting from the source number 2 (we use only one source, and I select the number 2 for practical disposition reasons) is splitted, allowing simultaneous collection of the signal by both a power meter and a frequency meter. To monitor temperature variations, a thermometer is attached to the LO.
After having verified the almost perfectly linearity of the internal attenuation of the LO, I decided not to attenuate the power for characterization purpose and to perform the testes exiting at 200 MHz. The choice of using this frequency

(200 MHz) aligns with the requirements to feed the modulator and demodulator using double of the required frequency (100 MHZ in the configuration of the COSMO KIDs) - according to modulator and demodulator datasheet.
Data are saved in ASCII files, divided in four columns: time, temperature, power (in dBm) and Δ frequency ($\Delta f = f_{out} - f_{nominal}$, in Hz). Over a span of approximately three days, data are collected in two distinct configurations: LO governed by the external reference from the GPS clock and without it.

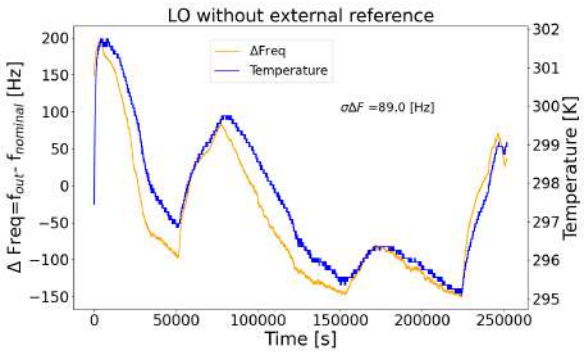

Figure 5.2: LO Δ frequency without external reference (in orange) and temperature variations (in blue).

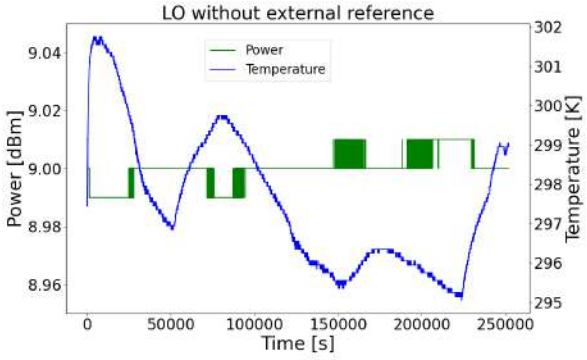

Figure 5.3: LO power without external reference (in green) and temperature variations (in blue).

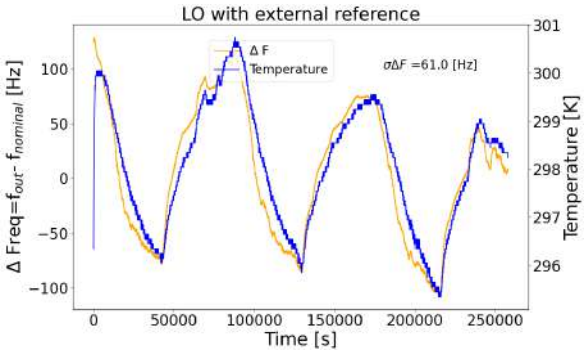

Figure 5.4: LO Δ frequency with the GPS external reference (in orange) and temperature variations (in blue).

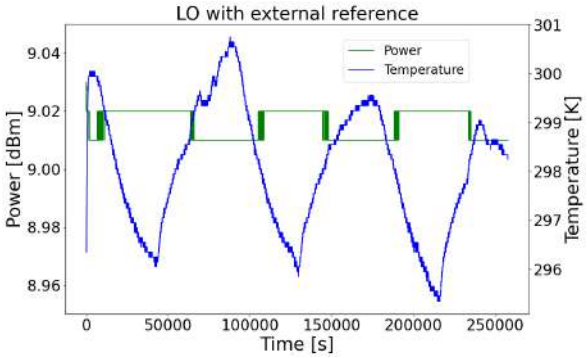

Figure 5.5: LO power with the GPS external reference (in green) and temperature variations (in blue).

Figure 5.2 and figure 5.4 illustrate that, following the initial rise in temperature, frequency variation correlates with temperature changes. On the contrary, as shown in figure 5.3 and figure 5.5, there is no temperature dependence on power. Temperature fluctuation were noted and attributed to the day-night cycle in the laboratory.
A noteworthy outcome is observed when the Cesium LO of the GPS is used: the standard deviation of the frequency reduces to approximately 60 Hz, compared to around 90 Hz when the GPS is not engaged. This underscores the significant impact of the external reference on enhancing frequency stability.

Stabilization of the LO frequency over time (and across temperature variations) is particular important as the LO modulate (and demodulate) the signal, defining the desired RF band. The fluctuation in the frequency of the RF test signal due to a fluctuation in the frequency of the LO could lead to a false signal reading. In fact a different frequency will be excited, corresponding to a different phase of the resonance.
According to this test, the maximum frequency shift caused by the instability of LO is approximately 100 Hz. Considering a KID with a resonance frequency of f_0=100 MHz, and a $Q-$factor of 10000, the KID's resonance bandwidth Δf is: $\Delta f = \frac{f_0}{Q} = 10$ kHz.
So the oscillator's frequency drift would now be at most 1% of the KID's bandwidth.
This problem could be mitigated using higher frequency KIDs while it is still more impacting with higher $Q-$factor.
However, considering that LO frequency instabilities are due to the temperature of the device, what truly matters is ensuring that the temperature remains as stable as possible.

5.2 GPS

5.2.1 Datasheet specifications

The GPS-2700, featuring the Chip-Scale Atomic Clock (CSAC), is a breakthrough technology that allows the presence of performative Cesium Vapor Cell Atomic Reference Oscillator, with fewer than 2 minutes warm-up to be fully operational. The CSAC oscillator provides a very high frequency accuracy, long-term stability, fast lock with low power consumption, and four output channels at 10 MHz.
The GPS-2700 also includes a high-performance time interval counter that can measure the internally generated 1 PPS signal from the GNSS (Global Navigation Satellite System,) receiver or an externally supplied 1 PPS reference signal with a resolution of 20 picoseconds.
The GPS-2700 can be commanded and controlled by RS-232 and USB serial links, with a power supply operating from 8 V up to 36 V.
For the COSMO readout electronics this GPS has multiple functions:

- master clock of the entire readout electronics
- external reference to the LO in order to maintain a much more stable exiting frequency
- assign a timestamp to each package of data acquired with microsecond precision (as reported in 4.5). This is fundamental for accurately tracking the pointing direction of the telescope, and for debugging purposes.

5.3 Modulator and Demodulator

5.3.1 Datasheet specifications: modulator ADL5386

ADL5386 is a quadrature modulator designed for operation across a broad frequency spectrum, ranging from 50 MHz to 2200 MHz.
The ADL5386 takes signals from two differential baseband inputs and modulates them onto two carriers in quadrature with each other. The two internal carriers are derived from a single-ended, external LO input signal at twice the frequency as the desired output. The output amplifier is designed to drive a 50 Ω load.
It operates off a single supply in the range between 4.75 V to 5.5 V.
The operation temperature is between -40° C and +85° C.
The main interesting specifications relevant for the COSMO readout electronics, both in terms of required frequency and power, and in terms of noise, are:

- external LO frequency at twice the required frequency because of an internal divider
- LO input power level at around -7 dBm
- 1 dB output compression: 11 dBm @ 200 MHz
- Noise floor: -160 dBm/Hz @ 200 MHz
- Sideband suppression: -50 dBc @ 200 MHz

Moreover, it is very important to have high sideband suppression so that the unused sideband remains in the background noise (this was verified); otherwise, there would be the possibility of exciting the KIDs at both frequencies.

5.3.2 Datasheet specifications: demodulator ADL5387

The ADL5387 is a broadband quadrature demodulator, ranging from 30 MHz to 2000 MHz.
It operates off a single supply in the range between 4.75 V to 5.25 V.
The operation temperature is between -40° C and +85° C.
The main interesting specifications relevant for the COSMO readout electronics, both in terms of required frequency and power, and in terms of accuracy and bandwidth, are:

- external LO frequency is twice output frequency
- LO input power level range: -6 dBm, +6 dBm
- Demodulation bandwidth: 240 MHz
- Quadrature demodulation accuracy: Phase accuracy 0.4° (0.07 rad), amplitude balance 0.05 dB

5.3.3 Characterization analysis

As for the LO, the modulator has been tested in both the frequency ranges: from 80 to 120 MHz (for the COSMO KIDs) and from 1.89 to 2* GHz (for our KIDs). Tests were done both checking the output frequency and power. Tests where firstly performed in the COSMO bandwidth.
Firstly, it was verified that the modulator's output frequency matches the theoretical expectation, as follows:

$$f_{\text{mod}} = f_{\text{LO}} \pm f_{\text{input}} \tag{5.1}$$

Given that the modulator needs to be fed at double the required frequency, the LO was placed at 200 MHz.
Spanning a range of frequencies from 80 to 120 MHz, the signal was generated using both a waveform generator and than also the readout electronics. This approach aimed to test the readout electronics and compare the generated signals for any discrepancies. The output signal of the modulator was then saved using a signal analyzer.
The results of the modulator performances in terms of frequency are perfectly in accordance with the expectations. In figure 5.6, the measured frequency is plotted as function of the input frequency (the frequency generated by the COSMO readout electronics). The signal is measured with a signal analyzer which sensitivity is taken as uncertainty for the frequency reading. However, to be visible, the error bars are multiplied by a factor of 100. The data perfectly matches expectations, forming a linear function: $y = mx + q$, where m =0.99998 ± 0.00005, and q= -0.00003 ± 0.001, with $\tilde{\chi}$= 0.01.
A similar figure (not reported since it is not significant) is obtained using the signal generated by the waveform generator as the input frequency, further demonstrating the quality of the COSMO readout electronics. Similarly was also saved the output signal of the demodulator, in order to check that:

$$f_{\text{dem}} = |f_{\text{input}} - f_{\text{LO}}| \tag{5.2}$$

It was checked that the both I and Q yield exactly the same results (both in power and frequency), and then a similar analysis to the one performed with the modulator was conducted.
Results matches the expectations, the linear function $y = mx + q$, where m =0.99997 ± 0.00008, and q= -0.0002 ± 0.001, with $\tilde{\chi}$= 0.001.
The power levels were also investigated. Indeed, the power level exiting from the readout electronics is very important to know, as the correct level of attenuation must be applied before entering the cryostat and exciting the KIDs. All the power levels need to be satisfied, such as the modulator requires an input power of approximately -7 dBm, which has to be commanded in the LO.
The results are the following:

*Since the demodulator can work only up to 2 GHz, I decided to test both modulator and demodulator in the same frequency range

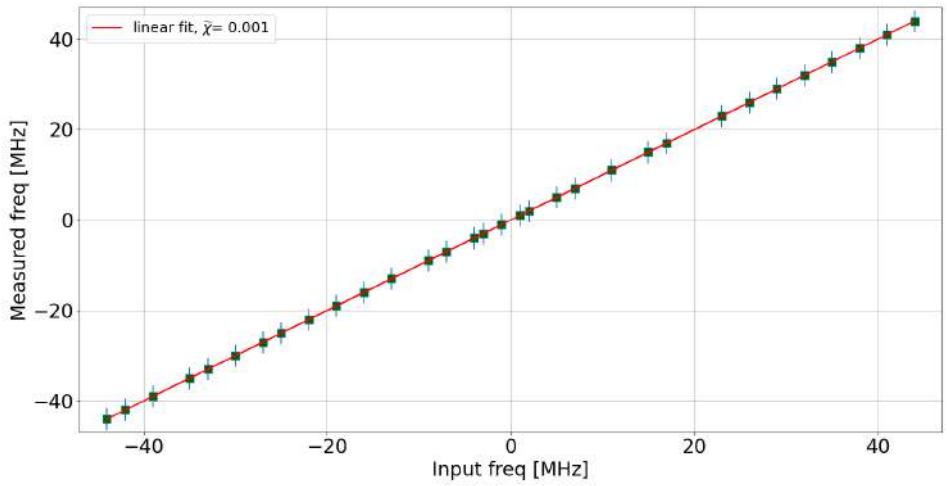

Figure 5.6: Measured frequency (by the signal analyzer) as a function of the input frequency (generated by the COSMO readout electronics). The error bar are multiplied by a factor of 100 to be visible. Data are fitted with a linear function: $y = mx + q$, where m =0.99998 ± 0.00005, and q= -0.00003 ± 0.001, with $\tilde{\chi}$= 0.001.

- the power level of the tones generated by the COSMO readout electronics is -30 dBm±0.5 dBm
- the LO power visible in the band is approximately -58.0±0.5 dBm
- the power level of the signal exiting from the modulator is approximately -27.0±0.5 dBm, up to -29.5±0.5 dBm at the maximum frequency, 2 GHz.

These measurements taking into account the cables' attenuation.
The LO power, even if significantly attenuated with respect to the comb power, is not negligible and is visible over the noise. For this reason, tones around the LO (approximately within an interval of 500 kHz) should not be sent since they could be attenuated (as visible, for example in figure 4.2).

5.4 Other RF components

Other RF components and their specifications are:

- Bias Tee model ZFBT-4R2GW-FT+[†]
  - frequency range: 0.1 to 4200 MHz
  - typical insertion loss: 0.6 dB
  - maximum input current: 500 mA

[†] https://www.minicircuits.com/pdfs/ZFBT-4R2GW-FT+.pdf

  - operating temperature range: -55° C to 100° C

- Power Splitter/Combiner model ZFSCJ-2-1+[‡]
  - frequency range: 0.1 to 500 MHz
  - typical total loss: (= Insertion Loss + 3dB splitter theoretical loss) 4 dB
  - typical isolation: 30 dB
  - typical amplitude unbalance: 0.1 dB
  - typical phase unbalance: 1 deg
  - maximum power input (as a splitter): 1 W
  - operating temperature range: -55° C to 100° C

- Power divider, model 11636B[§]
  - frequency range: DC to 26.5 GHz
  - symmetrical 6 dB power division
  - operating temperature range: -45° C to 70° C

The hybrid splitters and the bias tees are essential for appropriately conditioning the signal to the modulator. Indeed, as reported in 5.3, the modulator requires four inputs, each DC-biased by 0.5 V. Two of these inputs are relative to the I signal and its 180° phase shifted copy, while the other two are relative to the Q signal and its 180° phase shifted copy.
Power divider ensures that both the modulator and demodulator receive identical signals, necessitating them to be fed with the same phase of the LO.

5.5 Filters

As illustrated in figure 2.11, the final configuration for the readout electronics incorporates a total of five filters.
Two SLP-44+ filters are located at the transceiver input, and additional two SLP-44+ filters follow the demodulator at the transceiver output, allowing a total bandwidth around 88 MHz[†] (from -44 MHz to +44 MHz). Moreover, either the SLP-250+ (in the COSMO KIDs configuration) or the VLFG-1800+ (in our lab's configuration) is positioned after the modulator, just before entering the cryostat.
The SLP-44+ filters at both the transceiver input and output, along with the SLP-250+ or VLFG-1800+ after the modulator, effectively cut off unwanted harmonics generated by the LO and the modulator/demodulator. This filtering mitigates potential issues arising from harmonics, which can introduce noise in the power spectrum due to their non-negligible power levels.

[‡] https://www.minicircuits.com/pdfs/ZFSCJ-2-1.pdf
[§] https://www.sglabs.it/public/HP20Agilent20Keysight2011636B_D

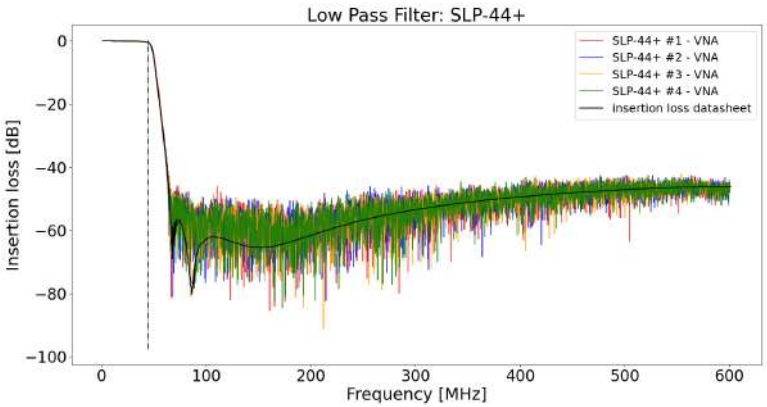

Figure 5.7: Insertion loss: SLP-44+

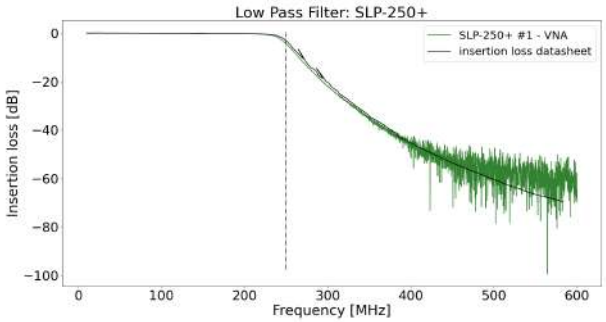

Figure 5.8: Insertion loss: SLP-250+

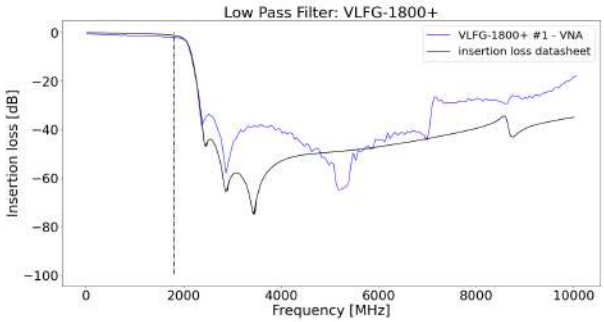

Figure 5.9: Insertion loss: VLFG-1800+

Figures 5.7, 5.8 and 5.9 shows the insertion losses of the three models of filters measured with the VNA and compared to the datasheet expectations.

5.6 Attenuator NI PXI-5695

After the modulator and filter (SLP-250+ for COSMO KIDs configuration, or VLFG-1800+ with our Nb KIDs), the signal may need to be attenuated before entering the cryostat.
In our setup we have the NI PXI-5695 attenuator with specifications in table 5.1. In the COSMO readout electronics, the two channels of attenuation are connected in series, with channel 0 connected to channel 1. However, it is possible to use the programmable attenuator (channel 1) without having the fixed attenuation of channel 0. In this configuration, called *direct* path, channel 0 has a very low attenuation, as reported in figure 5.11.
When higher value of attenuation are required, the attenuator can be used in the so-called *main* path, where the channel 0 has a fixed attenuation, as shown

atasheet_2.pdf

[†]The bandwidth depends on the filter cut off.

Frequency range	50 MHz to 8.0 GHz
Working temperature	0° to 55°
Number of channels	2
Gain Channel 0	Fixed
Gain Channel 1	Programmable

Table 5.1: NI PXI-5695 specifications.

Channel 0: performances	Main path	Direct path
Level calibration accuracy	± 0.7 dB	± 0.7 dB
Maximum input power	+33 dB (10 Vrms, 14 Vpk)	+33 dB (10 Vrms, 14 Vpk)
Relay switch time	5 ms	5 ms
Gain variation by temperature:	$-(4.66 \cdot 10^{-13})$ $\cdot f_{[Hz]}$ in dB/°C	$-(3.09 \cdot 10^{-13})$ $\cdot f_{[Hz]}$ in dB/°C

Table 5.2: Channel 0, fixed attenuator: performances using the attenuator in the main path and in the direct path.

in figure 5.10, in addition to the programmable attenuation of channel 1.
Channel 0 performances are summarized in table 5.2, and the level of attenuation as function of frequency is in figure 5.10 and 5.11.
Channel 1 main performances are summarized in table 5.3 and table 5.4.

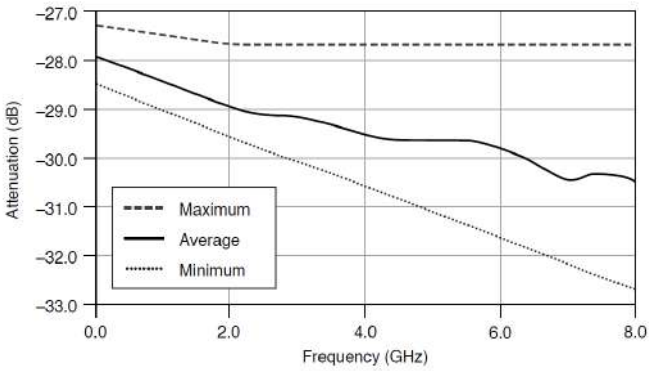

Figure 5.10: Channel 0, fixed attenuator, main path: average measured attenuation.

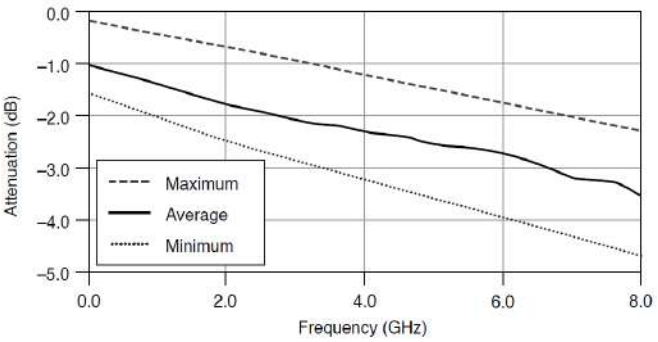

Figure 5.11: Channel 0, fixed attenuator, direct path: average measured attenuation.

A LabVIEW VI is used to control the NI PXI-5695 attenuator. Users can determine the desired path (main or direct), the gain to be applied at a specific central frequency, while also being able to monitor the applied gain as a function of frequency, known as the effective gain.

Channel 1: performances	
Attenuation resolution	± 0.5 dB, typical
Level calibration accuracy	± 0.7 dB
Attenuation settling time	+ 4 μs, maximum
Maximum input power	+27 dBm, maximum (5 Vrms, 7 Vpk)
Gain variation by temperature	-$(2.69 \cdot 10^{-13}) \cdot f_{[\mathrm{Hz}]}$ in dB/°C

Table 5.3: Channel 1: performances

Channel 1 Variable Attenuation Warranted Specification (dB)	10 MHz [dB]	8 GHz [dB]
Minimum Attenuation (Upper Bound)	10.7	13.6
Minimum Attenuation (Lower Bound)	12.3	16.5
Maximum Attenuation (Upper Bound)	41.6	44.3
Maximum Attenuation (Lower Bound)	44.0	47.4

Table 5.4: Channel 1: variable attenuation warranted specification

5.7 Cryogenic Low Noise Amplifier

The signal entering the cryostat is attenuated to prevent altering the superconductive state of the detectors. Additionally, the cryogenic segment of the coaxial cables, in order to guarantee a low heat load, are made by poorly conductive metals and therefore they have a high insertion loss too. As a result, the signal exiting from the KIDs needs to be amplified by a low-noise amplifier (LNA) to achieve the highest signal-to-noise ratio, and also to meet the power level requirement, as discussed in section 4.7.
Thus, a LNA is used which range of frequency is suitable for both the Nb KIDs and the COSMO ones[†]: we chose the model CITLF1 by Cosmic Microwave Technology.
It works between 0.001 GHz up to 5 GHz and it is powered from a single positive DC power supply working between 1.1 and 5 V.
LNA datasheet reports performances at the operative temperature of about 12 K, thus when characterized the LNA performances I tried to keep this temperature, ensuring compliance with the characterization presented in the datasheet.
In particular, during the tests I took into account the following quantities: the return loss given by the S_{11} and S_{22} parameters, the gain (S_{21} parameter) and the noise temperature.
$S-$parameter were measured by the VNA, by setting a range of frequency between 10 MHz (the minimum frequency achieved by the VNA) and 2.5 GHz, with power level at -45 dBm[‡], and varying the LNA voltage bias from 1.1 up to 5 V with 0.1 V step.
Before measuring the LNA S-parameters at around 12 K, I characterized the loss

[†]However, the COSMO final configuration will have another LNA, the ASU LNA#700, operating between 10 MHz and 2 GHz.

[‡]This power level is the maximum one allowed by the input of the LNA.

inside the 4 K cryostat at around 5 K (the minimum achieved temperature with those heat parasitic loads) due to the cables as reported in figure 5.12. Indeed,

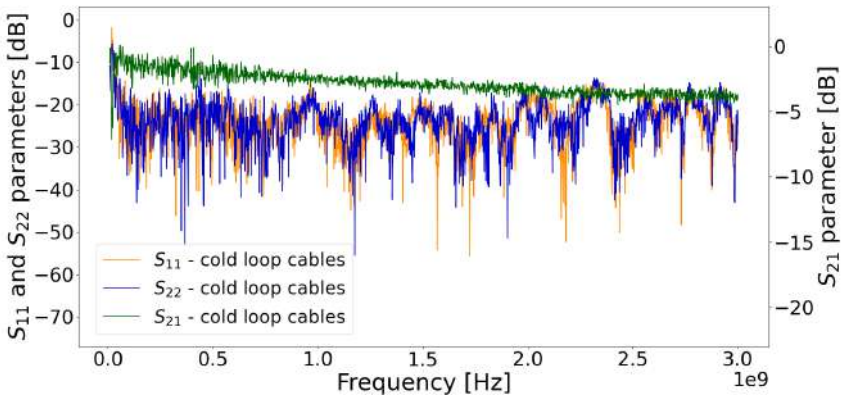

Figure 5.12: Cold loop cables: S_{11} in orange, S_{21} in green, and S_{22} in blue.

following the input signal propagation, there are: a Stainless Steel coax cable anchored to the first stage of the cryocooler (approximately 60 K), a flexible copper cable anchored to the 4 K plate and a superconductive Nb cable. The way back has the same configuration.
Then I placed the LNA inside the cryostat mechanically fixed on a copper plate before the Niobium cable way back, cooled down at a temperature of around 12 K. This temperature was chosen to be compliant with datasheet and it was reached by using some heaters fixed on the sides of the LNA copper plate, while varying the LNA voltage bias (this time I used a range of voltage bias between 1.1 V and 5.0 V with 0.1 resolution).
The LNA gain measured by the VNA was then corrected with the cold loop cables loss and the results are reported in figure 5.13.

The setup to measure the noise temperature when the LNA is cooled down inside the 4 K cryostat is the following, as shown in figure 5.14:

- the LNA is anchored to the 4 K plate. When it is switched on, it is biased at 2.5 V, in order to have a comparison with the datasheet.
- in the LNA input, there is a coaxial stainless steal cable SC-358/50-SS-SS [*] (see table 5.5 for the attenuation levels) with a 50 Ω termination, along with one 47 Ω heater and one thermometer. The termination of the cable is also anchored to the 60 K stage of the cryostat to improve thermalization. In this way, it is possible to monitor the temperature and raise it using the heater.
- LNA output is connected to a Nb cable, then there is a flexible copper cable anchored to the 4 K plate, and a stainless steal coax cable anchored to the 60 K stage before exiting.

[*] http://www.coax.co.jp/en/product/sc/358-50-ss-ss.html

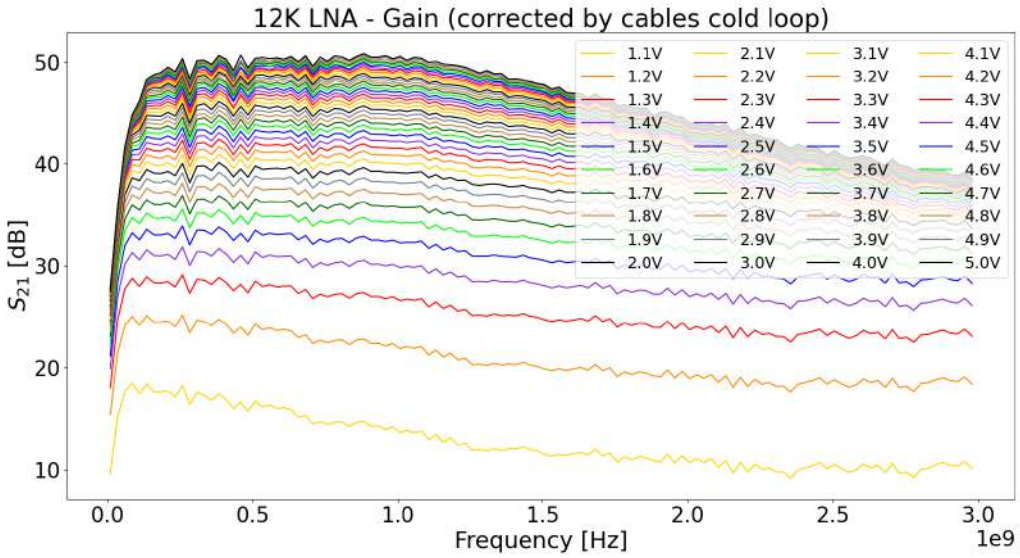

Figure 5.13: LNA gain at 12 K with different voltage bias.

Figure 5.14: LNA setup to measure its noise temperature.

The insertion loss of the cables from outside the cryostat to the LNA was estimated, including the loss of the coaxial stainless steel cable SC-358/50-SS-SS used as the input to the LNA. The procedure was as follows: a first measurement of the *S*-parameters was performed by the VNA cooling down a setup consisting of a stainless steel cable from 300 K to 60 K, a flexible copper cable

Frequency	Att @ 300K	Att @ 4K
0.5 [GHz]	1.7 [dB/m]	1.0 [dB/m]
1.0 [GHz]	2.3 [dB/m]	1.5 [dB/m]
5.0 [GHz]	5.2 [dB/m]	3.3 [dB/m]

Table 5.5: Coaxial stainless steal cable SC-358/50-SS-SS: attenuation values at 300K and 4K for different frequencies.

anchored to the 4 K plate, a Nb cable, and a return path identical to this configuration. Another measurement was performed adding the coaxial stainless steel cable SC-358/50-SS-SS after the Nb cable. By having characterized the line without this cable, it was possible to estimate the loss of the SC-358/50-SS-SS at approximately 7 K (the achieved temperature). The result was checked with the datasheet reported in table 5.5. Doing a linear regression, the expected loss of the datasheet at about 2 GHz is approximately 2 dB/m, and the measured loss at 7 K at a frequency of 2 GHz is about 0.3±0.1 dB for a 10 cm cable.
The attenuation of the SC-358/50-SS-SS is used to estimate the effective temperature in input of the LNA as:

$$T_{\text{effective}} = T_{\text{measured}} \cdot 10^{-\text{cable att}/10} + < T > \left(1 - 10^{-\text{cable att}/10}\right) \tag{5.3}$$

where T_{measured} is the measured temperature at the terminal of the SC-358/50-SS-SS cable, $10^{-\text{cable att}/10}$ accounts for the loss of the cable (in this case $10^{-\text{cable att}/10} = 0.933$, as the attenuation is 0.3 dB), and $< T >$ is the average temperature between the LNA temperature (≃7 K) and the measured temperature at the terminal of the cable (see the first column of the table 5.6).
The LNA output signal is too weak to be collected by the signal analyzer, so it is amplified by a MITEQ AFS4-01000200-05-10P-6* warm amplifier (with a minimum gain of approximately 46 dB, operating between 1 and 2 GHz). This amplified signal is then connected to a Keysight 423B low barrier Schottky diode (LBSD) detector†, which covers a frequency range from 10 MHz up to 26.5 GHz, and converts the input power (which must be lower then approximately -20 dBm) into a voltage, subsequently read by a multimeter.
The results of this test are shown in table 5.6, where the effective input temperature is calculated following equation 5.3. Once calculated the effective temperature in input of the LNA, it is possible to evaluate the noise temperature by equating the amplification law for two different temperatures:

$$\begin{cases} V_{\text{out},1} = G\left(T_{\text{N}} + T_{\text{effective},1}\right) \\ V_{\text{out},2} = G\left(T_{\text{N}} + T_{\text{effective},2}\right) \end{cases} \tag{5.4}$$

where $V_{\text{out},1}$ and $V_{\text{out},2}$ are the output voltage measured by the multimeter, G accounts for the gain of the system, $T_{\text{effective},1}$ and $T_{\text{effective},2}$ are the effective input

*https://nardamiteq.com/docs/AFS4-01000200-05-10P-6.PDF
†https://www.keysight.com/us/en/assets/7018-06773/data-sheets/5952-8299.pdf

T_{measured} @ terminal of cable	Voltage	T_{LNA}	$T_{\text{effective}}$
94.7 ± 0.1 [K]	-14.75 ± 0.01 [mV]	6.8± 0.1 [K]	91.8 ± 0.8 [K]
124.5 ± 0.1 [K]	-18.30 ± 0.01 [mV]	7.0± 0.1 [K]	120.6 ± 0.9 [K]

Table 5.6: Results of the test to characterized the noise temperature of the LNA. The first column shows the temperature measured at the terminal of the SC-358/50-SS-SS cable, the second column provides the voltage measured by the LBSD detector, the third column indicates the LNA temperature, biased at 2.5 V, and the fourth column is for the effective temperature, calculated as in equation 5.3.

temperature as reported in table 5.6, and T_{N} is the noise temperature, the quantity I want to measure.
The final result depends on the frequency only when taking into account the loss of the cable. Thus, the noise temperature of the LNA at approximately 2 GHz (the Nb KIDs' central frequency) is 27.9 K.
This value can be compared with the datasheet, but the result is higher. Indeed, according to the datasheet, when the LNA is cooled down to approximately 12 K, the noise temperature at 2 GHz is 8 K.
In this case, the measurement was performed at around 7K, however, the measured noise temperature is significantly higher, but not relevant on the noise budget.

Chapter 6

Tests Results

This chapter details the tests conducted on the readout electronics connected to the detectors. Specifically, the COSMO readout electronics was tested with Niobium KIDs present in the laboratory at the University of Milano-Bicocca, both in a 4 K cryostat operated by a mechanical cryocooler (SHI RDK-408D2 Gifford-McMahon). Moreover, a test campaign was also performed at the University of Roma La Sapienza with Aluminum KIDs cooled down with a dilution refrigerator.

6.1 General considerations

Electronics readout tests are mainly performed in two configurations, the so-called *warm loop* and the so-called *cold loop*, as already explained in section 4.3.2. Moreover, in the cold loop configuration, when the comb is sent, in addition to the resonant frequencies, a so-called *test tone* is also sent, which has is a frequency signal out of any resonance. The purpose of this tone is to evaluate the noise performances of the readout electronics in a situation where it is possible to neglect, at a first order, the contribution of the KIDs.
As explained in section 4.5, when the comb is sent and received, the parameters saved by the readout electronics are I and Q. From this data, in both configurations (cold and warm loop), the following tasks are performed:

- I-Q plot
- I (and Q) plot as function of time
- magnitude (A) and phase (Φ) as function of time where:

$$A = \sqrt{I^2 + Q^2} \tag{6.1}$$

$$\Phi = \arctan\left(\frac{Q}{I}\right) \tag{6.2}$$

- phase PSD (Power Spectral Density) (see subsection 3.5.1)

6.2 Electronics readout tests at Unimib with 4K cooler

Tests at Unimib were performed in a 4 K cryostat in which the temperature oscillations determine the observed features in the measurements.
The 4 K cryocooler is a SHI RDK-408D2 Gifford-McMahon operating with a water-cooled helium compressors, with a cooling power of 750 mW at 4 K. The refrigeration cycle occurs in an expansion chamber typically referred to as a cold finger, with a frequency of 1 Hz. This cycle is responsible for the small temperature oscillations (approximately 25 mK) in a period of about 1 second inside the cryostat, which we use to change the population of QPs of KIDs. The KIDs inside the cryostat are an array of 25 Niobium KIDs, designed at AstroParticule et Cosmologie Institute in Paris and manufactured at Paris Observatory. The transition temperature of these KIDs is around 9 K and their measured quality factors are higher than 5000 at 4.9 K.
Inside the Unimib-cryostat, the temperature is monitored by the Cryogenic Temperature Controller, CTC100*, which operates four diode sensors (Lake Shore DT-470). The excitation current routed to the temperature sensor, sampled at 10 Hz, produces a voltage across the sensor and calibration curves gives the temperature with millikelvin resolution by means of calibration curves.
Two of the diodes are placed at the two sides of the KIDs array holder, one monitors the LNA temperature (anchored to the first stage of the cryocooler - around 60 K) and the last one is put on one cable anchored to the 4 K plate to monitor the temperature before the KIDs array.
Having characterized the modulator, the power exiting from it is approximately -30 dBm. Therefore, we needed to determine the power required by the KIDs to set the attenuation of the variable attenuator accordingly. Using the Vector Network Analyzer (VNA), I scanned the KIDs' frequency band (1.89 - 2.05 GHz) with various power values to find the optimal input power by analyzing the $|S_{21}|$-parameter of the resonances. An example is reported in figures 6.1,6.2, 6.3, 6.4. In these four figures, the key aspect is the noise level of the signal with respect to the power. Besides, the depth of the resonance is not relevant, as the depth varies with a 1 Hz frequency due to temperature oscillations inside the cryostat, making it difficult for the VNA to capture the minima.
The problem is indeed delicate: insufficient power results in noisy signals and poorly defined resonances, while excessive power can lead to the transition from the superconductive to the non-superconductive regime of the detectors. This transition can occur due to the generation of non-thermal phonons by the dissipated power, which can alter the Cooper pair density.
Thus the input power of the VNA should be approximately -50 dBm. Therefore, the PXI-5695 attenuator is set at -20 dB with a central frequency of 2 GHz.

*https://www.thinksrs.com/products/ctc100.html

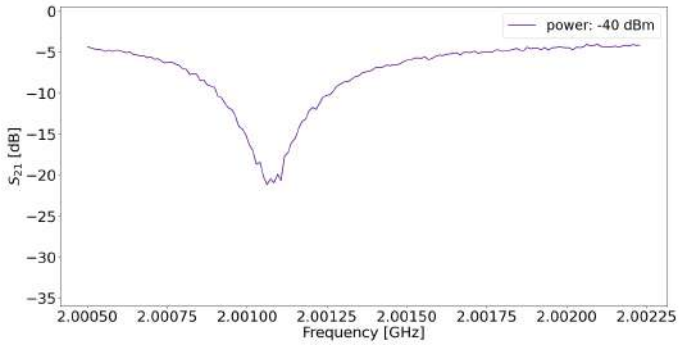

Figure 6.1: $|S_{21}|$-parameter, zoom on a resonance of Nb KIDs in the 4 K cryocooler with temperature $T = 5.5 \pm 0.25$ K. VNA input power: -40dBm.

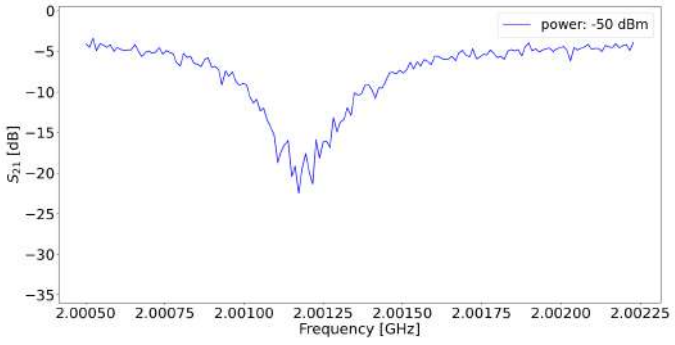

Figure 6.2: $|S_{21}|$-parameter, zoom on a resonance of Nb KIDs in the 4 K cryocooler with temperature $T = 5.5 \pm 0.25$ K. VNA input power: -50dBm.

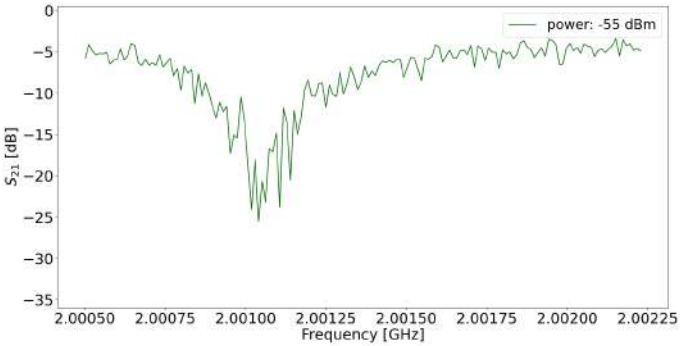

Figure 6.3: $|S_{21}|$-parameter, zoom on a resonance of Nb KIDs in the 4 K cryocooler with temperature $T = 5.5 \pm 0.25$ K. VNA input power: -55dBm.

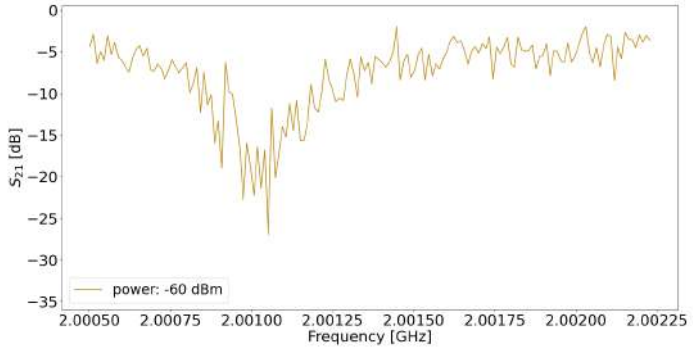

Figure 6.4: $|S_{21}|$-parameter, zoom on a resonance of Nb KIDs in the 4 K cryocooler with temperature $T = 5.5 \pm 0.25$ K. VNA input power: -60dBm.

Regarding the LNA, in this configuration it is anchored to the first stage of the cryostat, at approximately 60 K to prevent it from consuming cooling power required by the KIDs. I also checked that at different bias levels the LNA did not alter the temperature of the 4 K stage. Additionally, the LNA was operated with a bias of approximately 3.0 V, where, according to the datasheet, it should have the lowest noise.

6.2.1 4K cooler: find the resonances

For all the tests conducted with the 4 K cooler, the LO was set at 1.957 GHz, as previously shown in figure 4.5. This frequency was chosen based on several hardware considerations: the demodulator has a maximum operating frequency of 2 GHz (as mentioned in section 5.3.2), and the SLP-44+ filters (section 5.5) limit the bandwidth to at least 88 MHz. Additionally, from a practical perspective, the S_{21} VNA scan of the Nb KIDs shows no resonances around 1.957 GHz.
The first step is to find the resonances using the procedure described in section 4.4. In figure 6.5 the $|S_{21}|$-parameter of Nb KIDs at a temperature of $T = 4.8 \pm 0.25$ K is shown, comparing the results obtained with the VNA to those obtained using the COSMO readout electronics, following the implemented procedure. Some considerations regarding this figure are necessary. First, the VNA

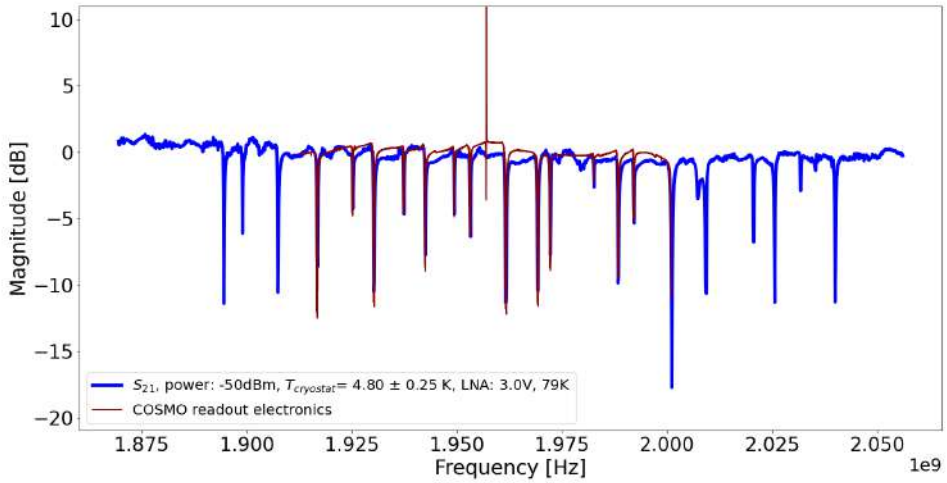

Figure 6.5: $|S_{21}|$-parameter of Nb KIDs at a temperature of $T = 4.8 \pm 0.25$ K is shown. The $|S_{21}|$-parameter obtained using the VNA with an exiting power of -50 dBm, amplified by the LNA, is represented in blue. The signal has been shifted along the y-axis to align with the $|S_{21}|$-parameter obtained using the COSMO readout electronics, shown in purple. This latter signal is obtained following the procedure described in section 4.4. The LNA is anchored at the first stage of the cryostat, reaching a temperature of approximately 79 K, and it is biased at 3.0 V.

signal has been shifted along the y-axis to align with the $|S_{21}|$-parameter ob-

tained using the COSMO readout electronics. This adjustment accounts for the presence of an amplifier's gain.
At the frequency position of the LO, there is a spike towards a positive magnitude. However, this signal is not real but is a result of the calibration procedure described in section 4.3.2.
The most notable point is that the VNA signal should be considered an instantaneous measurement, meaning it cannot track temperature fluctuations, which can cause the resonances to become deeper or shallower over time. In contrast, the $|S_{21}|$- parameter obtained with the COSMO readout electronics is designed to allow for tracking the minima of the monochromatic frequency. This is accomplished by sending the same monochromatic frequency multiple times and capturing the minima in transmission, which also corresponds to the minimum temperature achieved by the cryostat in that specific instant.
For this specific plot, I chose to repeat the measurement 7 times with a frequency step of 10 kHz, covering a bandwidth of 88 MHz.
An interesting consequence of sending the same monochromatic frequency multiple times and capturing the minima is that it allows monitoring of frequency variations due to temperature oscillations. An example is in figure 6.6, obtained with 11 repetitions, and a step frequency of 500 Hz. This should be viewed

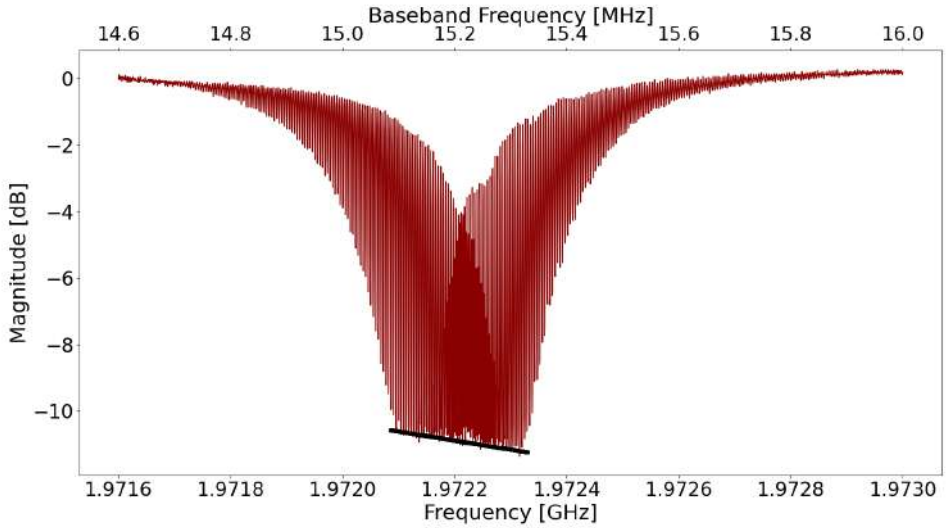

Figure 6.6: $|S_{21}|$-parameter of a resonances of the Nb KIDs array at a temperature of $T = 4.8 \pm 0.25$ K is shown. The top x-axis represents the baseband frequency, while the bottom x-axis shows the actual frequency. The black segment delineates the variation in the minimum frequency of the resonance due to temperature oscillations.

as multiple resonance curves, each corresponding to one of the temperatures within the range of oscillations, all displayed in the same plot. Thus the black segment delineates the variation in the minimum frequency of the resonance due to temperature oscillations.
This procedure is repeated for all frequencies to monitor frequency variations, which helps in selecting the tones that can be sent and acquired for evaluating

amplitude and phase variations using the DDC (as explained in section 4.2.3).

In the following subsections (6.2.2, 6.2.3 and 6.2.4), I provide a report of the most interesting and valuable results of the readout electronics, considering both some resonant tones and test tones in both configurations: the *warm loop* and the *cold loop*.
The chosen resonant tones are centered at about 1.9167 GHz, 1.9424 GHz, 1.9722 GHz, 1.9920 GHz, which appear to be the most interesting ones. It is important to note, particularly for characterizing the readout electronics, that these tones correspond to the tones generated in the baseband respectively at about $1.9167 - 1.957 = -40.3$ MHz, $1.9424 - 1.957 = -14.6$ MHz,$1.9722 - 1.957 = 15.2$ MHz, $1.9920 - 1.957 = 35$ MHz, where 1.957 GHz is the LO frequency.
The term "about" is used for these frequencies because, as observed in figure 6.6, with this cryocooler, it is not possible to pinpoint a single resonant frequency due to temperature oscillations. This results in a range of frequencies for each specific resonance that are generated as part of the comb.
Additionally, as explained in section 4.1, COSMO readout electronics can only generate comb signals (used to evaluate amplitude and phase variation through the DDC) at frequencies that are multiples of the sampling rate, which is approximately 60 kHz. Thus, for example, for the 15.2 MHz (1.9722 GHz) tone the comb frequencies sent are: 15.0757, 15.1367, 15.1978, 15.2588, 15.3198 MHz.
While, for the tones outside the resonances, the chosen test tones are: $1.9579 - 1.957 = 0.9$ MHz and $1.9750 - 1.957 = 18$ MHz. These test frequencies are chosen by examining figure 6.5 and selecting frequencies where no resonances are present, ensuring that the signal is not attenuated by other resonances. The test tones are useful for monitoring the effect of temperature fluctuations, disentangle these effects with respect to the resonances themselves.

6.2.2 4K cooler: I-Q plot

In this section, I present the results and considerations regarding the I-Q plot for all the tones described above in both configurations: the *warm loop* and the *KIDs loop*.
In figure 6.7 and figure 6.8, the IQ plots of two test tones (outside the resonances) are shown, comparing both the *warm loop* (red) and *cold loop* (blue) configurations. As expected, in the *warm loop* configuration, the IQ plot consists only of noise, while in the *cold loop* configuration, the signal is influenced by the cold chain.
In figure 6.9 and figure 6.10, two resonant tones are represented. The result aligns with expectations, as described in section 3.4.2.1: temperature oscillations trace an ellipse in the IQ plane, with each point representing a jump within the circle drawn at a fixed temperature.

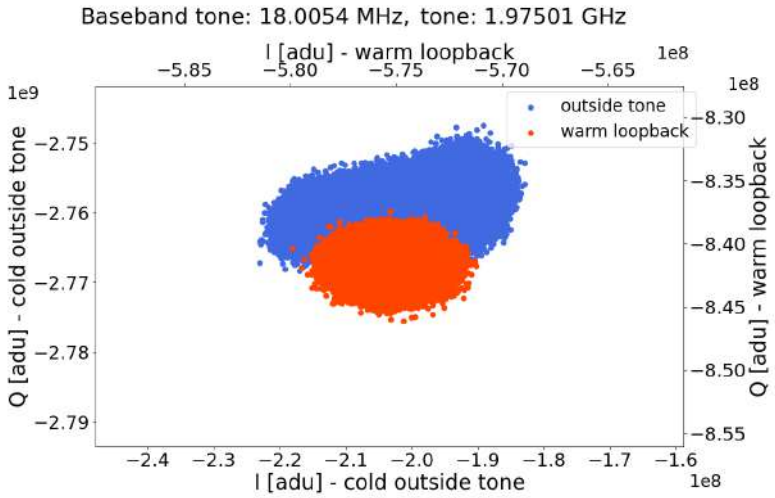

Figure 6.7: IQ plot of the test tone at baseband frequency: 18.0054 MHz. The *warm loop* is in red, and the *cold loop* is in blue.

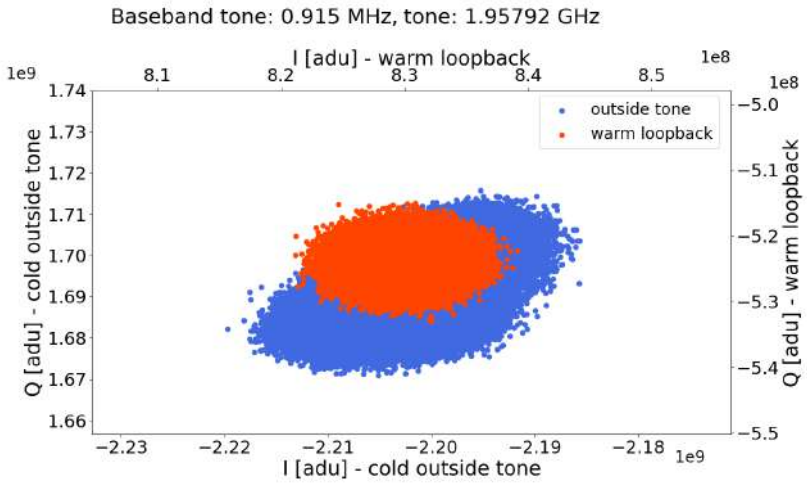

Figure 6.8: IQ plot of the test tone at baseband frequency: 0.915 MHz. The *warm loop* is in red, and the *cold loop* is in blue.

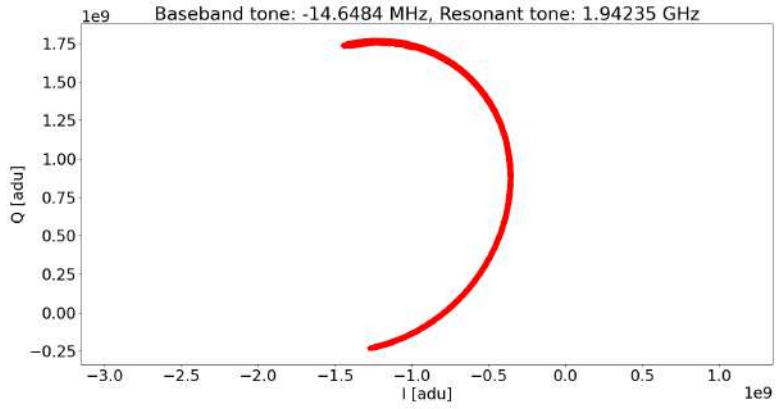

Figure 6.9: IQ plot of a resonant test tone at baseband frequency: -14.6484 MHz.

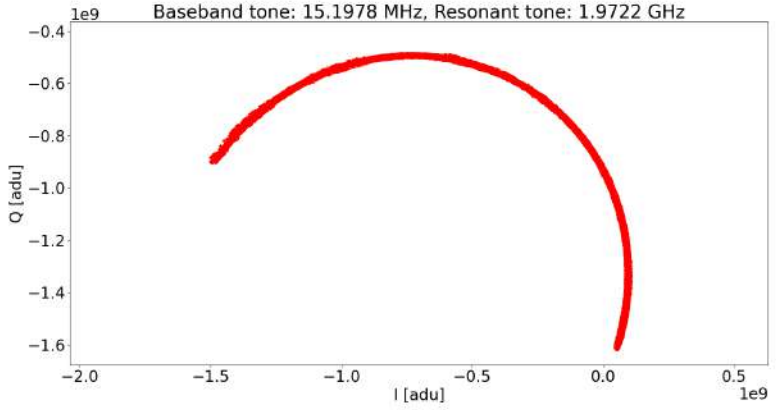

Figure 6.10: IQ plot of a resonant test tone at baseband frequency: 15.1978 MHz.

6.2.3 4K cooler: Magnitude and phase as function of time

In this section, I present the results and considerations regarding the magnitude (A) and phase (Φ) as function of time for representative resonant tone (in figure 6.11) and one test tone (in figure 6.12).
In figure 6.11, it can be observed that both phase and magnitude exhibit an oscillation period of 1 s, which corresponds to the frequency of the cryocooler. This trend is also noticeable outside the resonances, as seen in figure 6.12, where the noise, expected to form a straight line, is oscillating with the same 1-second period. This oscillation is visible thanks to the very high sensitivity of the readout electronics.
Both test tones have a standard deviation in the phase of 0.0027 radians.

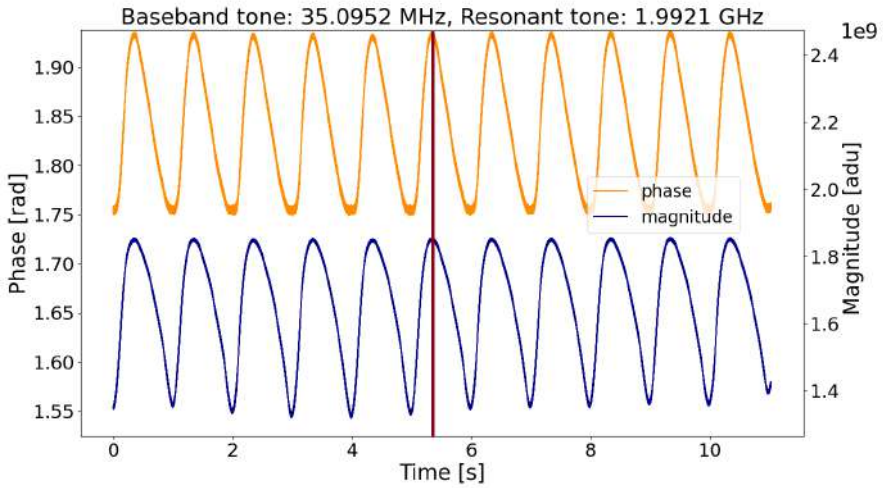

Figure 6.11: Magnitude (blue) and phase (orange) of the resonant tone at a frequency: 35.0952 MHz.

6.2.4 4K cooler: Phase PSD

In this section, I present the results and considerations regarding the PSD (refer to the theory in section 3.5.1) of the phase for all the tones described above, in both configurations: the *warm loop* and the *KIDs loop*.
The PSD analysis is particularly interesting in these configurations, including both test tones and resonant tones, as it helps to characterize the phase noise of the electronics and to differentiate the noise contributed by the KIDs from that introduced by the electronics.
In figure 6.13 and figure 6.14, the PSD of the two test tones is shown. The level of warm white noise (warm loopback) is consistent for both, at approximately $5.0 \cdot 10^{-6}$ rad$/\sqrt{\text{Hz}}$. The cold white noise, however, is $8.01 \cdot 10^{-5}$ rad$/\sqrt{\text{Hz}}$ for the 0.915 MHz tone, and $4.60 \cdot 10^{-5}$ rad$/\sqrt{\text{Hz}}$ for the 18.0054 MHz tone.
For both test tone is it possible to see:

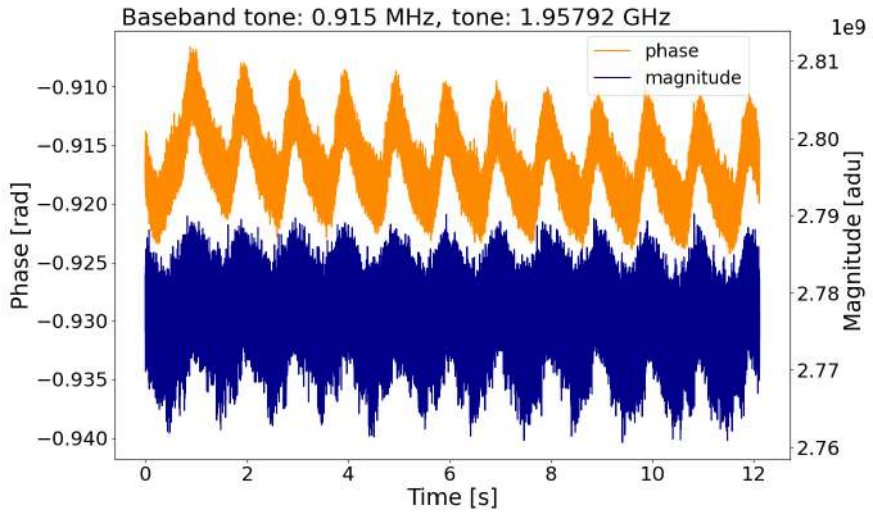

Figure 6.12: Magnitude (blue) and phase (orange) of the test tone at a frequency: 0.915 MHz.

- 1 Hz peak and its harmonics caused by the cryocooler.
- The large peak at approximately 50 Hz and its harmonics is due to the line voltage.

In figure 6.15 and figure 6.16, representing two illustrative case of resonant tones (15.1978 and 35.0342 MHz), the following can be observed:

- 1 Hz peak and its harmonics caused by the cryocooler.
- The large peak at approximately 50 Hz and its harmonics is due to the alternating current electricity at this frequency.
- white noise: $1.88 \cdot 10^{-4}$ rad$/\sqrt{\text{Hz}}$ for the 15.1978 MHz tone; and $1.53 \cdot 10^{-4}$ rad$/\sqrt{\text{Hz}}$ for the 35.0342 MHz tone.

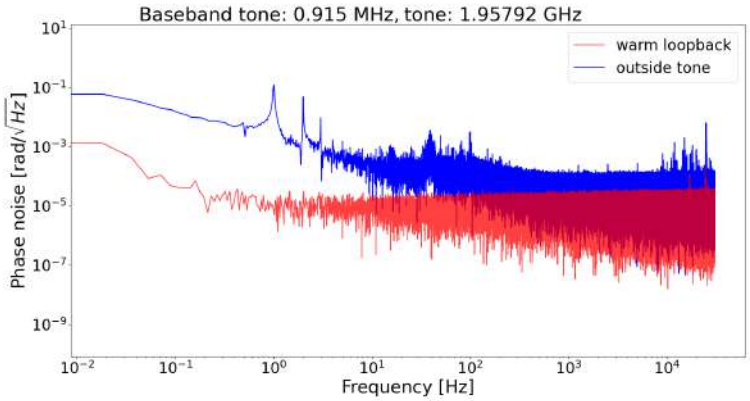

Figure 6.13: PSD of the test tone at frequency: 0.915 MHz. The *warm loop* is in red, and the *cold loop* is in blue.

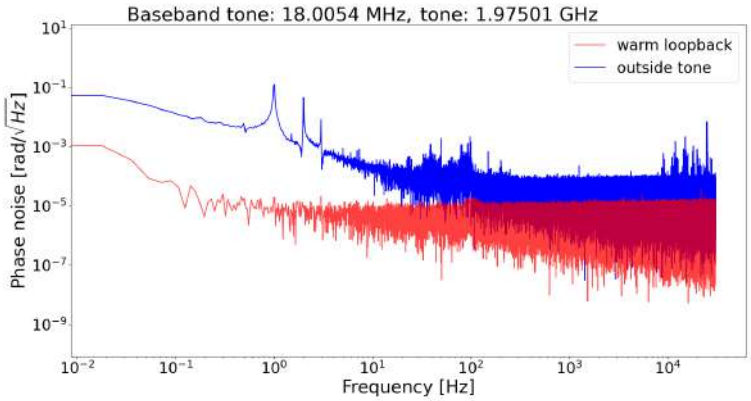

Figure 6.14: PSD of the test tone at frequency: 18.0054 MHz. The *warm loop* is in red, and the *cold loop* is in blue.

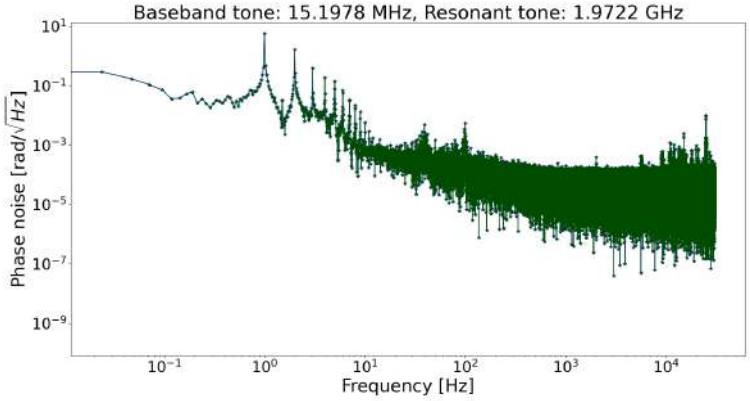

Figure 6.15: PSD of a resonant tone at frequency: 15.1978 MHz.

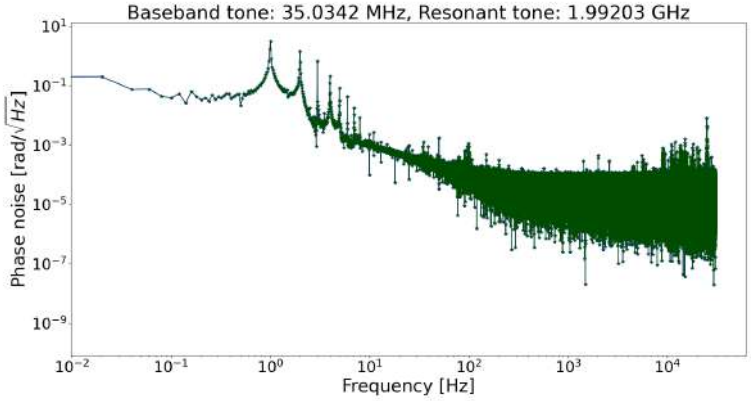

Figure 6.16: PSD of a resonant tone at frequency: 35.0342 MHz.

6.3 Electronics readout tests at Sapienza University

I tested the COSMO readout electronics at Sapienza University (Rome), where a dilution refrigerator hosted an array of Aluminium KIDs (with frequencies between approximately 200 to 400 MHz) cooled down to approximately 150 mK, see the picture in figure 6.17.

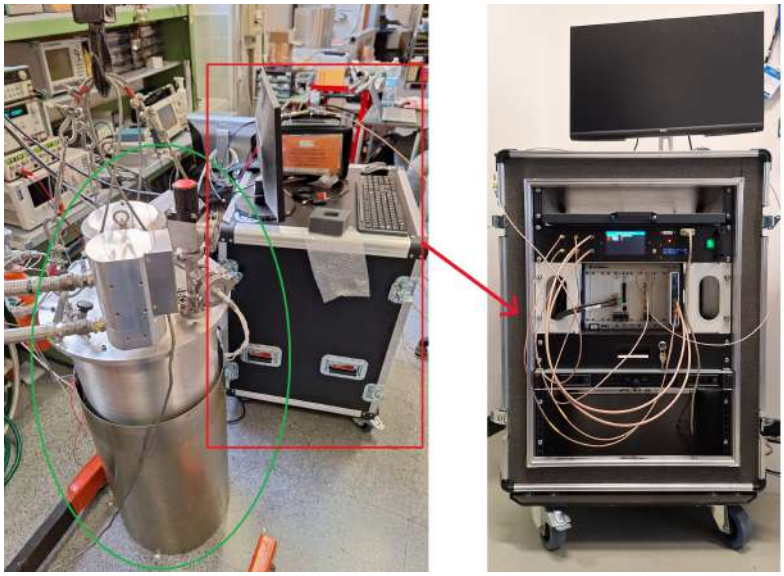

Figure 6.17: Left: COSMO readout electronics (in the red box - zoom in the right part) at Sapienza University in Rome. The readout electronics was tested with an array of Aluminium KIDs cooled down to approximately 150 mK in a dilution refrigerator (encircled in green).

The LO was placed at 310 MHz and a scan of the full bandwidth around it (-45 MHz, +45 MHz) was performed. The result, after the normalization (explained in section 4.4), is in figure 6.18.
Then some resonant tones were selected for a deeper investigation. In particular I analyzed the resonant tone at 319.080 MHz. The resonance amplitude was acquired with frequency step of 50, 150 and 250 Hz, in order to track the signal between 319.06 and 319.11 MHz, repeating each step 10 times to reduce the noise.
Then I also performed the same analysis varying the temperature: 152 mK, 209 mK, 245 mK and 256 mK. The result is shown in figure 6.19, with 150 Hz step.
As shown in figure 6.19, the COSMO readout electronics can accurately trace a resonance and its shape, having a sufficient number of points. However, a fit of the resonances is not performed, as a comparison with the ROACH data reveals a power loss of a few dB.
Once the resonant tone was found, I also sent it in the "comb" configuration (which means in configuration of sending and acquire one or more - up to 18

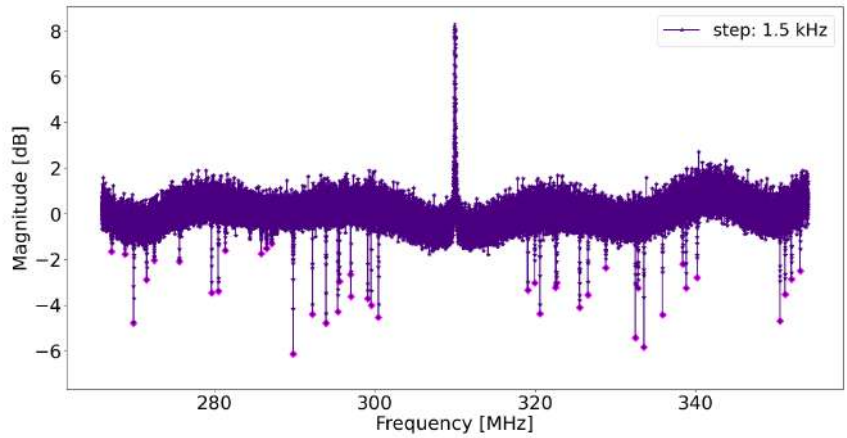

Figure 6.18: Calibrated signal. The resonant tones found are in fuchsia.

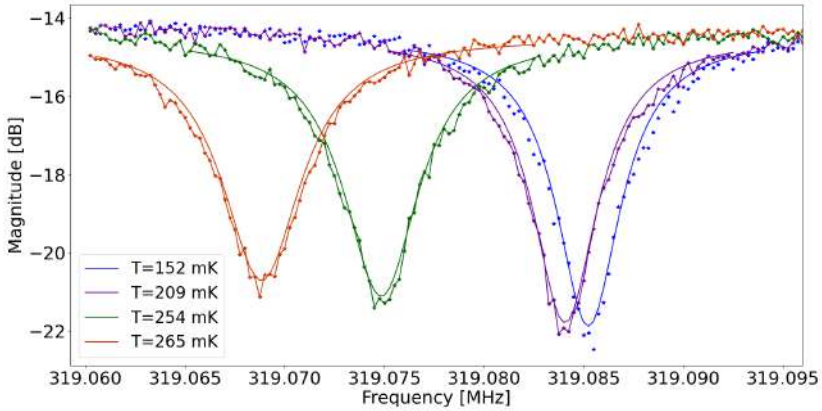

Figure 6.19: Amplitude variation of one selected tone changing the temperature (152 mK, 209 mK,254 mK, 265 mK). 150 Hz frequency step.

- tones doing a DDC). I got 60 seconds of data of I and Q signals, in order to evaluate the phase noise.
I also took 60 seconds of acquisition outside the resonance to monitor the level of phase noise. The result is in figure 6.20, where the tone is plotted in green, a frequency outside the resonance is in blue, and the warm noise is in red. The vertical grey dotted lines represents the interval of white noise evaluation. The results are:

- white noise of a resonant tone: $4.719 \cdot 10^{-4}$ rad$/\sqrt{\text{Hz}}$
- white noise outside a tone (cold loopback): $2.13 \cdot 10^{-5}$ rad$/\sqrt{\text{Hz}}$
- warm white noise (warm loopback): $2.3 \cdot 10^{-6}$ rad$/\sqrt{\text{Hz}}$

Moreover, in figure 6.20, the resonant tone exhibits the typical roll-off expected

due to the generation and recombination of quasiparticles. This demonstrates the high potential utility of this readout electronics, as parameters such as the quasiparticle lifetime can only be studied with electronics capable of achieving a very high sampling rate, which the ROACH system cannot provide.

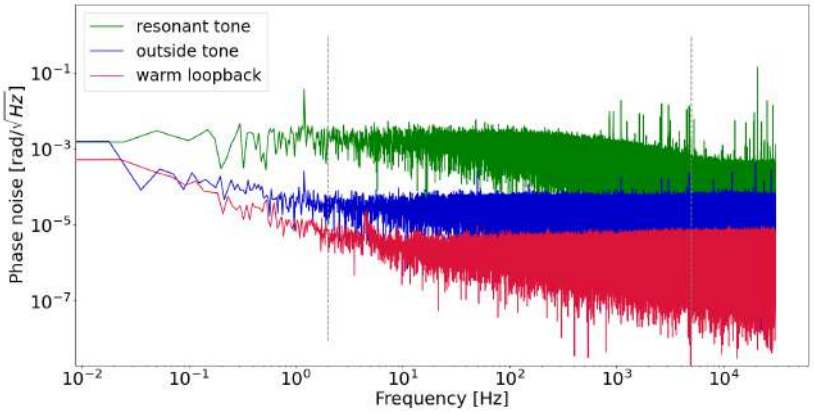

Figure 6.20: Phase noise of a resonant tone (green) compared to phase noise level outside a resonance (blue), and the phase noise in the warm loopback configuration (darkred). The vertical grey dotted lines represents the interval of white noise evaluation.

The COSMO readout electronics performances can be also compared to the one of the Roach2 (`https://www.digicom.org/roach-board.html`) used at Roma Sapienza University, in figure 6.21. Some considerations compar-

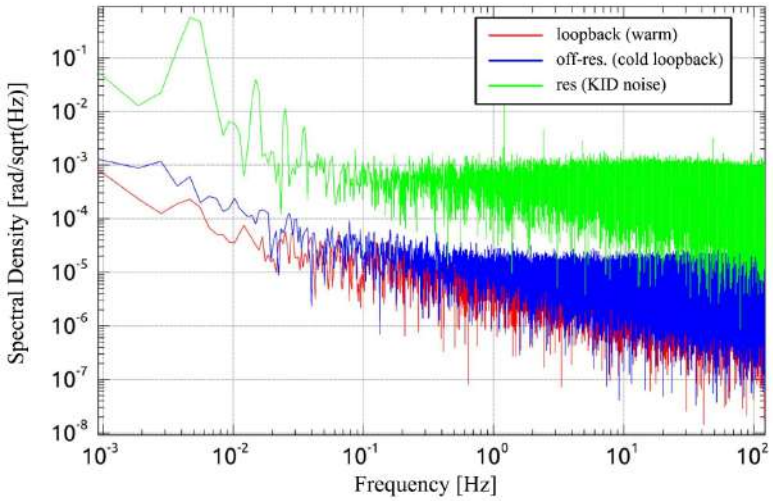

Figure 6.21: Roach2: Phase noise of a resonant tone (green) compared to phase noise level outside a resonance (blue), and the warm loopback (red).

ing the two phase noise in figure 6.20 (our readout electronics performances), and in figure 6.21.

- Our sampling rate is approximately 60 KHz, while the Roach2 sampling rate is approximately 200 Hz. Thus with our readout electronics it is possible to explore higher frequencies.
- Comparing the level of noise, the phase noise in configuration ”resonant tone“ is comparable, while in cold loopback configuration, we get higher value. Instead, warm loopback noise of our readout electronics is lower with respect to the Roach2 one.

Chapter 7

List of other electronics/strategies

In this chapter, the functionality and scientific objectives of other KIDs readout electronic systems will be examined, with a focus on how they operate, their design, and their characteristics in terms of ease of use and limitations.
The analysis will consider how these electronics are constructed and whether their use is straightforward or complex. For example, some systems, such as ROACH (Reconfigurable Open Architecture Computing Hardware), have significant limitations, such as firmware that is neither modifiable nor accessible, which reduces flexibility for specific customizations.
Finally, these solutions will be compared with the COSMO readout electronics described in this thesis, highlighting whether and how our electronic system offers additional functionalities compared to others. This comparison will be crucial in justifying the effort required to develop our own electronics, demonstrating the advantages of greater customization and optimization for our specific research needs.

7.1 OLIMPO

All the information related to the OLIMPO experiment was taken from [64, 65, 66].
OLIMPO (Osservatorio nel Lontano Infrarosso Montato su Pallone Orientabile, Far Infrared Observatory Mounted on a Pointed Balloon) was a 2.6 meter on-axis millimeter-wave Cassegrain telescope mounted on an attitude-controlled stratospheric balloon payload. It flew on July 14th, 2018, in the Circumpolar region at an altitude of 37.8 km.
The OLIMPO experiment was designed to measure the Sunyaev-Zel'dovich (SZ) effect, a CMB anisotropy observed in the direction of galaxy clusters. This effect is caused by the inverse Compton scattering of low-energy CMB photons by the high-energy electrons of the hot gas present in the intracluster medium. SZ effect measurements are a valuable tool for studying the morphological and dynamical state of clusters, probing the CMB temperature evolution with the redshift, constraining cosmological parameters, and identifying previously un-

known clusters through their SZ signature in the microwave sky.
OLIMPO performed a spectroscopic map of the SZ effect with a differential Fourier transform spectrometer (DFTS) with a maximum resolution $\Delta\nu = 1.8$ GHz.
Regarding the OLIMPO scanning strategy, the OLIMPO payload could scan and point at the sky using a custom alt-azimuth mount. Sky scans were obtained by rotating the gondola outer frame and then wobbling the primary mirror in the cross-elevation direction.
OLIMPO was also equipped with a plug-in spectrometer, which could be inserted into the optical path to perform spectral analysis within the four bands of the photometer. The spectrometer employed a double MPI configuration. The telescope was pointed such that one half of the focal plane focused on the cluster to be studied, while the other half focused on a nearby reference region.
OLIMPO was equipped with four arrays of detectors cooled down to approximately 300mK, operating at 150, 250, 350, and 460 GHz with 23, 39, 25 and 43 pixels, respectively.
Two identical readout electronics were used, biasing and reading the 150 and 460 GHz arrays and the 250 and 350 GHz arrays, respectively.
A schematic of the OLIMPO readout electronics is in figure 7.1. OLIMPO FPGA

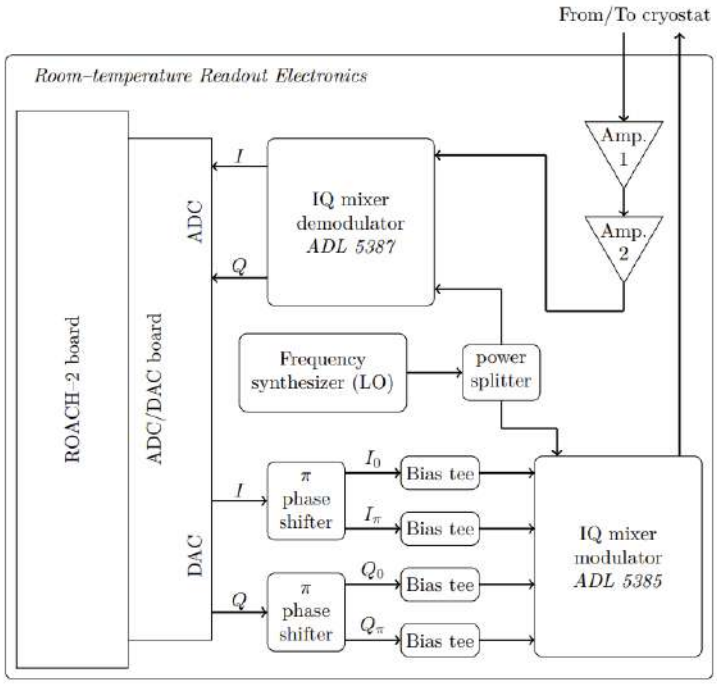

Figure 7.1: OLIMPO readout electronics block diagram. Figure taken in [65]

consists of a ROACH–2 board*, coupled to a MUSIC DAC/ADC board†. The firmware has been developed by ASU (Arizona State University), and is able

*https://casper.berkeley.edu/wiki/ROACH2
†https://casper.berkeley.edu/wiki/MUSIC_Readout_(Kinetic_Inductance_Detector_(KIDs))

to generate up to 1000 tones over a 512 MHz bandwidth, with a demodulated output sampling rate up to about 1 kHz.
The baseband bias signals I and Q output by the DACs are filtered by low pass filters (Mini Circuits SLP-250+), and up-converted by an IQ mixer modulator (Analog Devices ADL 5385). The local oscillator (LO) is a Valon, model 5009. Its signal is split by a power splitter (Mini Circuits ZFRSC-42-S+) and supplies to the modulator cited above and to the demodulator described below. The ADL 5385 IQ mixer modulator requires as input the I and Q signals and their 180° phase shifts (obtained by means of a Mini Circuits ZFSCJ-2-1-S+); all the input signals are offset positive by means of four bias tees (Mini Circuits ZFBT-4R2GW-1-FT+). The upconverted signal output of the modulator is connected to the input line of the cryostat. The signal from the readout line output of the cryostat is amplified by two room temperature amplifiers (Mini Circuits ZX60-P103LN+ and ZX60-3018G+), and input to the IQ mixer demodulator (Analog Devices ADL 5387) to be down-converted to the baseband. These signals are low-passed (via Mini Circuits SLP-250+ filters) and input to the ADCs of the MUSIC board. The signal is processed by the FPGA to measure the amplitude variations of the I ad Q signals transmitted by all the KIDs.
This readout configuration and the RF components are almost the same as the COSMO ones. An example of phase noise is in figure 7.2.

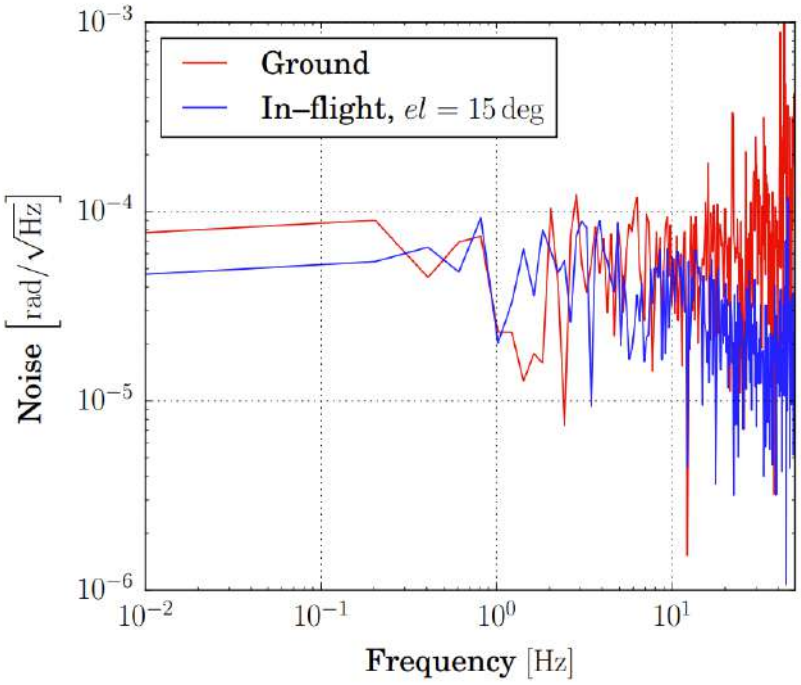

Figure 7.2: OLIMPO Phase noise in rad/$\sqrt{\text{Hz}}$. Figure taken from [66]

OLIMPO in brief is schematized in table 7.1.

OLIMPO	
	Balloon experiment ROACH-2 Virtex-6 FPGA board coupled to MUSIC DAC/ADC board Number of detectors: 130 Multiplexing factor: 64 or 66 Rate: up to 1 kHz 512 MHz RF bandwidth

Table 7.1: OLIMPO summarized in brief.

7.2 BLAST-TNG

All the information related to the BLAST-TNG experiment was taken from [67, 68, 69].
The Next Generation Balloon-Borne Large Aperture Submillimeter Telescope (BLAST-TNG) was a high-angular-resolution instrument developed to characterize the polarized submillimeter sky. Specifically, the purpose of BLAST-TNG was to study the role of magnetic fields in shaping the structure and evolution of the interstellar medium and in regulating star formation by mapping polarized dust emission.
BLAST-TNG was launched from McMurdo Station in Antarctica on January 6th, 2020, and flew for 18 hours.
The BLAST-TNG was a 2.5 m aperture on-axis Cassegrain telescope. The gondola could scan in azimuth at typical rates of 0.05 to 0.2°/s while observing, and slew at speeds of several degrees per second while moving between targets.
BLAST-TNG focal plain was equipped by three microwave KIDs (MKID) arrays, centered at 250, 350, and 500 μm, respectively with 918, 469, and 272 dual-polarization pixels, for a total of about 3.300 detectors, divided between five independent readout modules.
The BLAST-TNG detector arrays were read out using a highly multiplexed, FPGA-based digital spectrometer. This readout is developed for the ROACH-2 board.

The readout electronics, schematically represented in figure 7.3 for a single readout module, consists of a ROACH-2 Virtex-6 FPGA board coupled to a MUSIC DAC/ADC board. An embedded processor (AMCC PowerPC 440EPx) serves as the interface between the FPGA and the data acquisition or flight computer. The analog front-end handles up- and down-conversion of a baseband frequency comb spanning from -256 to 256 MHz, generated by the ROACH-2 and MUSIC board. The RF range containing the resonant frequencies of the KID detectors spans from 500 to 1012 MHz. Digitally programmable attenuators are used at both the modulator output and the demodulator input to match the total frequency comb power to the optimal detector tone power and the full-scale dynamic range of the ADCs. A room temperature amplifier, providing +40 dB of gain, precedes the RF input attenuator.

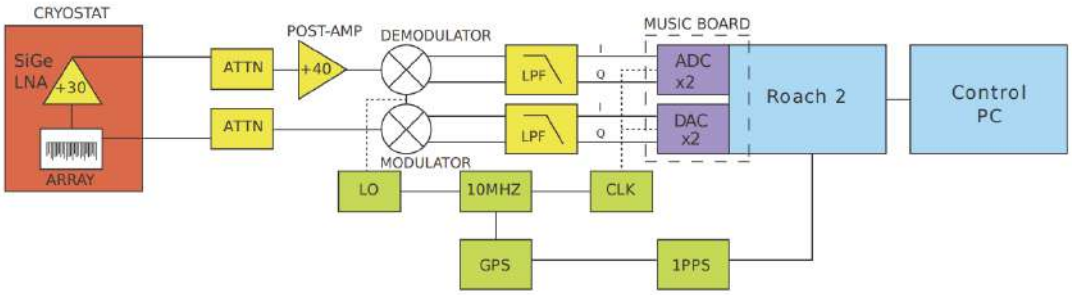

Figure 7.3: BLAST readout electronics block diagram. Figure taken from [68]

Each board is capable of simultaneously reading out over 1000 detectors at a rate of 488 Hz, covering 512 MHz of RF bandwidth.

BLAST-TNG in brief is schematized in table 7.2.

BLAST-TNG	
	Balloon experiment
	ROACH-2 Virtex-6 FPGA board coupled to MUSIC DAC/ADC board
	Number of detectors: ~3.300
	Multiplexing factor: about 660
	Rate: 488 Hz
	512 MHz RF bandwidth

Table 7.2: BLAST-TNG summarized in brief.

7.3 NIKA2

All the information related to the NIKA2 experiment was taken from [70, 71, 72].
NIKA2 (New IRAM KID Arrays) is a next-generation KID camera installed on the 30-meter telescope of the Institut de Radioastronomie Millimétrique (IRAM)at Pico Veleta (Spain).
NIKA2 is an important tool for addressing both astrophysical and cosmological questions, ranging from the study of the SZ effect in galaxy clusters to investigation of star formation in our galaxy.
Its key features include dual-color and polarization capabilities, high sensitivity, high angular resolution, and an instantaneous field of view of 6.5 arcminutes.
NIKA2 polarization system consists of a warm rotating multi-layer Half Wave Plate (HWP) mounted on the pupil of the cryostat, plus a polarizer mounted at the 100 mK stage to split the two components of the linear polarization, and the NIKA2 instrument (cryostat and KIDs matrices).

NIKA2 is equipped with three KID arrays: one array with 1020 pixels for imaging the sky at 150 GHz and two arrays, each with 1140 pixels, for imaging the sky at 260 GHz with polarimetry capabilities. Polarization is only available in one channel, the 260 GHz.
As shown schematically in figure 7.4, the frequency comb is generated at base-

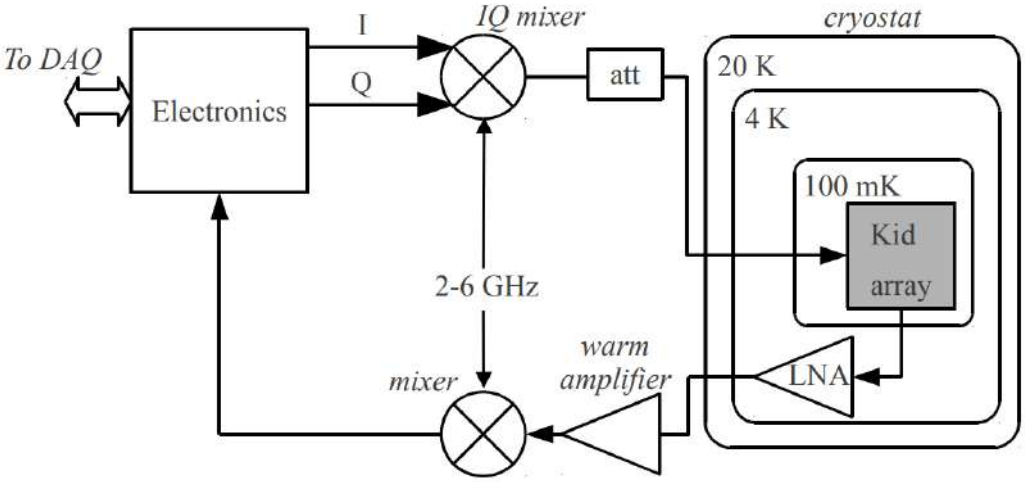

Figure 7.4: NIKA2 readout electronics block diagram. Figure taken from [70]

band in the electronics using a CORDIC algorithm with a precision of ~953 Hz, and up-converted with an IQ RF mixer modulator (ADL5375) to the frequency band of interest, between 1.3 and 2.4 GHz. The comb is then injected in the cold resonator line with the appropriate power level and amplified (ADL5610) before exiting the cryostat. The returning and modified frequency comb is down-converted by an AD8342 demodulator mixer, and it is acquired and analyzed by channelized DDC, which provides the I and Q components of each tone. The LO used for both up and down-conversion is generated by Aeroflex/IFR/Marconi 2024 signal generator.
The system's bandwidth is 500 MHz, and to limit the cross-talk, an average frequency separation of 4 MHz is chosen for the 260 GHz array (resonances from 1.9 GHz to 2.4 GHz) and of 2 MHz for the 150 GHz array (resonances from 1.3 GHz to 1.8 GHz). As a result, the three NIKA2 KID arrays, with a total of 3300 resonators, require 20 readout electronics.
The KID arrays are controlled by the New Iram Kid ELectronics (NIKEL). The digital board consists of a central FPGA ('split') and five processing FPGAs ('proc'). Each processing FPGA drives its associated 16-bit DAC (AD9125 from Analog Devices), generating the adequate frequency comb, supporting up to 80 tones. The 'split' FPGA receives data from a 12-bit ADC (ADS5400 from Texas Instruments), operating at 1 Giga Samples Per Second.
The 'split' FPGA is a Xilinx XC7K70T-2FBG676C and the 'proc' are Xilinx XC7K70T-2FBG484C.
NIKA2 data are sampled at 23.8418 Hz in intensity mode, while in polarimetric

mode, the sampling rate doubles to 47.6836 Hz.

NIKA2 in brief is schematized in table 7.3.

NIKA2	
	Ground-based experiment Xilinx FPGA (XC7K70T-2FBG676C and XC7K70T-2FBG484C) coupled to NIKEL electronics Number of detectors: ∼3.300 Multiplexing factor: about 165 Rate: 23.8418 Hz or 47.6836 Hz 500 MHz RF bandwidth

Table 7.3: NIKA2 summarized in brief.

7.4 GroundBIRD

All the information related to the GroundBIRD experiment was taken from [73, 74, 75].
GroundBIRD is a ground-based (Teide Observatory in Tenerife, Spain, at an elevation of 2400 m above mean sea level) CMB experiment designed to observe the polarization pattern imprinted on large angular scales. Its primary scientific goal is to measure the optical depth τ with a precision $\sigma(\tau) \simeq 0.01$, aiming to cross-check systematic effects found in previous measurements, such as those from the Planck satellite [33].
Due to the fluctuations in atmospheric emissions, the optical loading on the detectors—primarily from atmospheric sources—varies significantly during large angular scale measurements, complicating the precise observation of the power spectrum from the ground.
To capture the large-scale polarized CMB signal while minimizing the impact of atmospheric $1/f$ noise, GroundBIRD observes a wide sky area in the Northern Hemisphere (∼40% of the full sky) using a high-speed rotation of the telescope around the vertical axis. The telescope is tilted 20 degrees from the zenith, achieving rotation speeds of up to 20 rpm to mitigate atmospheric radiation fluctuations.
To achieve diffraction-limited spatial resolution while rotating the telescope at high speeds, GroundBIRD utilizes NbTiN/Al hybrid MKIDs as the focal plane detectors. The focal plane consists of seven MKID arrays, with 138 MKIDs optimized for the 145 GHz band and 23 MKIDs for the 220 GHz band. The 145 GHz band captures the peak frequency of the CMB spectrum, while the 220 GHz band helps in accurately removing contamination from thermal emission caused by Galactic interstellar dust.
An overview of the GroundBIRD readout system is presented in figure 7.4. The system's digital electronics generate a digital RF comb, which is then processed

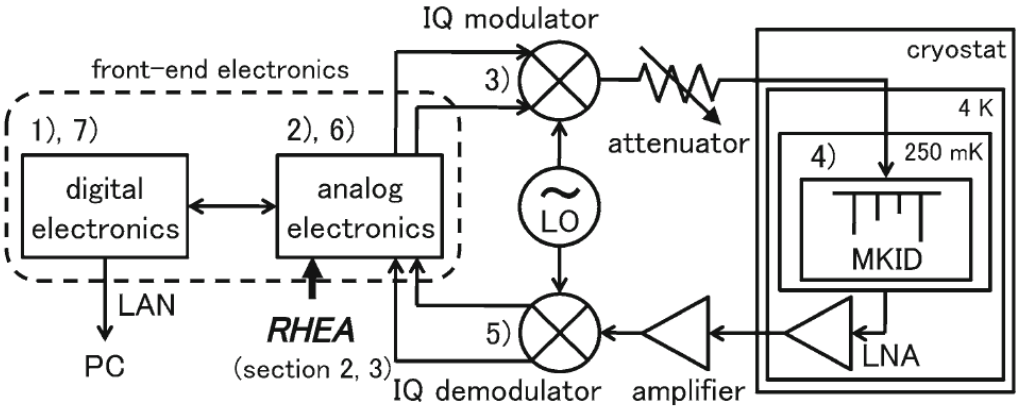

Figure 7.5: GroundBIRD readout electronics block diagram. Figure taken from [73]

through two DACs (DAC3283 by Texas Instruments, Dual-channel, 16-bits, 800 MSPS) in the analog electronics to create RF signals based on the digital RF input. The feed signal is constructed by coupling the cosine and sine waves, and the frequency is up-converted using a Local Oscillator (LO, Epson, EG-2102CA). Within the MKID system, the amplitude and phase of each tone in the comb are modulated. Afterward, the cosine and sine waves are decoupled, and the frequency is down-converted using the same LO. Two ADCs (ADC4249 by Texas Instruments, Dual-channel, 14-bits, 250 MSPS) convert the return RF signals into digital RF signals. These signals are further processed to extract the I and Q components for each MKID comb, and are down-sampled. The adopted strategy is to perform a DDC to extract I and Q variations.
For GroundBIRD, a High spEed Analog board (RHEA) was specifically designed, with a Kintex-7 FPGA, allowing the MKIDs to be sampled continuously at a high rate of 1 kHz, with a deadtime-less readout, a multiplexing factor of 100, and 200 MHz bandwidth. The achieved level of noise is 10^{-8} rad$/\sqrt{\text{Hz}}$, while the expected noise in observing condition is 10^{-5} rad$/\sqrt{\text{Hz}}$, corresponding to noise equivalent temperature of 10^{-17} W$/\sqrt{\text{Hz}}$.

GroundBIRD in brief is schematized in table 7.4.

GroundBIRD	
	Ground-based experiment
	Kintex-7 FPGA
	RHEA board
	Number of detectors: 161
	Multiplexing factor: 100
	Rate: 1 kHz
	200 MHz RF bandwidth

Table 7.4: GroundBIRD summarized in brief.

7.5 Considerations

As discussed in section 2.3.2, the COSMO focal plane will be equipped with two arrays of multimode LEKIDs, each consisting of 9 pixels. These arrays feature waveguides that allow the propagation of 10 to 19 modes in the 130-170 GHz range and of 23 to 42 modes in the 200-300 GHz range.
Thus, COSMO has a lower number of detectors compared to other experiments, but its uniqueness lies in the fact that they are multimode. Consequently, they also exhibit a very low baseband frequency.
The expected time constant is approximately $\tau \sim 60$ μs, which, combined with the scanning strategy (section 2.2), necessitates fast readout electronics, on the order of 60 kHz. This requirement is unique to COSMO, as the previously described experiments do not have such stringent requirements for their readout systems.
Indeed, only the GroundBIRD experiment in section 7.4 reaches a sampling rate of 1 kHz, while all the other experiments have a lower one.
In addition to the high sampling rate, COSMO's firmware is highly flexible and accessible, allowing for easier adjustments to the system. Moreover, the firmware design is accessible for potential future upgrades and modifications, which sets it apart from more rigid systems used in other CMB experiments.
As described in section 6.3, the COSMO readout electronics can reach a phase noise very comparable with the other electronics.
The high sampling rate is particularly useful for cosmic deglitching, which is essential in space but also important at polar observation sites like the one COSMO will use.
Regarding the RF bandwidth, the COSMO readout electronics, as described in section 2.4 is currently limited by the presence of the SLP-44+ filters, however broader filters could be used, up to a bandwidth of approximately 200 MHz.

Chapter 8

Conclusions

COSMO is an ambitious path-finder experiment aimed at studying CMB spectral distortions, providing an alternative approach with respect to B-modes to understand the thermal history of the Universe.
COSMO will perform rapid sky scans, enabling the separation of atmospheric emissions and their fluctuations from the CMB monopole. The fast-spinning wedge flat mirror of COSMO, expected to exceed 600 rpm, will trace a 20° diameter circle in the sky, covering a range of elevations, while the cryogenic interferometer will scan the optical path difference.
In addition to the ambitious fast wedge flat mirror, COSMO's focal plane will feature two arrays, each containing 9 multimode KIDs. This PhD thesis demonstrates the feasibility of developing a working readout electronics for COSMO's KIDs, based on a modular architecture utilizing commercial devices.
Comprehensive functional tests were conducted to characterize all components. The goal of achieving a sampling rate of 60 kHz for all 18 tones was met successfully.
The electronics can operate in two modes: a VNA-like mode used to identify the resonance frequencies of the KID arrays, after performing a calibration, and a second mode where a frequency comb is sent. Indeed, once the resonances are determined, the system can switch to the second mode, where the comb of the found frequencies is sent. Alternatively, a preselected frequency comb can also be sent. The amplitude and phase variations of the KIDs is acquired, and the selected strategy is to perform a DDC.
A user-friendly GUI was developed, enabling users to adjust comb frequencies, select different attenuation levels, monitor the transmitted and received signals, change the LO position, and more.
Furthermore, the software's accessibility also allows for easy modifications.
The level of phase noise, with a warm white noise (warm loopback) of a few $\sim 10^{-6}$ rad$/\sqrt{\text{Hz}}$, is very promising and highly competitive compared to more sophisticated and widely used systems.
Finally, the readout electronics were tested in an environment closer to COSMO's operational conditions. The PSD results, when compared with those obtained using a ROACH2 based-architecture, showed very similar outcomes, further

validating the system's performance.
In the near future, the COSMO collaboration will need to decide whether to confirm the goal (achieved in this thesis) of a 60 kHz sampling rate or reduce this value. This decision arises both from the challenge of storing large amounts of data and the change in the spinning mirror specifications, which have shifted from 2400 rpm to approximately 600 rpm. Additionally, the KIDs to be fabricated will play a crucial role in this process, as their performance, particularly their time constant, will be thoroughly analyzed. However, if the 60 kHz sampling rate is confirmed, a strategy will be needed to address the issue that the electronics described here generates frequency combs that are multiples of the sampling rate itself, 60 kHz. Regardless of the sampling rate, it will also be crucial to handle data packetization, and the removal of spikes caused by cosmic rays.

Ringraziamenti

Alla fine di questo percorso, sento il bisogno di fare dei ringraziamenti.
Le persone che mi sono vicine sanno quanto questi tre anni siano stati complessi, pieni di momenti in cui ho pensato di non farcela e in cui avrei preferito mollare tutto. Se questo non è accaduto, non è solo merito mio, ma anche vostro, delle persone a me care.
Questa lista non è in ordine di importanza, perché ognuno di voi è stato fondamentale.

Inizio ringraziando i miei genitori e la mia famiglia, che, anche quando non comprendevano appieno le mie scelte, sono sempre stati al mio fianco, anche nei momenti più difficili e nelle decisioni più drastiche. Grazie, mamma, per esserci sempre stata e per essere ancora qui, accanto a me.

Un ringraziamento speciale va anche alle persone che ho incontrato lungo questo percorso. È vero, questi tre anni sono stati difficilissimi, ma mi hanno regalato anche tanti ricordi felici, momenti di condivisione e vita, dentro e fuori dall'università. Flavia, la mia amica del cuore, Matteo, Elena: grazie.

Gabriele, grazie che mi sei stato vicino fin dall'inizio, da correlatore di tesi a compagno di ufficio, fino a diventare un vero amico. Sei sempre stato una persona su cui poter contare, per un consiglio, un aiuto, o semplicemente per un confronto sincero, anche quando la verità era scomoda.

Camilla, grazie per il tempo che abbiamo condiviso, per le lunghe telefonate e le risate che hanno reso tutto più leggero.

Ringrazio anche tutte le persone con cui ho condiviso piccoli ma significativi momenti della mia vita da dottoranda: Eugenia, Davide, Andrea T., tutti i colleghi di Milano-Bicocca e di Pisa. Grazie, ragazzi, per le risate insieme, lo scambio di idee e per le serate trascorse insieme.

Un ringraziamento doveroso ad Andrea Passerini, prezioso nella realizzazione di questa tesi, grazie per la tua pazienza e la tua capacità di sdrammatizzare.

Infine, vorrei ringraziare due persone che mi hanno spinto a scrivere queste righe colme di gratitudine: Giovanni e Jochem.

Giovanni, grazie. Da quando ti ho conosciuto, mi hai aiutata a capire cosa voglio fare nella vita e chi voglio diventare. Sei un modello per me, una fonte di ispirazione. Grazie per tutte le volte che, disperata, ti ho chiamato (e continuo a farlo!) e tu mi hai ascoltata, calmata e aiutata a trovare soluzioni. Hai contribuito in modo significativo alla scienziata che sono e che sarò, ma anche alla donna che sono diventata. Grazie per ogni insegnamento e per l'entusiasmo

con cui ascolti i miei racconti della mia nuova vita.

Jochem, grazie a te, perché da quando ho iniziato questo lavoro mi hai insegnato tanto e mi hai dato una fiducia che non pensavo possibile. Sei stato capace di dare un senso a questi tre anni difficili, facendomi capire che tutto ciò è servito a qualcosa. Grazie per la tua attenzione, presenza e disponibilità, e per l'entusiasmo contagioso che metti in ogni cosa che fai.

Jochem, thank you. Since I started this job, you have taught me so much and given me a level of trust I never thought possible. You have been able to give meaning to these three challenging years, helping me realize that it was all worth it. Thank you for your care, constant support, and availability, as well as for the contagious enthusiasm you bring to everything you do.

Bibliography

[1] Arno A. Penzias and Robert Woodrow Wilson. A Measurement of excess antenna temperature at 4080-Mc/s. *Astrophys. J.*, 142:419–421, 1965.

[2] A. Friedmann. Über die Möglichkeit einer Welt mit konstanter negativer Krümmung des Raumes, 1924.

[3] Abbé G. Lemaître. A Homogeneous Universe of Constant Mass and Increasing Radius accounting for the Radial Velocity of Extra-galactic Nebulæ. *Monthly Notices of the Royal Astronomical Society*, 91(5):483–490, 03 1931.

[4] H. P. Robertson. Kinematics and World-Structure. *apj*, 82:284, November 1935.

[5] A. G. Walker. On Milne's Theory of World-Structure. *Proceedings of the London Mathematical Society*, 42:90–127, January 1937.

[6] H. Bondi and T. Gold. The Steady-State Theory of the Expanding Universe. *mnras*, 108:252, January 1948.

[7] F. Hoyle. A New Model for the Expanding Universe. *mnras*, 108:372, January 1948.

[8] Planck Collaboration. Planck 2018 results. vi. cosmological parameters. *Astronomy and Astrophysics*, 641:A6, Sep 2020.

[9] G. Gamow. Expanding universe and the origin of elements. *Phys. Rev.*, 70:572–573, Oct 1946.

[10] R. A. Alpher. A Neutron-Capture Theory of the Formation and Relative Abundance of the Elements. *Physical Review*, 74(11):1577–1589, December 1948.

[11] R. H. Dicke. The Measurement of Thermal Radiation at Microwave Frequencies. *Review of Scientific Instruments*, 17(7):268–275, July 1946.

[12] R. H. Dicke, P. J. E. Peebles, P. G. Roll, and D. T. Wilkinson. Cosmic Black-Body Radiation. *apj*, 142:414–419, July 1965.

[13] G. Smoot, G. De Amici, S.D. Friedman, C. Witebski, N. Mandolesi, R.B. Partridge, G. Sironi, L. Danese, and G. De Zotti. New multifrequency measurements of the spectrum of the cosmic background radiation. *Advances in Space Research*, 3(10):465–467, 1984.

[14] G. F. Smoot, M. V. Gorenstein, and R. A. Muller. Detection of Anisotropy in the Cosmic Blackbody Radiation. *prl*, 39(14):898–901, October 1977.

[15] R. Fabbri, I. Guidi, F. Melchiorri, and V. Natale. Measurement of the cosmic-background large-scale anisotropy in the millimetric region. *Phys. Rev. Lett.*, 44:1563–1566, Jun 1980.

[16] D. J. Fixsen, E. S. Cheng, D. A. Cottingham, Jr. Eplee, R. E., R. B. Isaacman, J. C. Mather, S. S. Meyer, P. D. Noerdlinger, R. A. Shafer, R. Weiss, E. L. Wright, C. L. Bennett, N. W. Boggess, T. Kelsall, S. H. Moseley, R. F. Silverberg, G. F. Smoot, and D. T. Wilkinson. Cosmic Microwave Background Dipole Spectrum Measured by the COBE FIRAS Instrument. *apj*, 420:445, January 1994.

[17] J. C. Mather, M. G. Hauser, C. L. Bennett, N. W. Boggess, E. S. Cheng, Eplee R. E., H. T. Freudenreich, R. B. Isaacman, T. Kelsall, C. M. Lisse, Moseley S. H., R. A. Shafer, R. F. Silverberg, W. J. Spiesman, G. N. Toller, J. L. Weiland, S. Gulkis, M. Jansssen, P. M. Lubin, S. S. Meyer, R. Weiss, T. L. Murdock, G. F. Smoot, D. T. Wilkinson, and E. L. Wright. Early results from the Cosmic Background Explorer (COBE). *Advances in Space Research*, 11(2):181–191, January 1991.

[18] G. F. Smoot, C. L. Bennett, A. Kogut, J. Aymon, C. Backus, G. de Amici, K. Galuk, P. D. Jackson, P. Keegstra, L. Rokke, L. Tenorio, S. Torres, S. Gulkis, M. G. Hauser, M. Janssen, J. C. Mather, R. Weiss, D. T. Wilkinson, E. L. Wright, N. W. Boggess, E. S. Cheng, T. Kelsall, P. Lubin, S. Meyer, S. H. Moseley, T. L. Murdock, R. A. Shafer, and R. F. Silverberg. First results of the COBE satellite measurement of the anisotropy of the cosmic microwave background radiation. *Advances in Space Research*, 11(2):193–205, January 1991.

[19] G. F. Smoot, C. L. Bennett, A. Kogut, J. Aymon, C. Backus, G. de Amici, K. Galuk, P. D. Jackson, P. Keegstra, L. Rokke, L. Tenorio, S. Torres, S. Gulkis, M. G. Hauser, M. A. Janssen, J. C. Mather, R. Weiss, D. T. Wilkinson, E. L. Wright, N. W. Boggess, E. S. Cheng, T. Kelsall, P. Lubin, S. Meyer, S. H. Moseley, T. L. Murdock, R. A. Shafer, and R. F. Silverberg. Preliminary Results from the COBE Differential Microwave Radiometers: Large Angular Scale Isotropy of the Cosmic Microwave Background. *apjl*, 371:L1, April 1991.

[20] J. C. Mather, E. S. Cheng, D. A. Cottingham, Jr. Eplee, R. E., D. J. Fixsen, T. Hewagama, R. B. Isaacman, K. A. Jensen, S. S. Meyer, P. D. Noerdlinger,

S. M. Read, L. P. Rosen, R. A. Shafer, E. L. Wright, C. L. Bennett, N. W. Boggess, M. G. Hauser, T. Kelsall, Jr. Moseley, S. H., R. F. Silverberg, G. F. Smoot, R. Weiss, and D. T. Wilkinson. Measurement of the Cosmic Microwave Background Spectrum by the COBE FIRAS Instrument. *apj*, 420:439, January 1994.

[21] A. J. Banday, K. M. Gorski, L. Tenorio, E. L. Wright, G. F. Smoot, C. H. Lineweaver, A. Kogut, G. Hinshaw, and C. L. Bennett. On the RMS Anisotropy at 7 degrees and 10 degrees in the COBE-DMR Two-Year Sky Maps. *apjl*, 436:L99, December 1994.

[22] D. J. Fixsen, E. S. Cheng, J. M. Gales, J. C. Mather, R. A. Shafer, and E. L. Wright. The Cosmic Microwave Background Spectrum from the Full COBE FIRAS Data Set. *apj*, 473:576, December 1996.

[23] B. P. Crill, P. A. R. Ade, D. R. Artusa, R. S. Bhatia, J. J. Bock, A. Boscaleri, P. Cardoni, S. E. Church, K. Coble, P. de Bernardis, and et al. Boomerang: A balloon-borne millimeter-wave telescope and total power receiver for mapping anisotropy in the cosmic microwave background. *The Astrophysical Journal Supplement Series*, 148(2):527–541, Oct 2003.

[24] B. Rabii, C. D. Winant, J. S. Collins, A. T. Lee, P. L. Richards, M. E. Abroe, S. Hanany, B. R. Johnson, P. Ade, A. Balbi, and et al. Maxima: A balloon-borne cosmic microwave background anisotropy experiment. *Review of Scientific Instruments*, 77(7):071101, Jul 2006.

[25] E. M. Leitch, C. Pryke, N. W. Halverson, J. Kovac, G. Davidson, S. LaRoque, E. Schartman, J. Yamasaki, J. E. Carlstrom, W. L. Holzapfel, and et al. Experiment design and first season observations with the degree angular scale interferometer. *The Astrophysical Journal*, 568(1):28–37, Mar 2002.

[26] Nine-year wilkinson microwave anisotropy probe (wmap) observations: Final maps and results. 208.

[27] Planck2013 results. i. overview of products and scientific results. 571.

[28] Brian G. Keating, Peter A. R. Ade, James J. Bock, Eric Hivon, William L. Holzapfel, Andrew E. Lange, Hien Nguyen, and Ki Won Yoon. BICEP: a large angular scale CMB polarimeter. 4843:284–295, February 2003.

[29] Daniela Paoletti, Fabio Finelli, Jussi Valiviita, and Masashi Hazumi. Planck and bicep/keck array 2018 constraints on primordial gravitational waves and perspectives for future <mml:math xmlns:mml="http://www.w3.org/1998/math/mathml" display="inline"><mml:mi>b</mml:mi></mml:math> -mode polarization measurements. *Physical Review D*, 106(8), October 2022.

[30] Sptpol: an instrument for cmb polarization measurements with the south pole telescope.

[31] B. Keating, S. Moyerman, D. Boettger, J. Edwards, G. Fuller, F. Matsuda, N. Miller, H. Paar, G. Rebeiz, I. Schanning, M. Shimon, N. Stebor, K. Arnold, D. Flanigan, W. Holzapfel, J. Howard, Z. Kermish, A. Lee, M. Lungu, M. Myers, H. Nishino, R. O'Brient, E. Quealy, C. Reichardt, P. Richards, C. Shimmin, B. Steinbach, A. Suzuki, O. Zahn, J. Borrill, C. Cantalupo, E. Kisner, E. Linder, M. Sholl, H. Spieler, A. Anthony, N. Halverson, J. Errard, G. Fabbian, M. Le Jeune, R. Stompor, A. Jaffe, D. O'Dea, Y. Chinone, M. Hasegawa, M. Hazumi, T. Matsumura, H. Morii, A. Shimizu, T. Tomaru, P. Hyland, M. Dobbs, P. Ade, W. Grainger, and C. Tucker. Ultra high energy cosmology with polarbear, 2011.

[32] J. M. Nagy, P. A. R. Ade, M. Amiri, S. J. Benton, A. S. Bergman, R. Bihary, J. J. Bock, J. R. Bond, S. A. Bryan, H. C. Chiang, and et al. A new limit on cmb circular polarization from spider. *The Astrophysical Journal*, 844(2):151, Aug 2017.

[33] N. Aghanim, Y. Akrami, M. Ashdown, J. Aumont, C. Baccigalupi, M. Ballardini, A. J. Banday, R. B. Barreiro, N. Bartolo, S. Basak, R. Battye, K. Benabed, J.-P. Bernard, M. Bersanelli, P. Bielewicz, J. J. Bock, J. R. Bond, J. Borrill, F. R. Bouchet, F. Boulanger, M. Bucher, C. Burigana, R. C. Butler, E. Calabrese, J.-F. Cardoso, J. Carron, A. Challinor, H. C. Chiang, J. Chluba, L. P. L. Colombo, C. Combet, D. Contreras, B. P. Crill, F. Cuttaia, P. de Bernardis, G. de Zotti, J. Delabrouille, J.-M. Delouis, E. Di Valentino, J. M. Diego, O. Doré, M. Douspis, A. Ducout, X. Dupac, S. Dusini, G. Efstathiou, F. Elsner, T. A. Enßlin, H. K. Eriksen, Y. Fantaye, M. Farhang, J. Fergusson, R. Fernandez-Cobos, F. Finelli, F. Forastieri, M. Frailis, A. A. Fraisse, E. Franceschi, A. Frolov, S. Galeotta, S. Galli, K. Ganga, R. T. Génova-Santos, M. Gerbino, T. Ghosh, J. González-Nuevo, K. M. Górski, S. Gratton, A. Gruppuso, J. E. Gudmundsson, J. Hamann, W. Handley, F. K. Hansen, D. Herranz, S. R. Hildebrandt, E. Hivon, Z. Huang, A. H. Jaffe, W. C. Jones, A. Karakci, E. Keihänen, R. Keskitalo, K. Kiiveri, J. Kim, T. S. Kisner, L. Knox, N. Krachmalnicoff, M. Kunz, H. Kurki-Suonio, G. Lagache, J.-M. Lamarre, A. Lasenby, M. Lattanzi, C. R. Lawrence, M. Le Jeune, P. Lemos, J. Lesgourgues, F. Levrier, A. Lewis, M. Liguori, P. B. Lilje, M. Lilley, V. Lindholm, M. López-Caniego, P. M. Lubin, Y.-Z. Ma, J. F. Macías-Pérez, G. Maggio, D. Maino, N. Mandolesi, A. Mangilli, A. Marcos-Caballero, M. Maris, P. G. Martin, M. Martinelli, E. Martínez-González, S. Matarrese, N. Mauri, J. D. McEwen, P. R. Meinhold, A. Melchiorri, A. Mennella, M. Migliaccio, M. Millea, S. Mitra, M.-A. Miville-Deschênes, D. Molinari, L. Montier, G. Morgante, A. Moss, P. Natoli, H. U. Nørgaard-Nielsen, L. Pagano, D. Paoletti, B. Partridge, G. Patanchon, H. V. Peiris, F. Perrotta, V. Pettorino, F. Piacentini, L. Polastri, G. Polenta, J.-L. Puget, J. P. Rachen, M. Reinecke, M. Remazeilles, A. Renzi, G. Rocha, C. Rosset, G. Roudier, J. A. Rubiño-Martín, B. Ruiz-Granados, L. Salvati, M. Sandri, M. Savelainen, D. Scott, E. P. S. Shellard, C. Sirignano, G. Sirri, L. D. Spencer, R. Sunyaev, A.-S. Suur-Uski, J. A. Tauber, D. Tavagnacco, M. Tenti,

L. Toffolatti, M. Tomasi, T. Trombetti, L. Valenziano, J. Valiviita, B. Van Tent, L. Vibert, P. Vielva, F. Villa, N. Vittorio, B. D. Wandelt, I. K. Wehus, M. White, S. D. M. White, A. Zacchei, and A. Zonca. Planck2018 results: Vi. cosmological parameters. *Astronomy & Astrophysics*, 641:A6, September 2020.

[34] Barbara Ryden. *Introduction to Cosmology*. Cambridge University Press, 2 edition, 2016.

[35] Marc Kamionkowski and Ely D. Kovetz. The quest for b modes from inflationary gravitational waves. *Annual Review of Astronomy and Astrophysics*, 54(1):227–269, September 2016.

[36] Planck Collaboration. Planck2015 results. i. overview of products and scientific results. *Astronomy and Astrophysics*, 594:A1, Sep 2016.

[37] J. C. Mather, E. S. Cheng, D. A. Cottingham, Jr. Eplee, R. E., D. J. Fixsen, T. Hewagama, R. B. Isaacman, K. A. Jensen, S. S. Meyer, P. D. Noerdlinger, S. M. Read, L. P. Rosen, R. A. Shafer, E. L. Wright, C. L. Bennett, N. W. Boggess, M. G. Hauser, T. Kelsall, Jr. Moseley, S. H., R. F. Silverberg, G. F. Smoot, R. Weiss, and D. T. Wilkinson. Measurement of the Cosmic Microwave Background Spectrum by the COBE FIRAS Instrument. *apj*, 420:439, January 1994.

[38] M. Gervasi, M. Zannoni, A. Tartari, G. Boella, and G. Sironi. Tris. ii. search for cmb spectral distortions at 0.60, 0.82, and 2.5 ghz. *The Astrophysical Journal*, 688(1):24–31, November 2008.

[39] Jens Chluba. Which spectral distortions does ΛCDM actually predict? *Monthly Notices of the Royal Astronomical Society*, 460(1):227–239, April 2016.

[40] Jens Chluba. Future steps in cosmology using spectral distortions of the cosmic microwave background, 2018.

[41] S. Masi, E. Battistelli, P. de Bernardis, A. Coppolecchia, F. Columbro, G. D'Alessandro, M. De Petris, L. Lamagna, E. Marchitelli, L. Mele, A. Paiella, F. Piacentini, G. Pisano, M. Bersanelli, C. Franceschet, E. Manzan, D. Mennella, S. Realini, S. Cibella, F. Martini, G. Pettinari, G. Coppi, M. Gervasi, A. Limonta, M. Zannoni, L. Piccirillo, and C. Tucker. The cosmic monopole observer (cosmo), 2021.

[42] Giuseppe D'Alessandro, Paolo de Bernardis, Silvio di Tano, Silvia Masi, and Lorenzo Mele. Polarizing beam-splitter rotation in martin-puplett interferometers for spectroscopic measurements at millimeter wavelengths. *Infrared Physics & Technology*, 85:92–98, 2017.

[43] D.H. Martin and E. Puplett. Polarised interferometric spectrometry for the millimetre and submillimetre spectrum. *Infrared Physics*, 10(2):105–109, 1970.

[44] S. Masi, E.S. Battistelli, P. de Bernardis, C. Chapron, F. Columbro, A. Coppolecchia, G. D'Alessandro, M. De Petris, L. Grandsire, J.-Ch. Hamilton, L. Lamagna, S. Marnieros, A. May, L. Mele, A. Mennella, C. O'Sullivan, A. Paiella, F. Piacentini, M. Piat, L. Piccirillo, G. Presta, A. Schillaci, A. Tartari, J.-P. Thermeau, S.A. Torchinsky, F. Voisin, M. Zannoni, P. Ade, J.G. Alberro, A. Almela, G. Amico, L.H. Arnaldi, D. Auguste, J. Aumont, S. Azzoni, S. Banfi, A. Baù, B. Bélier, D. Bennett, L. Bergé, J.-Ph. Bernard, M. Bersanelli, M.-A. Bigot-Sazy, J. Bonaparte, J. Bonis, E. Bunn, D. Burke, D. Buzi, F. Cavaliere, P. Chanial, R. Charlassier, A.C. Cobos Cerutti, G. De Gasperis, M. De Leo, S. Dheilly, C. Duca, L. Dumoulin, A. Etchegoyen, A. Fasciszewski, L.P. Ferreyro, D. Fracchia, C. Franceschet, M.M. Gamboa Lerena, K.M. Ganga, B. García, M.E. García Redondo, M. Gaspard, D. Gayer, M. Gervasi, M. Giard, V. Gilles, Y. Giraud-Heraud, M. Gómez Berisso, M. González, M. Gradziel, M.R. Hampel, D. Harari, S. Henrot-Versillé, F. Incardona, E. Jules, J. Kaplan, C. Kristukat, S. Loucatos, T. Louis, B. Maffei, W. Marty, A. Mattei, M. McCulloch, D. Melo, L. Montier, L. Mousset, L.M. Mundo, J.A. Murphy, J.D. Murphy, F. Nati, E. Olivieri, C. Oriol, F. Pajot, A. Passerini, H. Pastoriza, A. Pelosi, C. Perbost, M. Perciballi, F. Pezzotta, G. Pisano, M. Platino, G. Polenta, D. Prêle, R. Puddu, D. Rambaud, E. Rasztocky, P. Ringegni, G.E. Romero, J.M. Salum, C.G. Scóccola, S. Scully, S. Spinelli, G. Stankowiak, M. Stolpovskiy, A.D. Supanitsky, P. Timbie, M. Tomasi, C. Tucker, G. Tucker, D. Viganò, N. Vittorio, F. Wicek, M. Wright, and A. Zullo. Qubic v: Cryogenic system design and performance. *Journal of Cosmology and Astroparticle Physics*, 2022(04):038, April 2022.

[45] Heike Kamerlingh Onnes. On the sudden change in the rate at which liquid helium ii evaporates at very low temperatures. *Communications from the Physical Laboratory at the University of Leiden*, (120b), July 1911.

[46] J. Bardeen, L. N. Cooper, and J. R. Schrieffer. Theory of superconductivity. *Phys. Rev.*, 108:1175–1204, Dec 1957.

[47] Jonas Zmuidzinas. Superconducting microresonators: Physics and applications. *Annual Review of Condensed Matter Physics*, 3(1):169–214, 2012.

[48] D. C. Mattis and J. Bardeen. Theory of the anomalous skin effect in normal and superconducting metals. *Phys. Rev.*, 111:412–417, Jul 1958.

[49] P. D. Mauskopf. Transition edge sensors and kinetic inductance detectors in astronomical instruments. *Publications of the Astronomical Society of the Pacific*, 130(990):082001, jun 2018.

[50] David M. Pozar. *Microwave Engineering*. Wiley, 2011.

[51] S. B. Kaplan, C. C. Chi, D. N. Langenberg, J. J. Chang, S. Jafarey, and D. J. Scalapino. Quasiparticle and phonon lifetimes in superconductors. *Phys. Rev. B*, 14:4854–4873, Dec 1976.

[52] D. Flanigan, H. McCarrick, G. Jones, B. R. Johnson, M. H. Abitbol, P. Ade, D. Araujo, K. Bradford, R. Cantor, G. Che, P. Day, S. Doyle, C. B. Kjellstrand, H. Leduc, M. Limon, V. Luu, P. Mauskopf, A. Miller, T. Mroczkowski, C. Tucker, and J. Zmuidzinas. Photon noise from chaotic and coherent millimeter-wave sources measured with horn-coupled, aluminum lumped-element kinetic inductance detectors. *Applied Physics Letters*, 108(8), February 2016.

[53] P. J. de Visser, D. J. Goldie, P. Diener, S. Withington, J. J. A. Baselmans, and T. M. Klapwijk. Evidence of a nonequilibrium distribution of quasiparticles in the microwave response of a superconducting aluminum resonator. *Phys. Rev. Lett.*, 112:047004, Jan 2014.

[54] A. Catalano, M. Calvo, N. Ponthieu, R. Adam, A. Adane, P. Ade, P. André, A. Beelen, B. Belier, A. Benoît, A. Bideaud, N. Billot, N. Boudou, O. Bourrion, G. Coiffard, B. Comis, A. D'Addabbo, F.-X. Désert, S. Doyle, J. Goupy, C. Kramer, S. Leclercq, J. F. Macías-Pérez, J. Martino, P. Mauskopf, F. Mayet, A. Monfardini, F. Pajot, E. Pascale, L. Perotto, V. Revéret, L. Rodriguez, G. Savini, K. Schuster, A. Sievers, C. Tucker, and R. Zylka. Performance and calibration of the nika camera at the iram 30 m telescope. *Astronomy & Astrophysics*, 569:A9, September 2014.

[55] J. Hubmayr, J. Beall, D. Becker, H.-M. Cho, M. Devlin, B. Dober, C. Groppi, G. C. Hilton, K. D. Irwin, D. Li, P. Mauskopf, D. P. Pappas, J. Van Lanen, M. R. Vissers, Y. Wang, L. F. Wei, and J. Gao. Photon-noise limited sensitivity in titanium nitride kinetic inductance detectors. *Applied Physics Letters*, 106(7), February 2015.

[56] J. Gao. *The Physics of Superconducting Microwave Resonators*. PhD thesis, California Institute of Technology, 2008.

[57] Charles Kittel and Herbert Kroemer. *Thermal Physics*. W. H. Freeman, 1998.

[58] S. Rowe. *Passive terahertz imaging with lumped element kinetic inductance detectors*. PhD thesis, School of Physics and Astronomy, Cardiff University, 2015.

[59] P. Barry. *On the development of SuperSpec: a fully integrated on-chip spectrometer for far-infrared astronomy.* PhD thesis, Cardiff University, 2014.

[60] Peter Ade, James Aguirre, Zeeshan Ahmed, Simone Aiola, Aamir Ali, David Alonso, Marcelo A. Alvarez, Kam Arnold, Peter Ashton, Jason Austermann, and et al. The Simons Observatory: science goals and forecasts. *jcap*, 2019(2):056, February 2019.

[61] S. W. Henderson, R. Allison, J. Austermann, T. Baildon, N. Battaglia, J. A. Beall, D. Becker, F. De Bernardis, J. R. Bond, E. Calabrese, S. K. Choi, K. P. Coughlin, K. T. Crowley, R. Datta, M. J. Devlin, S. M. Duff, J. Dunkley,

R. Dünner, A. van Engelen, P. A. Gallardo, E. Grace, M. Hasselfield, F. Hills, G. C. Hilton, A. D. Hincks, R. Hlozek, S. P. Ho, J. Hubmayr, K. Huffenberger, J. P. Hughes, K. D. Irwin, B. J. Koopman, A. B. Kosowsky, D. Li, J. McMahon, C. Munson, F. Nati, L. Newburgh, M. D. Niemack, P. Niraula, L. A. Page, C. G. Pappas, M. Salatino, A. Schillaci, B. L. Schmitt, N. Sehgal, B. D. Sherwin, J. L. Sievers, S. M. Simon, D. N. Spergel, S. T. Staggs, J. R. Stevens, R. Thornton, J. Van Lanen, E. M. Vavagiakis, J. T. Ward, and E. J. Wollack. Advanced actpol cryogenic detector arrays and readout. *Journal of Low Temperature Physics*, 184(3–4):772–779, March 2016.

[62] J. A. B. Mates, D. T. Becker, D. A. Bennett, B. J. Dober, J. D. Gard, J. P. Hays-Wehle, J. W. Fowler, G. C. Hilton, C. D. Reintsema, D. R. Schmidt, D. S. Swetz, L. R. Vale, and J. N. Ullom. Simultaneous readout of 128 x-ray and gamma-ray transition-edge microcalorimeters using microwave squid multiplexing. *Applied Physics Letters*, 111(6):062601, 08 2017.

[63] S. M. Stanchfield, P. A. R. Ade, J. Aguirre, J. A. Brevik, H. M. Cho, R. Datta, M. J. Devlin, S. R. Dicker, B. Dober, D. Egan, P. Ford, G. Hilton, J. Hubmayr, K. D. Irwin, P. Marganian, B. S. Mason, J. A. B. Mates, J. McMahon, M. Mello, T. Mroczkowski, C. Romero, C. Tucker, L. Vale, S. White, M. Whitehead, and A. H. Young. Development of a Microwave SQUID-Multiplexed TES Array for MUSTANG-2. *Journal of Low Temperature Physics*, 184(1-2):460–465, July 2016.

[64] A. Paiella, A. Coppolecchia, L. Lamagna, P.A.R. Ade, E.S. Battistelli, M. G. Castellano, I. Colantoni, F. Columbro, G. D'Alessandro, P. de Bernardis, S. Gordon, S. Masi, P. Mauskopf, G. Pettinari, F. Piacentini, G. Pisano, G. Presta, and C. Tucker. Kinetic inductance detectors for the olimpo experiment: design and pre-flight characterization. *Journal of Cosmology and Astroparticle Physics*, 2019(01):039–039, January 2019.

[65] A Paiella, E S Battistelli, M G Castellano, I Colantoni, F Columbro, A Coppolecchia, G D'Alessandro, P de Bernardis, S Gordon, L Lamagna, H Mani, S Masi, P Mauskopf, G Pettinari, F Piacentini, and G Presta. Kinetic inductance detectors and readout electronics for the olimpo experiment. *Journal of Physics: Conference Series*, 1182(1):012005, February 2019.

[66] S. Masi, P. de Bernardis, A. Paiella, F. Piacentini, L. Lamagna, A. Coppolecchia, P.A.R. Ade, E.S. Battistelli, M.G. Castellano, I. Colantoni, F. Columbro, G. D'Alessandro, M. De Petris, S. Gordon, C. Magneville, P. Mauskopf, G. Pettinari, G. Pisano, G. Polenta, G. Presta, E. Tommasi, C. Tucker, V. Vdovin, A. Volpe, and D. Yvon. Kinetic inductance detectors for the olimpo experiment: in-flight operation and performance. *Journal of Cosmology and Astroparticle Physics*, 2019(07):003, jul 2019.

[67] Nicholas Galitzki, Peter A. R. Ade, Francesco E. Angilè, Peter Ashton, James A. Beall, Dan Becker, Kristi J. Bradford, George Che, Hsiao-Mei

Cho, Mark J. Devlin, Bradley J. Dober, Laura M. Fissel, Yasuo Fukui, Jiansong Gao, Christopher E. Groppi, Seth Hillbrand, Gene C. Hilton, Johannes Hubmayr, Kent D. Irwin, Jeffrey Klein, Jeff Van Lanen, Dale Li, Zhi-Yun Li, Nathan P. Lourie, Hamdi Mani, Peter G. Martin, Philip Mauskopf, Fumitaka Nakamura, Giles Novak, David P. Pappas, Enzo Pascale, Giampaolo Pisano, Fabio P. Santos, Giorgio Savini, Douglas Scott, Sara Stanchfield, Carole Tucker, Joel N. Ullom, Matthew Underhill, Michael R. Vissers, and Derek Ward-Thompson. The next generation blast experiment. *Journal of Astronomical Instrumentation*, 03(02), November 2014.

[68] Samuel Gordon, Brad Dober, Adrian Sinclair, Samuel Rowe, Sean Bryan, Philip Mauskopf, Jason Austermann, Mark Devlin, Simon Dicker, Jiansong Gao, Gene C. Hilton, Johannes Hubmayr, Glenn Jones, Jeffrey Klein, Nathan P. Lourie, Christopher McKenney, Federico Nati, Juan D. Soler, Matthew Strader, and Michael Vissers. An open source, fpga-based lekid readout for blast-tng: Pre-flight results. *Journal of Astronomical Instrumentation*, 05(04), December 2016.

[69] Gabriele Coppi, Peter A. Ade, Peter C. Ashton, Jason E. Austermann, Erin G. Cox, Mark J. Devlin, Bradley J. Dober, Valentina Fanfani, Laura M. Fissel, Nicholas B. Galitzki, Jiansong Gao, Samuel Gordon, Christopher E. Groppi, Gene C. Hilton, Johannes Hubmayr, Jeffrey Klein, Dale Li, Ian Lowe, Nathan P. Lourie, Christopher Mckinney, Hamdi Mani, Philip D. Mauskopf, Federico Nati, Giles Novak, Giampaolo Pisano, Javier L. Romualdez, Adrian K. Sinclair, Juan D. Soler, Carole Tucker, Joel Ullom, Michael Visser, Caleb H. Wheeler, and Paul A. Williams. In-flight performance of the blast-tng telescope platform. In Heather K. Marshall, Jason Spyromilio, and Tomonori Usuda, editors, *Ground-based and Airborne Telescopes VIII*, page 281. SPIE, December 2020.

[70] O Bourrion, A Bideaud, A Benoit, A Cruciani, J F Macias-Perez, A Monfardini, M Roesch, L Swenson, and C Vescovi. Electronics and data acquisition demonstrator for a kinetic inductance camera. *Journal of Instrumentation*, 6(06):P06012–P06012, June 2011.

[71] Adam, R., Adane, A., Ade, P. A. R., André, P., Andrianasolo, A., Aussel, H., Beelen, A., Benoît, A., Bideaud, A., Billot, N., Bourrion, O., Bracco, A., Calvo, M., Catalano, A., Coiffard, G., Comis, B., De Petris, M., Désert, F.-X., Doyle, S., Driessen, E. F. C., Evans, R., Goupy, J., Kramer, C., Lagache, G., Leclercq, S., Leggeri, J.-P., Lestrade, J.-F., Macías-Pérez, J. F., Mauskopf, P., Mayet, F., Maury, A., Monfardini, A., Navarro, S., Pascale, E., Perotto, L., Pisano, G., Ponthieu, N., Revéret, V., Rigby, A., Ritacco, A., Romero, C., Roussel, H., Ruppin, F., Schuster, K., Sievers, A., Triqueneaux, S., Tucker, C., and Zylka, R. The nika2 large-field-of-view millimetre continuum camera for the 30 m iram telescope. *A&A*, 609:A115, 2018.

[72] O. Bourrion, A. Benoit, J.L. Bouly, J. Bouvier, G. Bosson, M. Calvo, A. Catalano, J. Goupy, C. Li, J.F. Macías-Pérez, A. Monfardini, D. Tourres, N. Ponchant, and C. Vescovi. Nikel amc: readout electronics for the nika2 experiment. *Journal of Instrumentation*, 11(11):P11001–P11001, November 2016.

[73] K. Lee, J. Choi, R. T. Génova-Santos, M. Hattori, M. Hazumi, S. Honda, T. Ikemitsu, H. Ishida, H. Ishitsuka, Y. Jo, K. Karatsu, K. Kiuchi, J. Komine, R. Koyano, H. Kutsuma, S. Mima, M. Minowa, J. Moon, M. Nagai, T. Nagasaki, M. Naruse, S. Oguri, C. Otani, M. Peel, R. Rebolo, J. A. Rubiño-Martín, Y. Sekimoto, J. Suzuki, T. Taino, O. Tajima, N. Tomita, T. Uchida, E. Won, and M. Yoshida. Groundbird: A cmb polarization experiment with mkid arrays. *Journal of Low Temperature Physics*, 200(5–6):384–391, August 2020.

[74] Miku Tsujii, Jochem J. A. Baselmans, Jihoon Choi, Antonio H. M. Coppens, Alessandro Fasano, Ricardo Tanausú Génova-Santos, Makoto Hattori, Masashi Hazumi, Shunsuke Honda, Takuji Ikemitsu, Hidesato Ishida, Hikaru Ishitsuka, Hoyong Jeong, Yonggil Jo, Kenichi Karatsu, Keisuke Kataoka, Kenji Kiuchi, Junta Komine, Ryo Koyano, Hiroki Kutsuma, Kyungmin Lee, Satoru Mima, Makoto Nagai, Taketo Nagasaki, Masato Naruse, Shugo Oguri, Chiko Otani, Michael W. Peel, Rafael Rebolo, José Alberto Rubiño-Martín, Yutaro Sekimoto, Yoshinori Sueno, Junya Suzuki, Tohru Taino, Osamu Tajima, Tomonaga Tanaka, David J. Thoen, Nozomu Tomita, Yuta Tsuji, Tomohisa Uchida, Eunil Won, and Mitsuhiro Yoshida. Commissioning the cmb polarization telescope groundbird with the full set of detectors, 2024.

[75] H. Ishitsuka, M. Ikeno, S. Oguri, O. Tajima, N. Tomita, and Tomohisa Uchida. Front–end electronics for the array readout of a microwave kinetic inductance detector towards observation of cosmic microwave background polarization. *Journal of Low Temperature Physics*, 184, 07 2016.

[76] F. Lucchin Peter Coles Prof Peter Coles, Francesco Lucchin. *Cosmology: the origin and evolution of cosmic structure*. Wiley, 2 edition, 2002.

[77] R. B. Partridge. *3K: The Cosmic Microwave Background Radiation (Cambridge Astrophysics)*. 1995.

[78] P. J. E. Peebles. *Principles of physical cosmology*. Princeton series in physics. Princeton University Press, 1993.

[79] J. A. Peacock. *Cosmological physics*. Cambridge Astrophysics. Cambridge University Press, 1 edition, 1998.

[80] Bruce T. Draine and Aurélien A. Fraisse. Polarized far-infrared and submillimeter emission from interstellar dust. *The Astrophysical Journal*, 696(1):1–11, Apr 2009.

[81] Paolo de Bernardis and Silvia Masi. Cosmic microwave background and cosmic polarization rotation: An experimentalist view. *International Journal of Modern Physics D*, 25(11):1640012, 2016.